The E and B EXperiment: Implementation and Analysis of the 2009 Engineering Flight

A DISSERTATION
SUBMITTED TO THE FACULTY OF THE GRADUATE SCHOOL
OF THE UNIVERSITY OF MINNESOTA
BY

Michael Bryce Milligan

IN PARTIAL FULFILLMENT OF THE REQUIREMENTS
FOR THE DEGREE OF
Doctor of Philosophy

Shaul Hanany

May, 2011

Acknowledgements

There are many people who have earned my lasting gratitude over the past (too many) years. To compile an exhaustive list would be both tedious and inevitably uncharitable to those I fail to mention. Forgive me, then, if I stick to generalities except for those few cases who, perhaps, don't know who they are.

The EBEX project itself is a collaboration of dozens of individuals, without whom this wonderful contraption we have built could not exist. I have been delighted to call them colleagues and friends, and I especially tip my hat to those of you who shared with me the ups and downs of our field campaigns in Nevis, NY, Ft. Sumner, NM, and Palestine, TX. And behind all of us, I recognize the family and friends who cheer on our successes, lighten the setbacks, and tolerate the strange hours and long absences that come with experimental astrophysics. Not least my own family and friends, who never seem to give up on me even when I quite shamefully neglect them!

I appreciate all the people who have been guideposts on the path that led me here. Early on, Moises Sandoval and later Jim Fraser nurtured in me a taste for doing an experiment to untangle the nature of the world. Also: the raft of educators who put up with my prodigious need to know things; the many people who make possible school, regional, and larger science fairs; everyone who, in the early years of personal computers, let me poke about and explore theirs. Thanks to the Meyer group at the University of Chicago for introducing me to TopHat and my first peek at scientific ballooning, and to the GriPhyN project collaborators, especially James Annis at FNAL, for showing me around the world of high performance computing.

The past eight years have been trying at times, so many thanks to the people who helped keep it fun, especially: Jeff Knoll, a marvelously undemanding roommate; Miriam Quintal and other residents of Beit Clore, who kept me company for a year in a distant land; the Judges and participants over the years of the University of Chicago Scavenger Hunt, the other really long-running game in my life; my fellow graduate students in the astronomy program.

EBEX is principally funded by NASA, and the staff of the Columbia Scientific Balloon Facility have energetically supported us throughout. I have personally received support from the Minnesota Space Grant Foundation. Our colleagues in the BLAST project originally developed important parts of the core flight hardware and software we use. We acutely feel the loss of our late colleague Huan Tran.

Dedication

For the sheer pleasure of finding things out.

Abstract

The E and B EXperiment (EBEX) is a balloon-borne telescope designed to map the polarization of the cosmic microwave background (CMB) and emission from galactic dust at millimeter wavelengths from 150 to 410 GHz. The primary science objectives of EBEX are to: detect or constrain the primordial B-mode polarization of the CMB predicted by inflationary cosmology; measure the CMB B-mode signal induced by gravitational lensing; and characterize the polarized thermal emission from interstellar dust. EBEX will observe a 420 square degree patch of the sky at high galactic latitude with a telescope and camera that provide an $8'$ beam at three observing bands (150, 250, and 410 GHz) and a $6.2°$ diffraction limited field of view to two large-format bolometer array focal planes. Polarimetry is achieved via a continuously rotating half-wave plate (HWP), and the optical system is designed from the ground up for control of sidelobe response and polarization systematic errors.

EBEX is intended to execute fly or more Antarctic long duration balloon campaigns. In June 2009 EBEX completed a North American engineering flight launched from NASA's Columbia Scientific Ballooning Facility (CSBF) in Ft. Sumner, NM and operated in the stratosphere above 30 km altitude for ~ 10 hours.

During flight EBEX must be largely autonomous as it conducts pointed, scheduled observations; tunes and operates 1432 TES bolometers via 28 embedded Digital frequency-domain multiplexing (DfMux) computers; logs over 3 GiB/hour of science and housekeeping data to onboard redundant disk storage arrays; manages and dispatches jobs over a fault-tolerant onboard Ethernet network; and feeds a complex real-time data processing infrastructure on the ground via satellite and line-of-sight (LOS) downlinks.

In this thesis we review the EBEX instrument, present the optical design and the computational architecture for in-flight control and data handling, and the quick-look software stack. Finally we describe the 2009 North American test flight and present analysis of data collected at the end of that flight that characterizes scan-synchronous signals and the expected response to emission from thermal dust in our galaxy.

Contents

List of Tables

List of Figures

Chapter 1

Introduction

For nearly a thousand years humanity has been engaged in a project of exploration and discovery that has steadily expanded to both encompass the Earth and look beyond it. Over much of that period the emergent study of physics progressed hand in hand with astronomy as when, for example, observations of planetary motion collected between the 11th and 17th centuries directly helped give rise to the theories of Newtonian gravity and classical kinematics.

Our present era is somewhat remarkable in this regard in that our gaze has at last reached the boundaries of the theoretically observable universe. In the century since the Great Debate about the nature of the spiral nebulae[1, 2] the frontier of our knowledge has expanded from a the island universe of a single galaxy almost to the doorstep of the Big Bang. In 1965 the reach of astronomy, at least in the electromagnetic spectrum, achieved its ultimate limit when the radiometer of Penzias and Wilson[3] registered an excess antenna temperature interpretted by Dicke and others[4] as the blackbody radiation expected in a universe theorized to have expanded from a primordial hot and dense state. This radiation now called the Cosmic Microwave Background (CMB) arises from the surface of last scattering, ~ 380000 years after the Big Bang, when free electrons were bound into atoms and the photon mean free path became large compared to the Hubble length. In principle no photon can reach us from beyond this surface or, equivalently, from earlier than this epoch.

The past two decades have been called a golden age of cosmology because detailed observations of the CMB and other probes of the large scale structure of the universe have yielded a wealth of data and permitted the construction of cosmological models with precisely determined parameters. As a result, we can for the first time propose answers informed by reason and observation to the very largest questions, those pertaining to the nature and origin of the universe itself.

1.1 Science overview

The E and B EXperiment (EBEX) is balloon-borne microwave polarimeter designed to study the polarization of the cosmic microwave background (CMB) and the foreground emission of thermal dust in our galaxy[5, 6]. These measurements will: detect or constrain the primordial B-mode polarization of the CMB, a predicted signature of gravity waves produced by cosmic inflation[7, 8]; characterize the polarized foreground dust emission, which is a necessary step in determining the CMB B-mode signal[9, 10]; and measure the predicted effect of gravitational lensing on the CMB[11]. The science goals of EBEX are described more fully in other publications [5, 6, 12].

1.2 Scope of this Work

EBEX is the product of a large collaboration and has posed many and varied challenges that have been ably tackled by my collaborators. This document makes no attempt to systematically discuss their efforts, but will endeavor to point the reader to further discussion as appropriate. As a dissertation in support of this author's graduate program, the only topics discussed in full detail are those which posed problems with which I have been intimately involved.

The immediately following chapters give a very general overview of the scientific questions that gave rise to the EBEX project, the EBEX instrument, and the 2009 test flight. Following that are several chapters addressing certain aspects in greater depth.

This author began his involvement with the EBEX project by developing candidate designs for the optical system of the telescope and analyzing those designs with physical optics and ray tracing packages. While the final optical design for EBEX was constructed by the late Huan Tran, this author's work continued to involve analysis of the built design, especially with respect to modeling instrumental polarization, modeling sidelobe response expectations, optimizing broadband antireflective coating strategies, and simulating the focal plane imaging performance. This work is discussed in Chapter 4.

The EBEX flight software–both the code running on the flight computers and software running in real time on the ground–evolved from code contributed by the BLAST project[13], parts of which were developed by BLAST researchers[14], while other components have a long heritage. That software infrastructure has grown considerably as we adapted it to meet the needs of this experiment. Having come to EBEX with significant software engineering and systems architecture experience, by 2009 this author was responsible for coordinating much of that work. Besides the routine, if sometimes challenging, tasks of system administration, source code management, and occasional digital disaster recovery, this author helped directly develop several components of the EBEX software architecture or *cyberinfrastructure*. As described in Chapter 5 these include significant enhancements to the flight control program, downlink system, and the chain of real-time data handling and analysis tools.

After the 2009 integration campaign and test flight various types of data collected were assigned to different members of the EBEX collaboration for in-depth analysis. Polsgrove has considered pre-flight calibration data[15], Hubmayr has examined the characteristics of the bolometers and DfMux readout system[16], Reichborn-Kjennerud has looked at thermal and pointing performance data[17], and Sagiv has investigated the behavior of the timing, housekeeping, and calibrator flash systems[18]. This author elected to analyze the data produced during the dipole scan at the end of the test flight, as described in Chapter 6, to search for response to astronomical signals from either the CMB dipole or dust features near the galactic plane.

Chapter 2

Overview of the EBEX Instrument

In order to provide context for the chapters that follow, we present here the science goals and experimental approach of EBEX, and summarize the design of the EBEX instrument.

2.1 Science Goals

Fig. 2.1 presents the theoretical E and B-mode power spectra of cosmological origin. The E-mode arises from Thompson scattering in the same scalar perturbations that give rise to the temperature power spectrum, is well-predicted by theory, and has been observed by several experiments at this point[19, 20].

Scalar perturbations cannot generate B-mode polarization. Instead, a primordial B-mode is expected to arise from gravitational waves, which manifest as tensor perturbations, and are predicted in many models of inflation. In this figure the tensor-to-scalar ratio $r = 0.1$. A detection of the primordial B-mode at any level would constitute strong evidence for the inflationary paradigm, and would provide information about new physics by fixing the energy scale of inflation. A non-detection at this level would be scientifically useful as a constraint on theory.

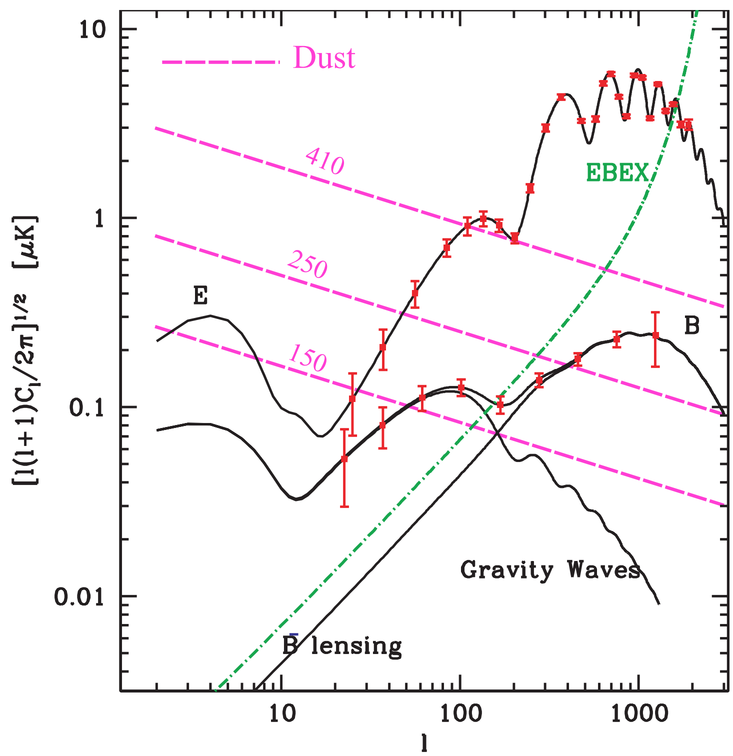

Figure 2.1: Theoretical E and B-mode polarization power spectra, assuming $r = 0.1$ (solid black lines) and predicted error bars (red) yielded by a 14-day Antarctic EBEX flight observing at high galactic latitude. Note that the predicted B-mode level includes anticipated contributions both from the theorized inflationary gravity wave signal and from gravitational lensing of the CMB. The dashed lines (pink) indicate the expected foreground contamination level from dust emission in the EBEX observing patch at each band. The dot-dash line (green) indicates the EBEX pixel noise level.

2.2 Experimental Approach

In order to improve on current measurements, EBEX has been designed around three organizing objectives: achieve high sensitivity; enable precision foreground subtraction; and effectively mitigate sources of systematic error.

2.2.1 Sensitivity

EBEX is made possible in part by recent advances in detector fabrication technology that allow lithographic construction of large arrays of bolometers. The ability to assemble a focal plane made of such arrays permits a dramatic increase in detector count from the previous generation of experiments.

The EBEX receiver is designed to accomodate 1920 transition edge sensor (TES) bolometers at a bath temperature of 270 mK with sufficient cryogen hold time for an 11-day Antarctic Long Duration Ballooning (LDB) flight. Because of limitations in the readout system it is only possible to operate 1400 to 1700 of these bolometers, depending on the continuing implementation of multiplexing technology. By scanning a ~ 350 square degree field EBEX will reach 1.2 μK sensitivity per pixel in the Q and U Stokes parameters in the course of one such flight.

2.2.2 Foreground Subtraction

Data from WMAP and other experiments demonstrate that polarized thermal emission from galactic dust will dominate the primordial B-mode in almost all regions of the sky and at all of the EBEX bands. Signals from polarized foregrounds must be subtracted in order to successfully estimate the inflationary B-mode signal. No experiment to date has measured the polarized foreground emission with sufficient precision, so EBEX will have to make this measurement in conjunction with observing the CMB.

For this reason, EBEX is designed with three widely separated observing bands centered at 150, 250, and 410 GHz. At these frequencies, thermal emission from dust is expected to be the only significant foreground component, and the two higher bands provide significant leverage to characterize the polarized intensity and spectral index, while the CMB is comparatively brighter at 150 GHz. By combining data from these three bands it will be possibe to model and subtract the dust foreground to the required sub-μK level.

2.2.3 Systematic Error Mitigation

EBEX uses the continuously rotating half-wave plate (HWP) method of polarimetry. In this approach, polarized signals entering the telescope are modulated to four times the HWP rotation frequency, and thus the information of interest is kept far removed in frequency from $1/f$ noise and potential sources of interference at the scan frequency or HWP rotation frequency. This method has an extensive legacy in millimeter and infrared polarimetry.

One purpose of the reimaging optics in the EBEX receiver is to provide a cold aperture stop that clips the Gaussian beams of the focal plane feed horn arrays. This method, combined with oversized telescope mirrors and absorptive baffles to intercept stray light, provide strong suppression of far sidelobe response. Our analysis of potential sources of polarized emission indicate that we must have knowledge of any sidelobe response above -85 dB relative to the main beam, and during integration in Ft. Sumner we failed to find any far sidelobe response at that level.

2.3 Instrument Overview

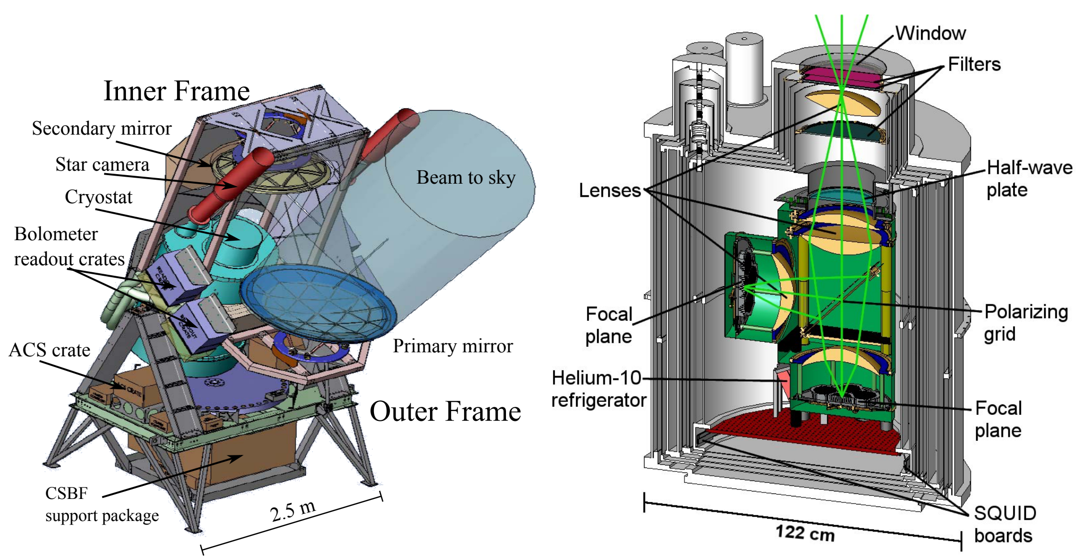

Figure 2.2: Left: schematic view of the EBEX gondola. Right: cutaway view of the EBEX cryostat. Major components of each are labelled. Note that on the gondola the flight computer crate and disk pressure vessels occupy the same position as the ACS crate on the far side of the outer frame.

Fig. 2.2 presents a schematic view of the construction of the EBEX instrument, showing the broad layout of the payload and a cutaway view of the receiver cryostat.

The EBEX instrument consists of a 1.5 meter clear aperture Gregorian-type telescope that feeds a cryogenic receiver, all of which are mounted on the inner frame of the EBEX gondola. Pointing control is maintained by driving the inner frame in elevation, while a pivot and reaction wheel turn the outer frame azimuthally relative to the balloon flight line. Attitude sensors including a sun sensor, star cameras, differential GPS, gyroscopes, magnetometer, and clinometers are mounted as appropriate on the inner and outer frames. The flight computers, Attitude Control System (ACS) crate, and disk storage pressure vessels are mounted on the outer frame. Inside the cryostat reimaging optics focus the input radiation onto two focal planes each carrying up to 960 transition edge sensor (TES) bolometers, up to 1920 total bolometers. A polarimetric system, consisting of a half wave plate (HWP)[21] spinning on a superconducting magnetic bearing[22] and a wire grid, modulates polarization information into the phase and amplitude of the component of the radiation intensity at the focal plane corresponding to four times the HWP rotation frequency[23]. The TES are read out through SQUID amplifiers via a frequency domain multiplexing scheme that connects up to 16 TES to each SQUID. The SQUIDs in turn are connected in groups of four to digital frequency-domain multiplexing readout (DfMux) boards[24]. The design of the EBEX instrument is detailed elsewhere [6, 17, 25], and the bolometer readout system is described in Hubmayr et al[26] and Aubin et al[27]. EBEX completed a 13 hour engineering flight from Ft. Sumner, New Mexico in June 2009.

Chapter 3

The EBEX North American Engineering Test Flight

3.1 Overview

The first flight of the EBEX payload was an engineering test flight which launched from Ft. Sumner, NM on June 11, 2009, at 14:01:48 UTC (8:01 a.m. local time). The balloon reached a maximum altitude of 36.065 km above sea level at 17:21 UTC, and remained at float until very shortly after 3:40 UTC on June 12, for somewhat over ten hours at float. The flight path is illustrated in Fig. 3.1. This flight was prepatory to a future long duration science flight over Antarctica.

The goals of this flight were:

1. Evaluate the performance and thermal characteristics of onboard electrical and electronic components, both during ascent through the tropopause and in a low-pressure, sunlit stratospheric environment.

2. Operate TESs for the first time in a space-like environment, and measure the in-flight noise properties of the bolometers and readout system.

3. Determine the sensitivity and operating parameters of our bolometers in a stratospheric environment, especially with respect to the greatly reduced atmospheric loading at float.

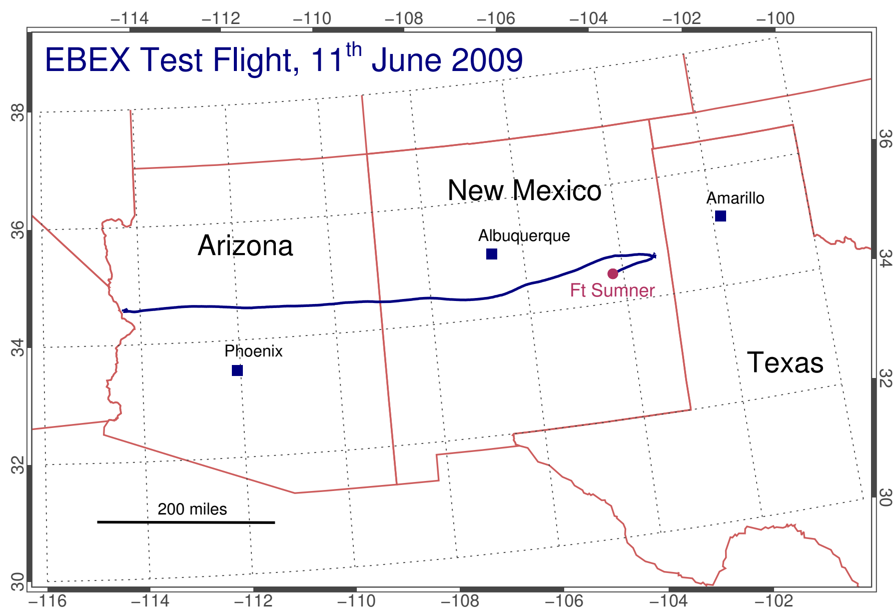

Figure 3.1: Flight trajectory of the EBEX North American test flight, as determined by GPS readings. Launch was from Ft. Sumner, NM. Termination and landing took place near Yucca, AZ. (Figure courtesy of Samuel leach.)

4. Validate the design and alignment of the telescope optics by acquiring an astronomical source and making a beam map.

5. Validate the autonomous control and remote operation capabilities of the flight software, flight computers, and attitude control system.

6. Demonstrate in flight the planned data flow, including real time downlink and data handling on the ground, and logging redundant copies of all science data on the payload.

7. Assess the mechanical performance of the cable supported EBEX gondola in flight, and the ability of the attitude control system to point the gondola.

The characteristics of the North American test flight, and the outcome of that flight with respect to thermal, electrical, and pointing performance (corresponding to goals 1 and 7) are documented comprehensively by Reichborn-Kjennerud[17].

Regarding goals 2 and 3, a subset of the eventual detector arrays were operated during the test flight. The expectations and in-flight performance of the SQUIDs and bolometers are documented by Aubin et al[27].

With respect to goal 4, the design of the telescope optics is discussed in detail in Chapter 4, but the evaluation of that design is not addressed in this document. Polsgrove[15] has described the efforts to evaluate and calibrate the instrument on the ground pre-flight. The instrument did not successfully acquire a point source calibrator during the test flight, and thus no beam map can be made from flight data.

Goals 5 and 6 pertain to the cyberinfrastructure of the EBEX project, and are addressed in Chapter 5.

3.2 Timeline of the Flight

The plan for the North American test flight included: pointing to bright stars to calibrate the star camera pointing; executing raster scans across Saturn to make beam maps, and in low dust regions of the sky to simulate science scans; and executing scans with large azimuth throw to calibrate on the CMB dipole and look for instrumental sidelobe response.

The elevation actuator buckled during launch[17], and the boresight pointing became permanently set at $\sim 15^\circ$ elevation. This unanticipated event invalidated the schedule stored on the flight computers, because while the pointing code can operate with elevation control signals uncoupled from the actual instrument pointing, most scheduled pointed operations lost their scientific utility without access to higher elevations. Instead, we controlled the instrument in real time via commands sent from the ground either by operators at the launch site or by operators (including this author) at a small downrange station in Winslow, AZ.

In addition to the failure of the elevation actuator, real-time pointing control of the instrument was compromised by inability to determine its true azimuth attitude. Leading to this condition were: the magnetometer readings were off by about 11°; the star cameras were saturated and unable to solve sky images after sunrise; the sun sensor did not yield useful azimuth data; sticking of the pivot joints caused intermittent stalls or undesired gondola azimuth motions. These conditions are all fully described by

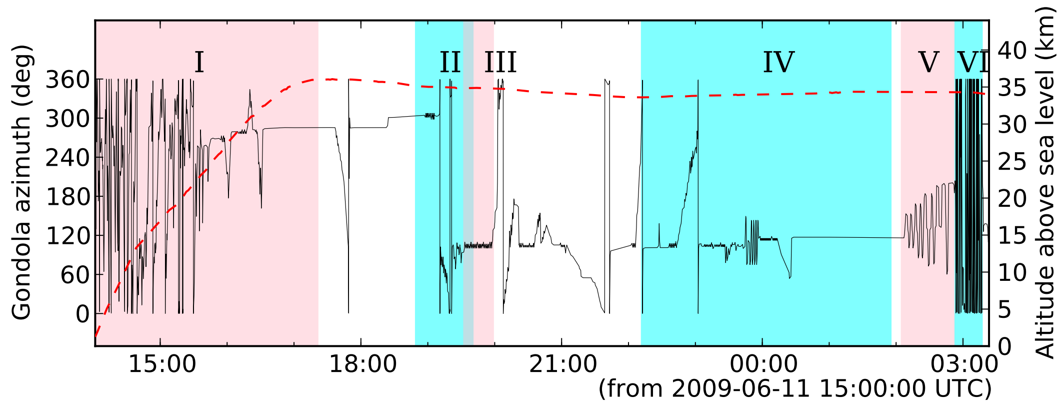

Figure 3.2: Phases of activity executed by the EBEX payload during the North American test flight, from launch time to the end of data logged by the flight computers. The thin black line plots the best reconstruction of gondola azimuthal pointing, and the red dashed line plots payload altitude above sea level. The shaded ranges correspond to periods described in Table 3.1. Note that range II (bolometer tuning) and range III (the Saturn scan) partially overlap.

Reichborn-Kjennerud[17]. It should be noted that the payload attitude has been successfully reconstructed post-flight[28], and unless otherwise noted all results presented here that derive from gondola azimuth refer to this reconstructed solution.

The timeline of actions actually taken during the test flight is tabulated in Table 3.1, and events of significant duration are referenced against the reconstructed gondola azimuth pointing and payload altitude in Fig. 3.2. During the first phase of ascent (segment I in Fig. 3.2) the gondola spun continuously to keep the pivot motor sufficiently warm in the cold tropopause. After that point we attempted to keep the instrument pointed at least 90° away from the sun at all times, although because of the pointing difficulties mentioned above the instrument still rotated past the sun on a few occasions. The pointing of the instrument is compared to the azimuth of the sun in the left panel of Fig. 3.3.

Because the cameras were saturated and none of the planned guide stars were at very low elevation, no effort was made to point to bright stars. Moreover, because the instrument elevation was fixed, the only opportunity to scan across Saturn would come just two hours after reaching float altitude when its path across the sky would take it through 15° elevation. Therefore the first priority was to tune the detector arrays (due

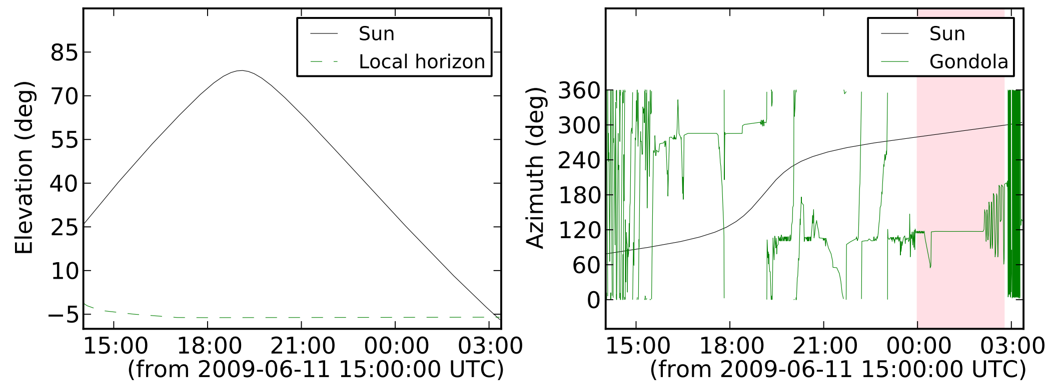

Figure 3.3: Elevation and azimuth of the sun during the NA flight. At left, the sun's elevation is compared to the elevation of the apparent geometric horizon at the altitude of the balloon, which is approximately $-6°$ for most of the flight. At right, the sun's azimuth is compared to the pointing of the gondola. The shaded region signifies the period during which the elevation of the sun is within 15° of the fixed gondola elevation pointing of $\sim 15°$.

to the dramatically higher atmospheric loading at sea level, this step could not be taken until after ascent), as described by Aubin et al[27]. The final phase of this operation, biasing the TESs into their superconducting transition (segment II in Fig. 3.2), finished slightly after the start of the Saturn scan (segment III). Unfortunately, because of the pointing uncertainty mentioned above, this scan did not overlap with the true position of Saturn.

After this, various pointing commands and scan modes were executed while operators attempted to diagnose and improve the behavior of the pointing system. About five hours after reaching float altitude, the focus of operations turned to gathering information about the performance of the bolometers. During this period (segment IV in Fig. 3.2) the gondola executed scans, primarily either 5° or 70° wide, to evaluate scan synchronous behavior, and at other times was left stationary while noise data were collected. As part of this process the bolometer biasing parameters were cycled through several variations. In the course of this process, a substantial fraction of the light bolometers that had been functional earlier in the flight became latched in a non-functional superconducting state.

Another reason for keeping the payload stationary during the latter part of segment

IV is that, as noted in the right hand panel of Fig. 3.3, the sun was close to the fixed boresight elevation during this time, and we did not wish to risk a pointing anomaly causing the instrument to point directly at the sun. However, once the sun was significantly below the boresight elevation but still above the horizon, a series of wide slews were executed to evaluate the sidelobe pickup of the instrument (segment V in Fig. 3.2).

As noted in the left panel of Fig. 3.3, the sun remained visible at float altitude almost until termination. However, the gondola baffling is designed to reject radiation from the Earth even when pointed to the lower elevation limit, so once the sun set more than 15° below the boresight it became safe to point towards the sun. At this time we set the gondola in constant rotation (segment VI) to obtain maximum sensitivity to the CMB dipole. Because stratospheric winds are relatively fast late in the spring ballooning season, the payload was by this point in western Arizona (see Fig. 3.1). Because Federal Aviation rules prohibit CSBF balloons from descending through California airspace, there was only time to execute this scan for about 23 minutes. Once the gondola achieved a stable rotation speed of about $16°/s$ it executed 40 full rotations. The data from this scan are analyzed in detail in Chapter 6.

Finally we executed the shutdown procedures for the instrument and collected post-sunset images with the star cameras while (with some urging from CSBF personnel) we readied the payload for termination. The HWP was stopped and secured by 3:23 UTC, and the flight computers stopped logging data due to shutdown of the disk arrays at 3:29 UTC. CSBF sent the termination command detaching the payload from the balloon at 3:40 UTC, and received data from the CSBF GPS until 3:55 UTC at 41,714 ft altitude. The payload was found the next day near Yucca, AZ.

Code[a]	Time (UTC)	Duration	Description
I	06-11-2009 14:01:48	3.32 hour	Launch and ascent to maximum altitude
	∼17:21		Maximum altitude at 36.065 km
	17:25:26	17.58 min	SQUID heating, bolometer sampling settings changed during operation
II	18:49:23	50.75 min	Bolometer tuning for float
	18:57:34		Begin pointing adjustments prepatory to Saturn scan
III	19:32:40	25.73 min	Saturn scan
	20:21:13		Begin anti-sun pointing
	20:24:44	12 min	5° anti-sun scans
	20:26:51		First calibrator LED flash, recurs every 15 minutes
	20:36:27		Pointing parked anti-sun
	20:58:44	12.5 min	5° anti-sun scan
	21:11:13	2.55 hour	Scanning stopped, various pointing operations
IV	∼22:12	3.72 hour	Bolometer tuning and noise testing
	23:44:23	11.77 min	Wide scans: ∼70° azimuth slews
	23:57:05	19.7 min	5° anti-sun scans, sun ∼ 30° elevation
	06-12-2009 00:16:47		Scanning stopped, pointing parked anti-sun for sunset
	∼01:55		End of bolometer noise tests, many bolometers latched at this point
V	02:05:27	46.15 min	Wide slew sequence for sidelobe response testing
VI	02:53:15	23.55 min	CMB dipole scan (with manual pivot control)
	03:17:17		Start of HWP shutdown procedure
	∼03:18		Sun fully below local horizon
	03:23:02		HWP stopped, re-gripped, encoders off
	03:29:15		Last log entries from flight computer

[a]Refers to labels on shaded boxes in Fig. 3.2

Table 3.1: Timeline of activities executed by the EBEX payload during the North American test flight.

Chapter 4

EBEX Telescope Optical Design and Analysis

In a fundamental sense, EBEX is an alt-azimuth mounted telescope for millimeter wavelengths. The ultimate design of that telescope was finalized in large part by the late Huan Tran, who brought with him years of experience designing other submillimeter telescopes. This chapter is dedicated to him.

This chapter will first describe the concerns that drove the optical design to its final configuration, and provide a detailed description of that design. Note that Chapter 2 provides an overview of the entire EBEX instrument, which establishes the broader physical context for the optical system.

Following sections will address specific problems that prompted further research on the part of the author. This is not meant to be an exhaustive listing of all research problems relating to the EBEX optics. By way of example, this chapter contains no discussion of the mechanical optical alignment procedures, as the author was largely uninvolved in the development of same, and no discussion on the development of the achromatic half-wave plate (AHWP), which has been discussed elsewhere[21].

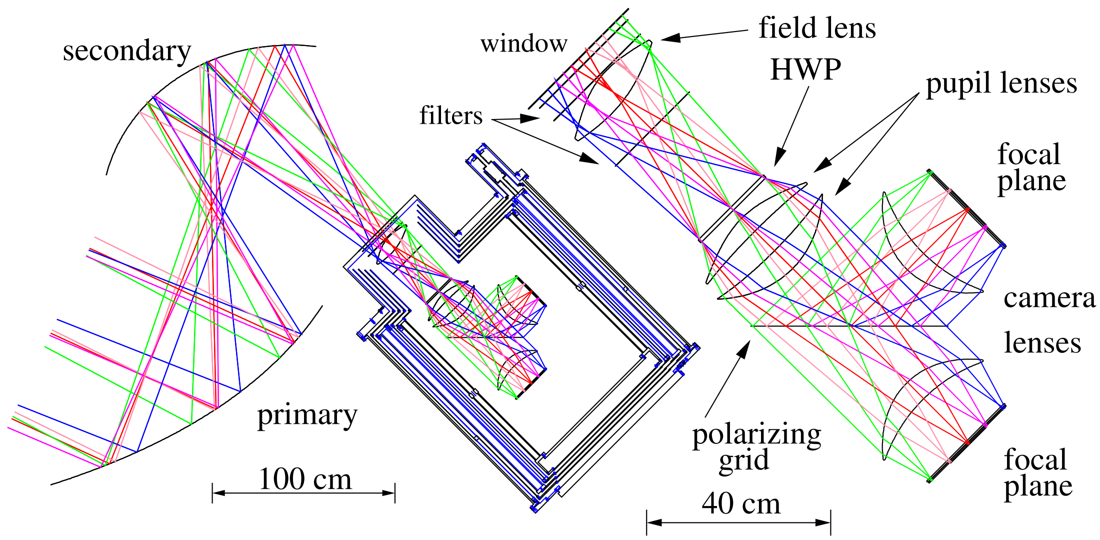

Figure 4.1: Ray tracing schematic of the EBEX warm and cold optical design. Left, the full optical system overlaid on a schematic of the EBEX receiver cryostat for scale, showing how light arrives from the sky at the primary mirror and is focused by the warm optics onto the field stop near the cryostat window. Right, a zoom on the cold optics, which reimage the Gregorian focus onto the two focal planes, and provide a cold Lyot stop at the HWP. Also noted are the infrared blocking filters. The band defining filters are mounted flush to the focal plane arrays.

4.1 Design Constraints

4.1.1 Frequency bands

EBEX observes in three bands centered near 150, 250, and 410 GHz. This range was chosen principally to enable foreground subtraction, by providing significant leverage on the spectral index of thermal dust emission, while minimizing the foreground contribution of galactic synchrotron radiation. The wide range of wavelengths requires achromatic optics, particularly with regard to antireflective coatings and the half-wave plate. The choice of specific band centers proceeds from the constraints of atmospheric absorption and the limits of achromatic behavior achieved in the AHWP.

4.1.2 8 arcmin beam size

We chose a beam size of 8 arcmin to ensure that EBEX can probe the angular scales at which gravitational lensing is predicted to produce B-mode polarization. In order to achieve this at the lowest frequency, 150 GHz, by the Rayleigh criterion

$$\sin\theta \approx \theta = 1.22\frac{\lambda}{D} \tag{4.1}$$

the effective entrance aperture must be at least 1 m.

4.1.3 Low sidelobe contamination

Far sidelobes–unmapped instrument response far from the beam–can produce serious systematic errors[29], especially for a polarization experiment since scattered diffracted radiation may be strongly polarized. Several design criteria flow from this requirement: the instrument must feature an unobstructed aperture; the reflectors must be oversized by 20% or more, and the receiver must include a cold aperture stop (and thus, reimaging optics).

4.1.4 Flat, telecentric focal plane

EBEX achieves greater sensitivity than past experiments in part by increasing the total number of detectors[5]. This is now feasible because of the development of bolometer arrays fabricated on wafers using lithographic techniques. The use of wafer arrays (and planar feedhorn arrays to efficiently couple them to incoming radiation) creates two constraints on the optical design of the resulting system: the final focal plane must be flat and telecentric.

4.1.5 Polarizing grid at $45°$ and two focal planes

To further increase the potential number of detectors, the EBEX design detects radiation both transmitted and reflected by the polarizing grid at two separate focal planes (see Fig. 4.1, right panel). The design of the reimaging optics must provide sufficient path length for a beam split, which precludes some more compact designs.

4.1.6 Large, diffraction limited field of view

Effective use of large format detector arrays requires that the optics provide a large, diffraction limited field of view (DLFOV). This implies a low $f/\#$ system, a goal that is in tension with the above constraint on path length, and aspheric optics to control abberations at large field angles.

4.1.7 Good polarization performance

Any practical optical system will create some level of instrumental polarization, defined as partial conversion of unpolarized incident radiation into linearly polarized radiation. Similarly, any system will exhibit some instrumental rotation of the polarization vectors of incoming light, or cross-polarization response, at least for off-axis fields. These effects will have to be removed in post-flight processing by precise calibration of the instrument. However, a desirable optical design will minimize these effects, to reduce the amount of observing time that must be spent collecting calibration data in order to remove them to a suitable level. According to our simulations, we can tolerate a systematic uncertainty in polarization angle in the final sky maps of no more than 0.3°.

4.2 EBEX Optical Design

The overall optical design of the EBEX telescope is outlined as a ray-tracing schematic in Fig. 4.1, which shows a Gregorian Mizuguchi-Dragone reflecting telescope with precision machined aluminum reflectors, coupled via a window to a cryogenic receiver containing five ultra-high molecular weight polyethyleye (UHMWPE) lenses making up the cold reimaging optics, and two focal planes.

Incoming radiation is collected by the 1.5 m parabolic primary mirror, transfered via an ellipsoidal secondary, and forms the Gregorian focal plane about 10 cm behind the cryostat window. Just behind the window a field lens creates an image of the primary aperture at the cold Lyot stop, which is coincident with the HWP. Past the HWP a pair of pupil lenses collimate the ray bundle, which is split by a linear polarizer. Finally a camera lens on each optical branch forms the final flat, telecentric focal plane at the feedhorn array. This design provides diffraction-limited $8'$ beams at all bands across a 6.2° field of view.

The reflectors and cryostat are mounted on the gondola inner frame and surrounded by nearly light-tight baffles that are reflective on the outside and absorptive black inside. The baffling as configured for the North American flight can be seen in Fig. 4.4. The design of the outer frame baffles and wings will change modestly for the Antarctic flight due to the lower Sun elevation and the presence of solar panels mounted to the rear of the gondola.

4.2.1 Warm Optics: Telescope

Fundamental parameters		Derived parameters	
f_e	198 cm	a	110.2017 cm
D_p	105 cm	b	98.206 cm
f_p	80 cm	c	50 cm
α_d	12.767782°	K	-0.205856
y_{off}	100 cm	θ_f	$-33.159756°$
		Θ_s	52°

Table 4.1: Optical parameters of the EBEX Gregorian telescope. Five fundamental parameters define the geometry of a Gregorian telescope. Also tabulated are several useful parameters that can be derived from these fundamental parameters. The choice of which five to consider fundamental is somewhat arbitrary. Refer to the text of Sec. 4.2.1 for definitions of the variables above, and see Fig. 4.2 for a graphical representation connecting these variables to the telescope geometry.

The EBEX warm telescope is an off-center $f/1.9$ Gregorian design. This design provides several advantages:

- Offsetting the optical axis from the primary symmetry axis provides an unobstructed aperture, as desired for sidelobe and systematic error control.
- The Gregorian design produces a real field stop between the primary and secondary mirrors, which allows for good stray light rejection by mostly enclosing the secondary mirror and cryostat with baffles.
- Using a relatively large secondary mirror–which would be problematic in an axial design where the secondary occludes the primary–permits constructing a fast system, as required to fit a large field of view through the cryostat window.

- This design allowed us to use the existing parabolic primary mirror from the Archeops experiment[30], saving somewhat on fabrication and testing costs.

Prior to committing to this design we also evaluated a scheme that used a crossed Dragone telescope, also known as a compact range or offset Cassegrainian antenna[31]. Such a telescope could be more compact overall, have lower intrinsic cross-polarization, and provide a larger DLFOV[32]. However, the crossed Dragone would require a substantially larger secondary mirror, and does not produce a real field stop, making baffling for stray light rejection much more difficult.

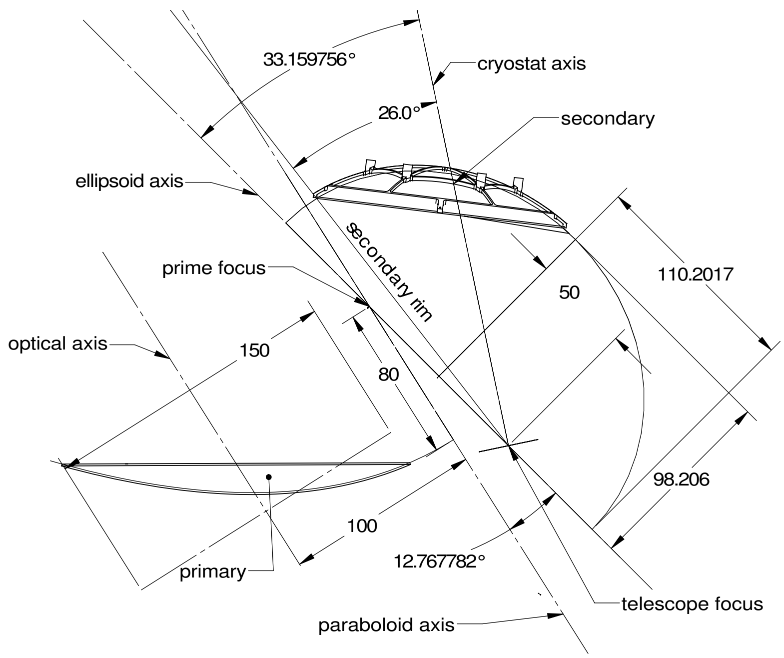

Figure 4.2: Geometry of the EBEX Gregorian-Dragone reflecting telescope. The off-center Gregorian design provides for an unobstructed aperture and low sidelobe response, and is reasonably compact. The specific parameters of this configuration are chosen to satisfy the Mizuguchi-Dragone condition for optimal polarization response, while allowing reuse of the pre-existing parabolic 1.5 m Archeops primary mirror. (Figure courtesy Huan Tran.)

The telescope geometry is presented schematically in Fig. 4.2, and the geometrical variables parameterizing this design are tabulated in Table 4.1.

There are five fundamental geometrical parameters that define the telescope. f_e is the effective focal length. D_p is the projected circular aperture diameter of the primary mirror. f_p is the focal length of the primary mirror paraboloid. α_d is the angle between the symmetry axes of the primary and secondary figures, which is chosen to satisfy the Mizuguchi-Dragone condition. y_{off} the offset between the primary symmetry axis and the aperture center.

Additional important parameters that can be derived from the fundamental parameters are: a, b, and $K = -e^2$ the semi-major and semi-minor axes, and conic constant of the secondary ellipsoid, respectively; c is half the inter-focal length of the secondary ellipsoid. θ_f is the angle between the secondary symmetry axis and the axis of a horn located at the secondary focus; and Θ_s the opening angle filled by the secondary mirror as viewed from the secondary focus.

Both the primary and secondary mirrors are oversized by about 40% relative to the aperture limits obtained by geometrical ray tracing. This is because we wish to minimize sidelobe pickup by intercepting scattered and spillover power and sending it to the sky in the direction of observation. Therefore, while the optical aperture diameter is 105 cm, the primary mirror has a circular aperture of 150 cm diameter.

4.2.2 Mizuguchi-Dragone Condition

It has been shown that every two-reflector system with conic surfaces has an equivalent paraboloidal single-reflector system that has the same aperture diameter and feed orientation[33]. In the case that

$$\tan\left(\frac{\theta_f}{2}\right) = \frac{e+1}{e-1}\tan\left(\frac{\alpha_d}{2}\right) \tag{4.2}$$

the equivalent single-reflector system is a rotationally symmetric, on-axis paraboloid. A system that satisfies this relation minimizes cross-polarization and exhibits low astigmatism, which provides a larger DLFOV. This relation is known as the Mizuguchi-Dragone condition[34, 35].

4.2.3 Cold Optics: Reimaging Camera

In principle a focal plane could be mounted directly behind the cryostat window and suitable filters, obviating the need for any refractive optics. However, several considerations prevent us from doing so in the case of EBEX:

- Our polarization modulation scheme calls for a rotating HWP and a polarizing grid to be placed in the optical path. It is not possible to fabricate a sapphire HWP as large as the current EBEX focal plane.
- We wish to have a cold aperture stop to control beam size and sidelobe sensitivity.
- Splitting the beam by polarization state immediately gains a factor of two in optical efficiency, by detecting rather than rejecting light reflected by the polarizer.

Instead we use a series of four lenses (five total, since there is one camera lens for each optical branch) to create a true aperture stop coincident with the HWP at the entrance to the 1 K optics box, and then create a second image with the same magnification and $f/\#$ as the Gregorian focus at each of the two feedhorn arrays. Also present are low-pass filters to reject thermal radiation and define the observation bands, which are detailed by Sagiv[18]. The cold optical chain is depicted on the right side of Fig. 4.1.

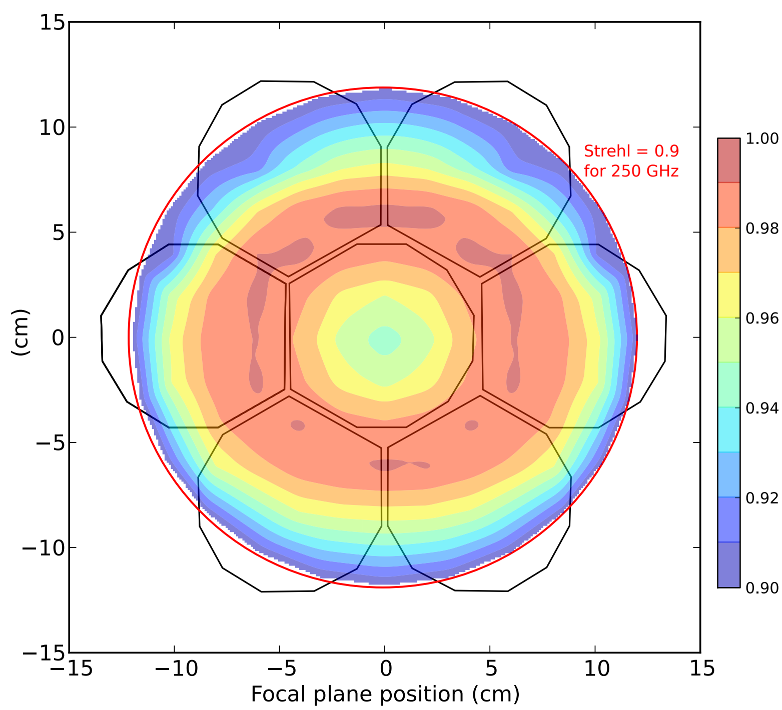

Figure 4.3: Wafer outlines in one focal plane, overlaid by a contour plot of Strehl ratios at 250 GHz. The central wafer is 410 GHz, the two at left and right are 250 GHz, and the four above and below the center are 150 GHz.

The lenses used are all manufactured from a single block of UHMWPE to ensure a consistent index of refraction. All lens surfaces are modelled as 14th-order polynomial aspheres, which were developed using design optimization codes in the ZEMAX[36] and Code V[37] optical design suites. According to ray tracing simulations of the RMS wavefront error at the focal plane, these lenses should provide a DLFOV with Strehl ratio above 0.9 across the entire focal plane at 150 GHz (extending about 3.6° from the boresight), and across the entire central wafer at 410 GHz. At 250 GHz the DLFOV forms an ellipse that extends between 3.40° and 3.48° from the boresight, overlapping about 80% of the detectors on the 250 GHz wafers, as shown in Fig. 4.3. Note that in any event, the unvignetted field of view only extends to 3.3° in elevation and 3.4° in azimuth from the boresight.

Ordinarily an instrument with fixed aperture size and several observing bands would exhibit beam sizes that scale with wavelength according to the Rayleigh criterion (Eq. 4.1), but in the case of the EBEX receiver this is cancelled out by another effect. Our feedhorn array uses smooth-walled conical horns of constant roughly 6 mm diameter for all three bands–note that this does not follow the $2f\lambda$ feedhorn spacing rule that is more usual[38, 13]. As a result, the aperture stop, and thus the entrance pupil aperture at the primary, is underilluminated by the amounts tabulated below. As the degree of underillumination scales with wavelength in the same way as beam size, the effects cancel and the instrument produces roughly constant beam size at all wavelengths.

Band	FWHM	Aperture taper
150 GHz	$7.76'$	-7.2 dB
250 GHz	$5.82'$	-19.4 dB
410 GHz	$5.02'$	-50.1 dB

Table 4.2: Edge taper at the aperture stop of the beams generated by the feedhorn array at each observing frequency. The tabulated FWHM is the beam size on the sky that would be computed purely from apodizing a circular Gaussian beam in this way, as computed by Huan Tran.

Figure 4.4: The EBEX payload with baffles deployed in Ft. Sumner. In this photo the instrument is standing on the launchpad in an open area to test sidelobe response using an RF source on a crane (not pictured). The large wings and box-like structure on the right make up the outer frame baffling, which prevent sunlight from directly impinging on the inner frame and electronics crates. The central tilted box and open scoop are the inner frame baffles, which move in elevation with the instrument, and reject stray light from the optical path.

4.3 Baffles and Sidelobe Rejection

The off-axis, or sidelobe, response of the telescope is important to characterize (and minimize) since it is in the sidelobes that spurious signals from the Earth, Sun, Moon, balloon, and Galaxy will appear. Of these sources, we have determined that the Galaxy can produce the largest spurious scan-synchronous signal (the Earth is brighter, but fortunately does not vary during a constant-elevation scan).

Using a GRASP8[39] simulation of the EBEX reflectors, we calculate an approximate upper limit of a 72 nK modulated signal, extrapolating to 150 GHz from WMAP 90 GHz Stokes I and Q for the galactic center, using worst-case sidelobe geometry and a conservative estimate of sidelobe polarization. By measuring the sidelobe response of the telescope to 85 dB below the on-axis response, we will be able to suppress the residual level of sidelobe contamination in the final maps to below 21 nK, which is the peak B-mode polarization signal expected for T/S a factor of five below 0.02. During the Ft. Sumner integration campaign we successfully characterized the far sidelobe response of the fully assembled EBEX payload to this level[15].

Based on the model described below, we decided to use absorptive baffles. In this case, the specific geometry of the reflector sidelobe pattern is less important, as the vast majority of spurious sensitivity is directed to the uniform unpolarized emission of the ambient temperature absorptive coating. The baffles as constructed for the North American flight are shown in Fig. 4.4. Note that, for thermal reasons, the baffles must still be reflective on outward-facing surfaces.

For the LDB flight we are considering moving to either reflective baffles or an open frame that allows spillover directly to the sky, in order to reduce emissive loading on the interior of the cryostat.

4.3.1 EBEX Sidelobe Model

As illustrated in figure 4.5, suppose four gain components generated by the EBEX reflector system. These are chosen from the results of a physical optics simulation of the EBEX reflectors, and approximate the sidelobes resulting from power that spills or diffracts past the primary reflector. These sidelobes are of considerable interest as they are difficult to contain within the gondola and must either be dumped to an absorptive

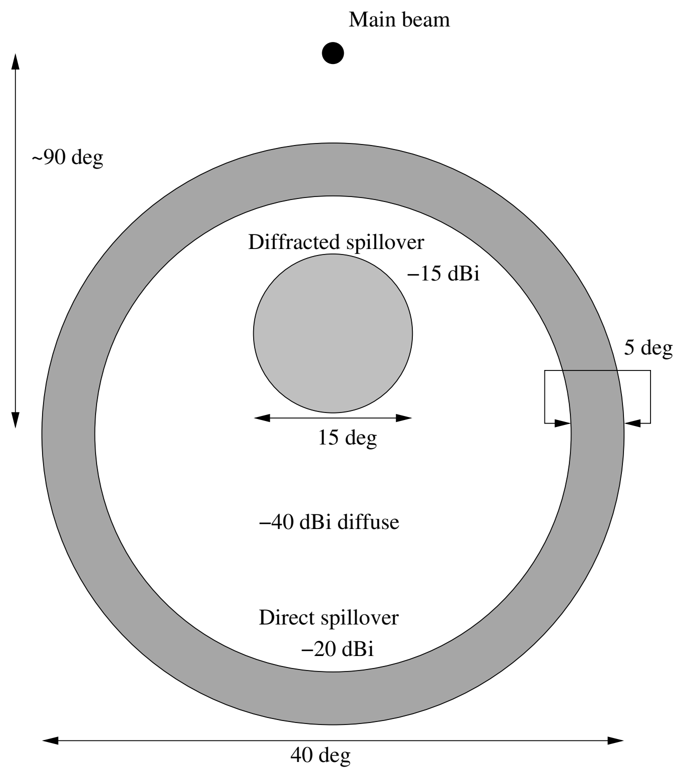

Figure 4.5: Schematic geometry of EBEX reflecting telescope sidelobe response in the absense of any baffling. In the far field, the telescope is sensitive to most of the sky at -40 dBi, but spillover past (the annular feature) and diffraction around (the circular feature inside the annulus) the secondary mirror creates areas of -15 to -20 dBi sensitivity. The main beam, the black spot at top (not to scale), by contrast features about +80 dBi sensitivity.

load or will illuminate the sky in an unpredictable fashion. Therefore, at no point does the position of these features relative to the main beam concern us, except to note that the sidelobes will not, in general, illuminate the same part of the sky as the main beam. Thus Table 4.3 encapsulates the relevant properties of this sidelobe model. Note that, in the case of the beam, the area and gain are representative quantities that satisfy the desired normalization, and approximate the FWHM of the real beam. See the formalism in Appendix B for more detail.

Component	A_j (sr)	G_j (sr^{-1})	A_jG_j
Diffuse	$4\pi = 12.6$	-40 dBi $= 10^{-4.0}/4\pi$	1.0×10^{-4}
Ring	$(5°)\,(2\pi \sin 20°) = 0.2$	-20 dBi $= 10^{-2.0}/4\pi$	1.5×10^{-4}
Disk	$\pi\,(7.5°)^2 = 0.05$	-15 dBi $= 10^{-1.5}/4\pi$	1.3×10^{-4}
Beam	$\pi\,(4\,\mathrm{arcmin})^2$	64.7 dBi $= 10^{6.47}/4\pi$	0.999

Table 4.3: Components of the sidelobe response model tabulated with area, gain, and $A \cdot G$ product.

4.3.2 Load from Absorptive Baffles

The simplest case to analyze is that where the interior of the gondola (via baffling or other means) is made fully absorptive at the frequencies of interest. In this case the sidelobes will intercept a uniform, unpolarized radiation emitter at ambient temperature. The relevant effect is to increase the power incident upon the detectors, with attendant loss of receiver sensitivity, and the metric of interest is the size of the contribution relative to the largest known source of incident power.

In the case of EBEX the largest such load will be thermal emission from the telescope reflectors, which will be at a temperature near 250 K and have emissivity ≈ 0.005, and will each thus emit like a 1.25 K blackbody that completely fills the main beam (but which nevertheless dominate the CMB load)[1] . To this we compare loading from the sidelobes: $\Delta T = \sum_s A_j G_j T \approx \left(4 \times 10^{-4}\right) \cdot 250\ \mathrm{K} = 0.1\ \mathrm{K}$. This suggests that, assuming all sidelobe power could really be absorbed inside the gondola by a uniform blackbody, the resulting increase in loading would be subdominant.

4.3.3 Reflective Baffles

The overarching assumption behind the use of reflective baffles is that multiple reflections will occur, so that the power in sidelobes is mapped in an unpredictable fashion onto the far field. In the generic case, sidelobe power may wind up anywhere on the sky, balloon, or ground. In practice, both the ground and the balloon are 200-300

[1] Generally in radio astronomy the brightness temperature T_b is large enough that $h\nu/kT_b \ll 1$. In the Rayleigh-Jeans regime specific intensity $I_\nu \propto T_b$. The 2.7K CMB is actually near the peak of its blackbody spectrum at our wavelengths, and thus has intensity about 30 times less than a source with thermodynamic temperature 300K and optical depth τ or emissivity ε of 1%.

Kelvin blackbodies with no azimuthal features, and thus contribute load but no scan-synchronous modulation during a constant-elevation scan. Therefore, we can consider sidelobes landing there as identical to the case of absorptive baffles, addressed above.

Suppose instead that sidelobe power lands on the sky, and the scan sweeps this power across bright sources on the sky. The change in load will be indistinguishable from an increase in the CMB temperature in that part of the scan. However, due to the low temperature of the sky and the suppression due to small overall sidelobe gain, this added load is insignificant relative to radiation from the reflectors. On the other hand, if the sources or the sidelobes are polarized the resulting change in polarized input intensity will be indistinguishable from, and possibly dominant over, polarization in the CMB.

4.3.4 Polarized Sources

From WMAP[40], the galaxy in W-band (at 90 GHz dust dominates the foreground signal as at our frequencies) reaches 3.6 mK intensity and $\sim 40\ \mu$K Stokes Q averaged over a $2^\circ \times 10^\circ$ region covering the galactic center in the plane. The bright disk of the galactic plane is on the order of 2° thick, but reaches across nearly the entire sky. Suppose the dust emission has a spectral index of 1.7 (it appears to actually be somewhat variable). Then extrapolated to 150 GHz we expect a brightness temperature of $(150/90)^{1.7} \times 3.6$ mK $= 8.6$ mK and an average Stokes Q of $\sim 95\ \mu$K. After examining the surface brightness of the LMC and a nearby HII region, we take this to be the largest possible source of polarized contamination.

To compute the resulting load suppose that at some scan position the disk sidelobe is mapped onto the sky so as to fully cover this region. In steradians, $2^\circ \times 10^\circ \approx 0.006$, so $d \approx 0.12$. Then this region will contribute to detector temperature as $\Delta T = G \cdot A \cdot d \cdot T = \left(1.3 \times 10^{-4}\right)(0.12)(8.6\,\mathrm{mK}) \approx 130$ nK, a totally negligible load. However the polarized load will be $\Delta Q = \left(1.3 \times 10^{-4}\right)(0.12)(95\,\mu\mathrm{K}) \approx 1.5$ nK, which is small but not necessarily negligible.

It is worthwhile to observe that this computation assumes a reflective remapping that preserves the area of this sidelobe. It is more plausible that the sidelobe would also be diffused in the process of scattering onto the sky, in which case the area would increase. This must conserve $G \cdot A$ but would cause d to shrink, further decreasing the overall contribution.

4.3.5 Reflective Polarization

Rays that scatter off of reflective surfaces on their way to the sky will naturally be partially polarized. In the case of the telescope reflectors the Dragonne optimization minimizes this effect. Moreover, since aluminum is highly conductive, only grazing-angle reflections will impart large polarizations. Since the gondola baffles are not optimized to null polarization, and since we do not *a priori* know the path that rays might take through the gondola to the sky, we cannot rule out this possibility. A simple model illustrates this case: we set up a pair of reflective flats in Code V[37], apply surface coatings to simulate aluminum, and propogate rays through them at various incidence angles. Thus each ray is reflected twice at the given angle, tabulated below:

Angle	20°	30°	45°	60°	70°	80°	85°
IQ	1.7×10^{-4}	3.8×10^{-4}	9.4×10^{-4}	0.0020	0.0034	0.0074	0.015

4.3.6 Total Contibution

Now assume that in the worst case scenario, the disk component of the sidelobe pattern falls onto the galactic center, after one grazing-incidence reflection off of the baffles that does not appreciably diffuse the sidelobe but does impart 1% polarization. Using the results from the preceeding sections, the total sidelobe contamination can be computed as

$$\begin{aligned}\Delta Q &= d \cdot A \cdot G\,[Q + 0.01T] \\ &= \left(1.6 \times 10^{-5}\right)[95\,\mu\mathrm{K} + 0.01 \cdot 8.6\,\mathrm{mK}] \\ &= 2.9\,\mathrm{nK}\end{aligned}$$

The stated EBEX sensitivity target requires that no systematic effect contribute a spurious signal larger than the B-mode intensity expected for T/S=0.004, five times below the EBEX target of T/S=0.02. This corresponds to a 21 nK polarized signal. This section shows that the largest probable far sidelobe contribution from reflective baffles falls below this threshold.

4.4 Broadband Anti-reflective Coatings

During the North American test flight the optical elements did not have anti-reflective coatings (ARCs). However, for the LDB science flight broadband ARCs will be essential for two reasons: without them internal reflections will reduce optical efficiency by 50% or more[16], and differential reflection will generate instrumental polarization.

4.4.1 Differential Reflection

Light impinging upon a dielectric material with non-normal incidence angle will experience differential polarized reflection. Many polymer materials, including UHMWPE, have an index of refraction near $n = 1.5$ at millimeter wavelengths. By the Fresnel equations[41], such a surface exhibits roughly 4% reflection for all polarization states at normal incidence. However, at an incidence angle of 30° the p-polarization will experience 2.5% reflection while the s-polarization experiences 5.8%, thereby imparting a 3% linear polarization to previously unpolarized light.

As is clearly visible in Fig. 4.1 most rays do not encounter the surfaces of optical components at normal incidence. However, because the ray bundles locally approximate rotational symmetry, some of this differential reflection will cancel, reducing the total polarization imparted to the transmitted light. The remaining conversion of unpolarized light into partially polarized light is termed the instrumental polarization of the optical system. However, EBEX is only sensitive to polarization that is modulated by the rotating HWP, so the quantity of interest is the instrumental polarization measured at the HWP.

4.4.2 Instrumental Polarization Model

To predict this quantity, we construct a simplified model of the EBEX optics in Code V[37], which contains the optical elements between the sky and the cold aperture stop at the HWP. Using the Code V ray tracing features, we can compute a pupil-averaged effective Mueller matrix for a given field position, and take the quadrature sum of the IQ and IU components as the instrumental polarization. By doing so at several frequencies around the band center construct a band averaged estimate of this quantity; we refer to this estimate as IP. Table 4.4 tabulates IP for various permutations of the simplified

Model	IP [%] vs Band		
	150 GHz	250 GHz	420 GHz
Reflectors only	0.0289	0.0369	0.0521
$\sqrt{n}$ ideal ARC	0.302	0.253	0.024
Available ARC w/o window+filters	0.89	1.50	0.06
Available ARC w/ uncoated films	2.13	2.74	0.58
Available ARC w/ coated films	1.46	2.22	2.25

Table 4.4: Instrumental polarization at the HWP tabulated by band as various components are added to the ARC model. The first line considers only the mirrors. At the second line the field lens is added with an ideal $\sqrt{n}$, $\lambda/4$ thickness coating applied for each band individually, approximating the theoretical performance of a maximally broadband ARC. In the third line one available ARC is applied to the field lens, and in the fourth line the same is done, and the window and filters are added to the model. In the final line an ARC is applied to the filters as well.

optical model as it is made more realistic. Here the "available ARC" refers to a particular somewhat arbitrary choice for the thickness of low-index coatings applied to the front and back surfaces of the field lens or other optical elements.

4.4.3 Optimized Broadband ARC

Because EBEX is only sensitive to polarization that is modulated by the rotating HWP, the element of most concern is the field lens. An ongoing research effort aims to develop a technique for fabricating a sub-wavelength index gradient structure on the surface of the field lens, but as of this writing this has not produced a satisfactory surface. In lieu of this technology, we aim to develop a broadband ARC using traditional methods that can be applied to all of the lenses, which will perform adequately for the field lens as well.

Because of the large range of wavelengths of concern, techniques involving multilayer coatings do not perform well. However, the simple expedient of applying coatings of different thicknesses to the front and back surfaces of our lenses has produced good results. The Ade group in Cardiff has developed the capability to bond UHMWPE with sheets of porous Teflon (PPTFE) of either 415 μm or 230 μm thickness, chosen to approximate $\lambda/4$ for 250 GHz and 410 GHz. By simulating IP for the four possible combinations of these coatings, Table 4.5 is obtained. Based on this result, we have

	IP [%] for field lens ARC applied			
Band (GHz)	thick-thick	thick-thin	thin-thick	thin-thin
150 GHz	0.78	2.67	1.22	3.12
250 GHz	2.21	1.82	1.82	1.43
420 GHz	1.07	1.07	0.53	0.52

Table 4.5: Instrumental polarization at the HWP tabulated by band and by broadband ARC applied to the field lens.

proceeded to apply the thinner coating to the sky-facing side of each lens, and the thicker coating to the reverse, with the goal of achieving the IP performance of the "thin-thick" column.

Chapter 5

Software and Cyberinfrastructure Supporting EBEX in Flight

5.1 Computing and system control requirements

In order to meet the science goals, EBEX autonomously executes several tasks in parallel.

The instrument maintains real-time pointing control to better than the $0.5°$ requirement and logs sufficient data from the pointing sensors to allow post-flight pointing reconstruction to better than the $9''$ requirement. The pointing system can realize several predefined instrument scan modes, as well as drift, slew, and coordinate tracking motions. The two redundant flight computers (see Sec. 5.3) execute all pointing actions synchronously, with a watchdog card selecting the less-recently rebooted computer to control the instrument. The pointing system is discussed in detail by Reichborn-Kjennerud[17].

Both SQUIDs and TES bolometers periodically require active tuning, such as during cycling of the sub-Kelvin adsorption refrigerators[42]. This instrument reads out up to 1792 of the possible 1920 bolometers, multiplexed through 112 SQUIDs, operated by 28 DfMux boards. These setup and tuning operations are managed over the gondola Ethernet network by the flight computers, as discussed in Sec. 5.4.

Bolometers are read out at 190.73 Hz as 16-bit samples. Depending on the multiplexing level each DfMux board reads out between 32 and 64 bolometers, producing a data stream of between 21 and 42 kilobytes/s, or 2.1 to 4.2 gigabytes per hour for the full complement of 28 boards. The ACS generates an additional data stream of approximately 20 KB/s (70 megabytes per hour), and the angular encoders on the rotating HWP produce a combined 21 KB/s (75 MB/h). This output data is transferred over the ethernet network to the flight computer and logged to disk. Consequently for a 14 day flight the onboard disk array must provide over 1.5 terabytes total storage per redundant copy written. The storage system is discussed in Sec. 5.5.

In addition to planned housekeeping operations, the possibility of unplanned events demands that EBEX possess the ability to respond to some exogenous contingencies, that sufficient operational data be downlinked to enable human diagnosis of unexpected conditions, and that the telecommanding interface be flexible enough to exercise the full range of recovery options available in the flying hardware. The necessary downlink (Sec. 5.6) is provided by a 1 Mbit/s line-of-sight (LOS) transmitter available for roughly the first day of flight, and a much slower TDRSS satellite relay afterwards. The telecommanding uplink relies on satellite relay or an HF-band LOS transmission, and in practice is limited to less than ten 15-bit command tokens per second.

All of the above activities can be triggered from the ground via uplinked commands, as well as scheduled via onboard schedule files. The scheduling system operates in local sidereal time, allowing planned observations to account for the motion of the balloon in longitude, which cannot be precisely known in advance. Within the limits of the underlying operating system, actions can be scheduled arbitrarily far in the future. Uplinked commands can select between alternative stored schedules.

The communications infrastructure of the Columbia Scientific Balloon Facility (CSBF) provides the LOS downlink signal at the launch site, and provides connections to satellite-based telemetry and telecommanding via the Operations Control Center in Palestine, Texas[43]. During a long duration balloon flight, many collaboration personnel will be positioned at the launch site, while other collaborators may be geographically dispersed. To support this scenario the EBEX ground segment couples uplink and downlink hardware to a client-server software stack (see Sec. 5.7 and Fig. 5.2). The full high rate LOS data stream is available at multiple client workstations at the launch site, and portions of this data can be made available via the public internet for remote real-time examination. Likewise telecommanding is forwarded over network links to the EBEX ground station and CSBF uplink.

To meet the reliability and development time requirements of this project we use commercially available hardware and existing software whenever practical. With the exception of the FPGA-based DfMux and ACS boards, onboard computers and networking hardware are available industrial embedded models which we have qualified in thermal and vacuum conditions approximating balloon flight. The ACS, many aspects of the gondola and pointing system design, and several components of the software chain described here originate with the BLAST project[13], and are described by Wiebe[14]. The housekeeping system makes extensive use of embedded monitoring boards[44] originally developed for the ATLAS experiment at CERN[45, 46].

5.2 Subsystems overview

The EBEX gondola comprises several subsystems of networked components, with the flight computer crate acting as the point of intersection.

An Ethernet network of industrial ring switches[47] connects the flight computers, disk storage system, bolometer readout boards, HWP encoder readouts, sun sensor, and star camera. This network is shown in Fig. 5.1. The use of ring switches provides resilience to network breaks or failure of a single switch. Optical fiber connections are used where electrical isolation is necessary.

The GPS receiver, multiple actuators, and the CSBF support package (which includes the commanding uplink and low rate satellite telemetry) communicate directly with the flight computers via serial ports. Additional sensors and controls connect directly to hardware in the ACS crate. The ACS communicates with the flight computers via a custom bidirectional bus termed the "E-bus."[14, 17]

Housekeeping monitoring and control is handled by custom boards equipped with embedded monitoring boards[46], which are connected by a Controller Area Network[48] bus (CANbus). The flight computers communicate with this network via Kvaser USB-CANbus adapters[49].

Because the housekeeping system, ACS, and bolometer readouts are asynchronous, all systems embed in their data streams a common timestamp using EBEX "ticks" which is recorded for post-flight alignment. The systems maintain a relative synchronization

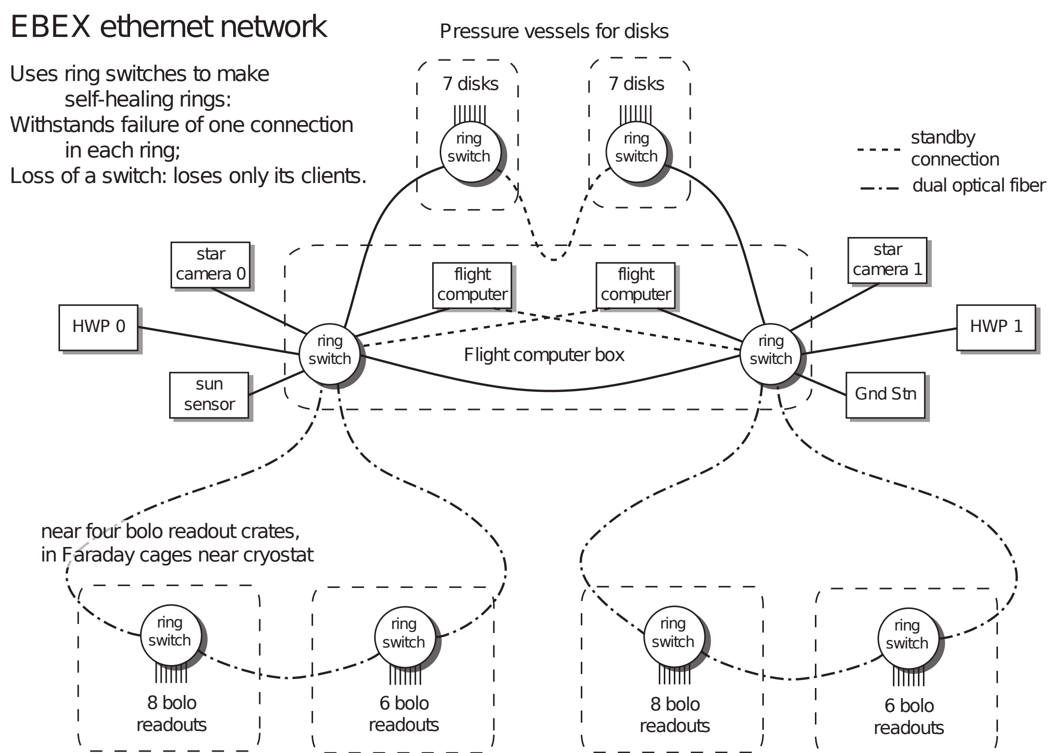

Figure 5.1: Configuration of the EBEX gondola ethernet network planned for the long duration Antarctic flight. For the North American test flight, we flew only one disk pressure vessel containing only two hard drives, only one star camera, and a total of 12 DfMux boards in two Bolometer ReadOut crates.

of ~ 10 μs by resynchronizing to an onboard precision clock every 164 ms. The time servers broadcast synchronization messages onto the CANbus, and distribute timing data to the DfMux boards and ACS via an RS-485 serial link that does not connect to the flight computers. The housekeeping and timing subsystems are described in Sagiv et al[25].

5.3 Flight control program – *fcp*

The flight computer crate contains two Ampro single board computers[50], each configured with a 1.0 GHz Celeron processor, 256 MiB RAM, and a 1 GB solid state flash disk module. The module stores the computer operating system, currently Debian GNU/Linux 4.0[51] with Linux kernel 2.6.18 and additional modular drivers for the ACS E-bus and USB-CANbus adapter. The flight control program *fcp* resides on the flash module as well, which the operating system is configured to run immediately after the computer boots.

fcp is a derivative of the BLAST experiment's *mcp*[14], and preserves its overall architecture as a monolithic program running multiple concurrent, event-driven threads, with a main loop handling pointing, frame generation, and data logging clocked to the E-bus. We have added code modules implementing control and readout of the DfMux boards, housekeeping via the CANbus, storage to the networked disk storage array, and the downlink scheme discussed below. Other modules have been modified as needed. For the LDB flight we plan to replace the command scheduling and TDRSS satellite downlink modules.

Flight computer redundancy is implemented via a watchdog card connected to the IEEE 1284 parallel port of each computer. In nominal operation the *fcp* `WatchDog` thread toggles a pin on the parallel port at 25 Hz. If this action ceases for more than a configurable length of time, a fault is inferred. The watchdog card will power cycle the faulty computer and switch control to the other computer. Besides crashes in the software or hardware of the flight computer, *fcp* can programmatically trigger this sequence of events by terminating the `WatchDog` thread in response to certain error conditions. The identity of the computer in control is communicated to both flight computers via the E-bus, and recorded as the `incharge` variable. During the North

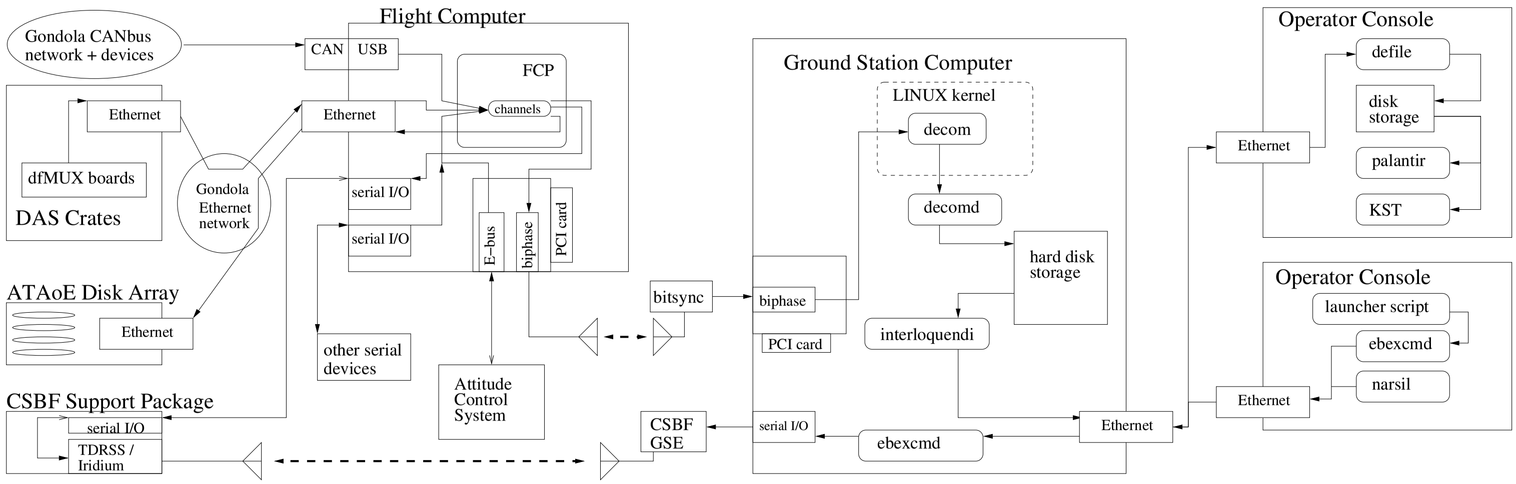

Figure 5.2: Schematic diagram of command and data flows in the EBEX flight and ground systems. Square corner boxes represent physical components, and rounded boxes generally represent software modules. The left side of the figure comprises flight systems, including the flight computer running *fcp* (Sec. 5.3) connected to DfMux boards in the Data Acquisition System (Sec. 5.4) and the disk storage system (Sec. 5.5). The center of the figure represents the ground station, containing the interface to CSBF downlink equipment (*biphase*, *decom*, *decomd*, Sec. 5.6), and the server portion of the data distribution software chain (*interloquendi*). Sample operator console configurations (Sec. 5.7) are shown on the right. A data monitoring terminal at top illustrates the client (*defile*) and display (*KST*, *palantir*) portions of the data distribution chain. Below, a commanding station illustrates the command uplink chain via *narsil* and *ebexcmd*. The heavy dashed lines represent radio communications between the gondola on the left and ground on the right. In the interest of space and clarity data paths for satellite downlinks are omitted.

American engineering flight dataset the value of this variable changes only once, at 8:19 UTC, due to an intentional pre-flight reboot of the then-active flight computer. This indicates that there were no such reboots of the in-charge flight computer between launch at 14:01 UTC and termination after 03:18 UTC.

As indicated in Table 5.1, however, the non-in-charge flight computer did reboot several times in the course of the test flight. The rapidity of the reboots near 17:30 UTC, and thermal and current data suggesting that the non-in-charge computer rebooted additional times without running long enough to write log entries to disk[17], point to a malfunction of the watchdog card or power supply. All parts of the flight computer crate are being overhauled in preparation for the long duration flight.

Time (UTC)	Which computer	Event
2009-06-11 7:54:26	in-charge	Logfile begins
8:21:42	other	Logfile begins
14:01:48		Launch
17:27:15	other	Logfile restarts
17:30:38	other	Logfile restarts
17:36:48	other	Logfile restarts
2009-06-12 3:29:15	in-charge	End of log
3:33	other	End of log

Table 5.1: Restart times for the flight computers, based on the log entries that *fcp* writes on startup. It is possible that the non-in-charge flight computer rebooted more than three times near 17:30 UTC, but did not run long enough to write log entries to disk.

5.4 Distributed networked bolometer readout architecture

Each DfMux readout board combines analog signal processing hardware with an FPGA implementing digital signal processing modules and a soft CPU running an embedded Linux distribution. The DfMux hardware is described in detail by Dobbs et al[24]. Operations comprising the setup, tuning, and maintenance of the detectors and readout system are controlled by the flight computer via requests over the Ethernet network, and readout data are returned over the same network.

Low level operations are exposed via small programs in the DfMux firmware implementing the Common Gateway Interface[52]. More complex algorithms are invoked as jobs through an interface called "Algorithm Manager," which passes data using JavaScript Object Notation (JSON)[53]. On each DfMux board a program, implemented by code in a subset of the Python language[54], listens on a network port for requests to start, stop, or collect the output of jobs. Because of memory and CPU constraints in the embedded environment, no more than two jobs may run at a time on each board. In *fcp* the `algMan` module maintains queues of pending and running jobs and attempts to run all requested jobs as soon as possible, while ensuring that on a per-board basis all jobs are run in the order requested. To the rest of *fcp*, `algMan` exposes routines to trigger algorithm requests to a single board. It also provides a higher level interface based on stored parameter files. In these files sets of algorithm parameters are defined on a per-SQUID basis. After commanding *fcp* to parse one of the stored files, `algMan` will respond to these high-level commands by dispatching algorithm requests for the corresponding operation for each SQUID defined in the parameter file.

Regardless of the method of invocation, requested operations will produce output strings in the JavaScript Object Notation format which are returned to `algMan`. These strings, generically termed "algorithm results," are logged to disk and added to the file downlink system queue.

DfMux boards output data samples by broadcasting User Datagram Protocol[55] packets to a multicast address over the Ethernet network. Each packet is 1428 bytes and consists of a header and 13 frame structures. In the case of the bolometer readout boards in the configuration flown in the 2009 engineering flight, with 8 bolometer per SQUID multiplexing (32 total bolometer channels per board) these frames contain a timestamp and one 16-bit sample for each of the 32 channels recorded at the corresponding time. For a 190.73 Hz sample rate each board broadcasts packets at 14.67 Hz. Within each bolometer readout crate, the DfMux boards are synchronized to a common 25 MHz oscillator so that the bolometers for all boards in the crate are sampled at the same time.

In *fcp* the `UDPS_Listener` packet reader thread listens on the multicast address. Each packet is inspected to determine its origin, and the `pdump` module writes it to disk in a packet dump (`.pdump`) file corresponding to the originating board. The `.pdump` files are

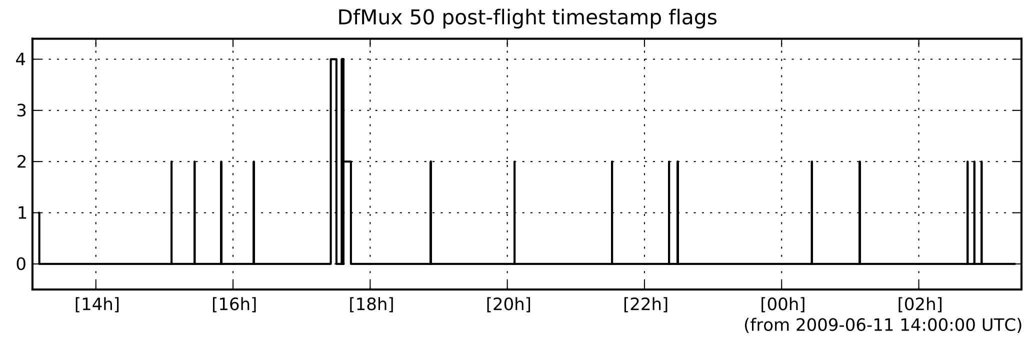

Figure 5.3: Synchronization flags for a typical bolometer readout board during the 2009 flight. The flag values indicate: 0 – sample present and synchronized; 1 – padding at ends; 2 – missing data; 4 – wrong sample rate. The anomalous behavior around 17:35 UTC corresponds to a commanded reboot of the DfMux boards. Most of the isolated spikes to state 2 indicate single packets missing from the recorded data stream, 20 in total for this board. Otherwise for this board data samples were logged for the entire flight, and those samples were synchronized to the common oscillator.

rotated every 15 minutes to limit the maximum file size produced. Fig. 5.3 demonstrates the performance of this readout system for a typical readout board. Excluding a brief period around 17:35 UTC when the boards were commanded to reboot during a SQUID tuning procedure, no board is missing more than 65 packets from the logged packet data, for a loss rate of $< 0.01\%$. Testing on the ground shows that under simulated load equivalent to the full planned complement of 28 boards, loss rates remain similarly low. 11 of the 12 bolometer readout boards were synchronized to the common oscillators in their respective crates for the entire flight. The twelfth board was left unsynchronized due to a misconfigured startup script.

Two DfMux boards are also used to read the optical angular encoder on the HWP. They each sample a single channel at 3.052 KHz. Each HWP encoder packet contains 416 samples, and thus each board broadcasts packets at 7.34 Hz. The structure of the bolometer readout packets is reused for the HWP encoder readout, so the same code processes both types of packet stream.

The code defining the packet format is written in portable C that is compiled into the packet streamer program onboard the DfMux CPU, `UDPS_Listener`, and the standalone `parser` program used to extract data from packet streams and saved dumps.

5.5 ATAoE onboard storage

EBEX will fly with over 3 terabytes of hard disk storage. This allows the flight computers to write two redundant copies of all data produced in flight to separate disks. We use the ATA over Ethernet (ATAoE) protocol[56] in order to implement the onboard disk storage array. Ethernet has several attractive features. It provides a many-to-many topology so that redundant disks can be provided without foreknowledge of which flight computer will need one. It is physically straightforward to route signals from the flight computer crate in vacuum into the pressure vessels holding hard disks. Finally, Ethernet is already in use onboard so it avoids adding an additional networking technology. Drivers for the ATAoE protocol are a standard part of the Linux kernel.

As shown in Fig. 5.1, the disk drives are divided between two pressure vessels. Each vessel contains a ring switch, a passive backplane for power and signal distribution, and up to seven 2.5” laptop disk drives mounted on ATAoE blades[57]. Each blade is connected independently to the ethernet ring switch. In *fcp* the `EBEX_AOE` module abstracts detection, setup and low-level management of the array. Disk usage is flagged in non-volatile memory present on each blade to ensure that the two flight computers do not attempt to simultaneously mount the same disk. This module will only present as available disks which are not already in use and which have sufficient free space remaining. The `aoeMan` module adds an additional layer of abstraction, allowing *fcp* code to request file operations without any detailed knowledge of the disk array. It mounts disks as needed to supply the requested free space, and translates filenames to correspond with the correct mount points in the filesystem namespace.

5.6 Downlink and data logging

fcp produces a 1 Mbit/s biphase encoded output data stream, suitable for transmission over the CSBF-provided line-of-sight downlink. This stream combines all output channels of the ACS and housekeeping systems, packet data streams from five selectable DfMux boards, and a file downlink system called `filepig`, used to retrieve algorithm results, diagnostic logs, and other irregularly formatted data. At the launch site the EBEX ground station uses a commercial bit synchronizer, custom decommutator card, and the *decomd* software to decode and store this data stream to disk.

As detailed in Fig. 5.4, the downlink stream is composed of 1248 byte frames generated at 100 Hz. These are grouped into superframes of 20 frames. Each frame begins with a sync word and counters, followed by channel data. Each 2-byte word of channel data can either contain samples of a "fast channel" at 100 Hz, or have 20 "slow channels" multiplexed over the superframe at 5 Hz. In the 2009 engineering flight, this channel data totalled 194 bytes per frame, encoding 59 fast channels and 480 slow channels. This channel data is also logged to disk onboard the gondola.

The remaining space in each frame (1048 bytes, after overhead, for the 2009 flight configuration) is aggregated across the superframe and used to transfer DfMux readout packets and `filepig` data blocks. In *fcp* this format is defined by the "Biphase marshaler" module, which accepts data from `UDPS_Listener` and `filepig` via message queues and assembles the superframe data area. Every 200 ms the *fcp* downlink code queries the marshaler for an assembled data area to incorporate into the transmitted frames.

The marshaler uses fixed slots in the superframe to provision a deterministic bandwidth to each downlinked data stream, and to ensure that if one frame is lost or corrupted, data in the surrounding frames can still be correctly reassembled. `UDPS_Listener`, described above, passes whole packets, and thus requires 1428-byte slots. In 200 ms a bolometer readout board produces on average 2.93 packets, and a HWP encoder board produces 1.47. Thus a group of three slots for bolometer readout or two slots for encoder readout yields a stream with adequate capacity to downlink the entire packet data output of a DfMux board. With 14 slots, streams are defined to downlink the output of four bolometer readout boards and one HWP encoder board. Uplinked commands select which five boards out of the total complement are allotted a downlink stream.

Because the marshaler slots are agnostic to their content, we will be able to implement downlink compression for the bolometer packet data for the LDB without significant code changes to either the `UDPS_Listener` or biphase marshaler subsystems. Instead, we plan to develop a compression module that will receive packets from the `UDPS_Listener` message queue in place of the marshaler. This module will compress packets until a fixed-size block is full, at which point it will forward the block to a message queue connected to the marshaler. The only needed change to the marshaler will be to alter the slot size and expected data type so that the compressed blocks can

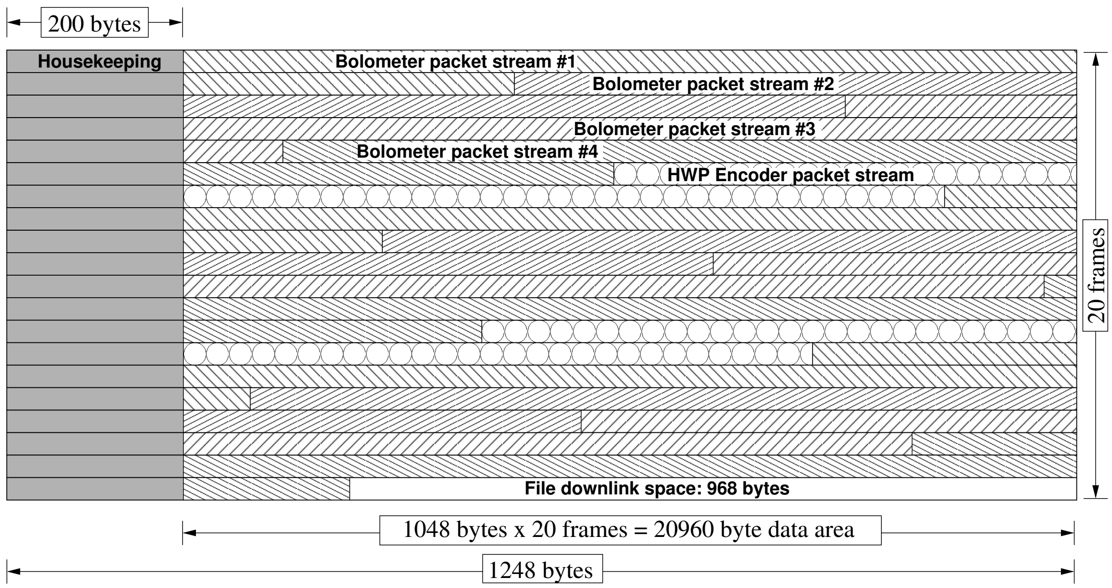

Figure 5.4: Schematic of the line-of-sight downlink superframe discussed in Sec. 5.6. This structure is repeated at 5 Hz over the 1 Mbit/s transmitter. The horizontal rows indicate the 20 individual 1248 byte frames, transmitted at 100 Hz. Each frame starts with 200 bytes of header and housekeeping channel data. The remaining 1048 bytes in each frame is aggregated across the superframe to form a 20960 byte data area. 14 slots of 1428 bytes each are allotted for DfMux packets and are grouped into five logical streams (denoted here by matching hatch patterns), accomodating the complete data output of four bolometer readout boards and one HWP encoder readout board. The final 968 bytes of the superframe is used by the `filepig` file downlink system.

be correctly routed and decoded on the ground.

`filepig`, so named because it allows files to "piggyback" on a frame-based protocol, claims the odd-sized chunk of space at the end of the data area after packet streams have been allocated. It exposes an interface by which *fcp* code may queue the filenames of data objects already written to disk. Files are broken into chunks together with minimal header and error detection data and downlinked. Support exists, presently unused, to plug in transformations for more robust error correction or data compression, and to resend corrupted data in response to uplinked commands. For the engineering flight 968 bytes per superframe were left for the `filepig` data chunk, providing about 4.2 KB/s file downlink bandwidth. Over the 13 hour flight 10898 files totalling 61 MB were retrieved.

5.7 Ground tools and architecture

Once downlinked, flight data is distributed to workstations and made available for real time processing and visualization. The EBEX real-time analysis architecture is focused on streaming both primary data and derived data products to provide immediate feedback on the state of the instrument, leveraging local networks to enable as many researchers as possible to interact with the incoming data, and a modular architecture based around interchange of standardized data formats between components potentially running different widely-separated machines.

5.7.1 BLAST-derived telemetry chain

The BLAST telemetry chain[14] is employed largely unmodified on the ground. As illustrated in Fig. 5.2, the biphase encoded bitstream is converted back into data frames in the Ground Station computer and logged to disk. The *interloquendi* server permits clients to fetch streams of frames remotely via TCP/IP connections. *defile* then decodes the channel data in these frames into dirfile[58] formatted data files. Front end programs such as *palantir* and *KST*[59] allow real-time display of the streamed channels.

To this EBEX adds support in the frame handling code for the superframe data area, and support in *defile* for extracting packet streams and downlinked files from those frames. These additional data products are written alongside the channel-based data on each connecting client workstation. Scripts employing the *parser* program automate the production of bolometer and HWP encoder time streams in dirfile format from extracted `.pdump` files.

Time streams can be displayed in real-time using either *KST* or Python tools that understand the dirfile format. We developed a set of Python bindings to the *getdata* dirfile library as the module `pygetdata`; the GetData project has since developed a similar Python binding under the same name.

5.7.2 Alignment and interpolation tools

The EBEX Alignment Tools is a suite of programs for further processing these streams, including interpolation and alignment to a common sample rate and timing, decoding the HWP angular encoder signal to HWP position, and template-based removal of the

HWP rotation signal from bolometer timestreams. The *interpX* family of programs take as input dirfiles of bolometer, ACS, or hwp angular encoder data and apply linear interpolation with corrections for periodic signals (so that extra values are not added when e.g. an angle wraps around from 359.9° to 0°) to resample all channels of interest to be synchronous with the bolometer samples. Variants of this program exist to process logged data in bulk or to process streaming data in real time. This suite also includes the core HWP template fitting routines, which are discussed in detail in Sec. 6.2.

Fig. 5.3 is a diagnostic product of the bolometer alignment class `TimeFlagger`, which exploits the sampling synchronization between DfMux boards to merge many boards worth of bolometer dirfiles into a single dirfile with a common timestamp field. To do so, the tool identifies those DfMux boards that logged bitwise identical timestamps (typically not at the same sample index), and applies to every channel any offset needed to ensure that identical timestamps occur at the same sample index for each board. This process is iterated forward to fill gaps due to dropped packets, with missing timestamps taken from other boards, and missing bolometer values filled with a sentinel value and flagged in a status channel. It is this flags channel that is plotted for board 50 during the North American flight in Fig. 5.3. Only in the case that all boards are missing a range of timestamps, as happens during a brief period when the DfMux data streamer programs were commanded to halt, is interpolation used to obtain the correct number of missing timestamps.

5.7.3 Visualization tools

To visualize timestreams in parallel as they correspond to detectors, we have developed *jsviz*. This tool consists of an HTML and Javascript frontend designed to run in a web browser, and a set of JSON formats for describing a focal plane layout and communicating an arbitrary set of properties attached to each bolometer. The browser-based component downloads a geometry specification from its server, and uses the HTML5 CANVAS element[60] to draw a continuously updated schematic of one or both focal planes populated with wafers according to that specification. The geometry file also contains a pointer to one or more data files available for download that describe properties of each bolometer. On the server, these data files may be created once, if describing properties (such as connection information) that do not change, or may change several

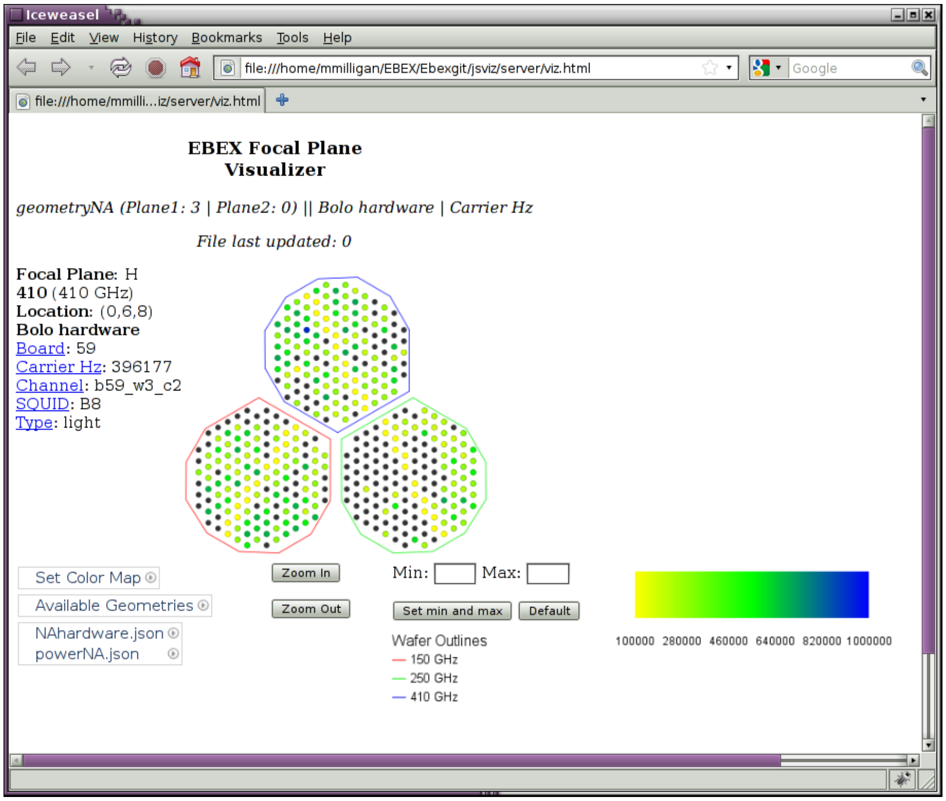

Figure 5.5: Screenshot of *jsviz* running in a web browser. The geometry displayed is the three wafers flown in the test flight–the layout reproduces the layout and relative orientations of the wafers as seen from the sky if the focal plane was uncovered. The color code in this display is representing the bolometer bias carrier frequency.

times per second if describing properties (such as noise level) that are derived from a stream of bolometer data. In the browser, these values can be listed, or used to color code the bolometer symbols in the visualization. A screenshot of *jsviz* running in a browser is displayed in Fig. 5.5. Using a web browser as the tool for this platform has provided three distinct advantages: deployment of the tool to a new computer is as easy as navigating to a URL; platform independence is achieved automatically; and potentially demanding processing operations to extract meaningful parameters from many bolometer data streams in parallel need only be done on one central server computer. Even relatively old computers, if equipped with a reasonably recent browser, have been shown to run the visualization without trouble at update rates of up to 10 Hz.

We have also written a Python/TK front end to the Algorithm Manager system. By monitoring the names of the files downlinked through `filepig`, it is possible to select those corresponding to algorithm result strings. Parsing these files permits display on a board-by-board basis, in close to real time, of the job execution activity occurring in the readout system DfMux boards. A dashboard interface presents selected information from each board using labels and color coding, and the user can select individual boards or jobs for more detailed display. This front end provides immediate visual feedback on complex operations, such as detector system tuning, that entail parallel execution of a sequence of jobs on each bolometer readout board.

5.7.4 Networked operations

ebexcmd accepts *fcp* commands in textual format, which it can either relay to a listening *ebexcmd* over a network connection, or convert to the binary representation suitable for transmission over CSBF uplink hardware. Commands can therefore be generated on any host permitted to connect to the ground station, and those commands will then be uplinked. Commands are most commonly selected through the *narsil* front end, but are also generated by Python scripts and may even be entered manually from a command line.

This ground infrastructure provides network transparency in both data distribution and commanding, allowing flight operators to monitor and control the instrument from an arbitrary number of networked workstations. During the 2009 integration campaign and flight, this system routinely connected as many as ten client workstations over the private internal network at the New Mexico launch site. Late in the flight line-of-sight communications were only possible from the downrange station in Arizona, and commands were successfully relayed from the launch site through the downrange ground station *ebexcmd*. Streaming of frame data via *interloquendi* from the downrange station to the launch site, and from the launch site to collaborators at their home institutions, worked only intermittently due to bandwidth constraints at the launch site. We are investigating techniques to stream subsets of the full downlink data stream, and/or apply data compression, to address this issue for future campaigns.

5.8 Summary

EBEX combines a large format bolometer array, and the correspondingly large data volume, with a complex readout system architecture. As a result, EBEX solves for a balloon flight environment problems in data handling, communications, and control that are typically associated with ground based observatories. The required 3 terabyte in-flight storage capacity is achieved using a high speed gondola ethernet network and networked disk storage arrays. The readout system is controlled from a central flight computer using a custom distributed job control scheduler, and it is monitored by extending a frame-oriented telemetry system to support asynchronous packet streams and event-driven downlink of arbitrary data in files. On the ground, a networked real-time data distribution and command relay architecture allows shared monitoring and control of the instrument.

Chapter 6

North American Dipole Scan Analysis

When the disks storage arrays are recovered after a flight of the EBEX instrument, most science data is packed into framefiles and packet dump files. After these are appropriately parsed and concatenated, the result should be:

- one dirfile sampled at 100.16 Hz containing the channels that traverse the E-bus
- one dirfile per DfMux board sampled at 190.73 Hz containing bolometer and timestamp timestreams
- one dirfile per HWP encoder board sampled at 3052 Hz containing the filtered output of the optical angular encoders
- logging and diagnostic information in a variety of formats

To begin processing, the E-bus, bolometer, and HWP encoder data are merged–aligned and resampled to a common sample rate–using the tools described in Sec. 5.7. The HWP orientation angle is reconstructed from the encoder data using a procedure not documented here[61].

Following the convention used by B. Johnson[23], the raw data stream for each bolometer is

$$d_i = s_i + n_i + h_i + g_i \tag{6.1}$$

where i is the sample index, d the sampled bolometer data, s the optical signal from the sky, n the Gaussian random noise, h the HWP synchronous signal (also called the HWP template), and g other spurious signals produced within the EBEX instrument. Sec. 6.2 will thus elaborate a technique to robustly estimate the h_i and subtract them from the recorded timestream. g is composed of transients, which can be identified and removed in time domain, and of periodic components, which are characterized and removed by frequency domain processing described in Secs. 6.3. Ultimately we use these techniques to recover

$$s_i + n_i = d_i - \langle h_i \rangle - \langle g_i \rangle \tag{6.2}$$

where $\langle h_i \rangle$ and $\langle g_i \rangle$ are statistical estimates (maximum likelihood expectation values, if available) of h_i and g_i, and attempt to correlate s_i with astronomical simulations.

The remainder of this chapter will describe the application of the techniques developed to analysis of data from the dipole scan portion of the North American EBEX test flight, as outlined in the following section.

6.1 NA Flight Dipole Scan

As noted in Chapter 3, the dipole scan took place near the end of the North American test flight. At 2:53:15 UTC June 12, the pivot PWM drive was manually set to drive the gondola into constant rotation. The initially commanded value proved to drive the gondola faster than expected, and after 90 seconds the gondola rotation had reached a maximum of 50°/s, and the PWM value was reduced to allow the gondola to slow down. The gondola took approximately two minutes to halt, and at 2:59:54 the PWM value was increased again. With continuous manual adjustment the gondola reached and was maintained at an average rotation speed of 16.7°/s for 13 minutes and 40 rotations. The azimuth motions of the gondola during the dipole scan are plotted in Fig. 6.1.

6.1.1 Reconstructed Pointing

The azimuth pointing plotted, and used throughout this chapter, is the result of the post-flight pointing reconstruction procedure[17, 28]. However, that reconstruction is thought to be less reliable for the dipole scan than for other portions of the flight. The reconstructed pointing model was shown to exhibit an unexplained correlation between

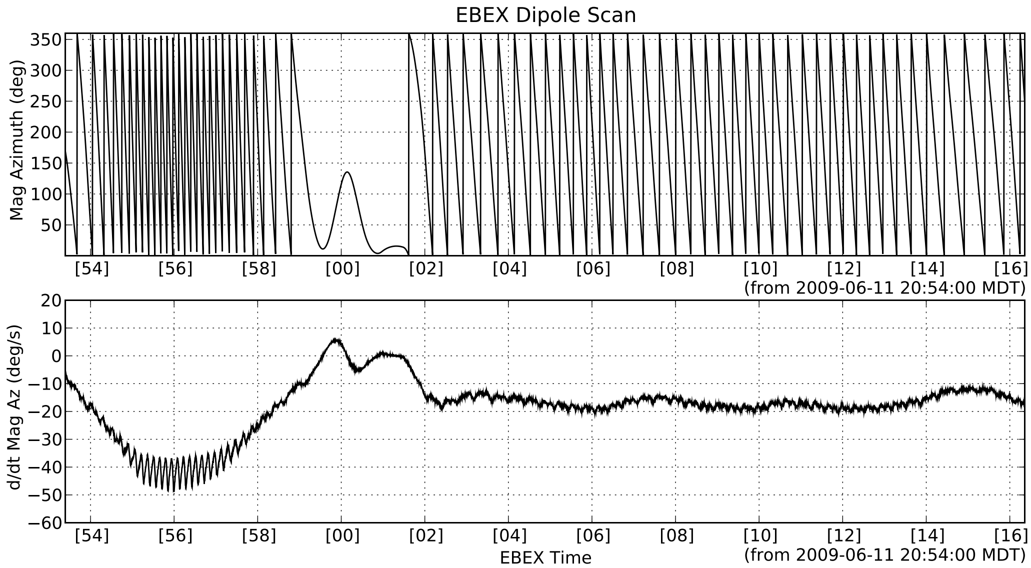

Figure 6.1: Above: telescope boresight azimuth during the NA flight dipole scan. Below: angular velocity of the telescope boresight pointing during the dipole scan. In both plots the azimuthal pointing has been reconstructed post-flight based primarily upon logged magnetometer data.

rotational speed, as measured by the gyroscopes, and the inferred azimuth pointing of the gondola. Because the dipole scan features the highest rotational speeds of the flight the effect on pointing reconstruction is unknown.

The exact elevation pointing is also unknown. After the elevation actuator failed during launch, the inner frame became permanently pointed at a constant elevation relative to the outer frame, 17.2° according to the trunion bearing elevation encoder. Under static conditions, due to the imbalance of the gondola the true sky pointing would be roughly 2° lower than this, and thus for most of the flight the boresight is believed to be pointed at a constant $\sim 15°$ elevation from horizontal. However, under conditions of rapid rotation, the unbalanced payload may appreciably precess or nutate. The inner and outer frame clinometers, which suffered from common mode noise and long term drifts[17], nevertheless report an excursion of up to one degree at the start of the dipole scan, and fluctuations of about 20-30 arcminutes throughout the scan period (Fig. 6.2).

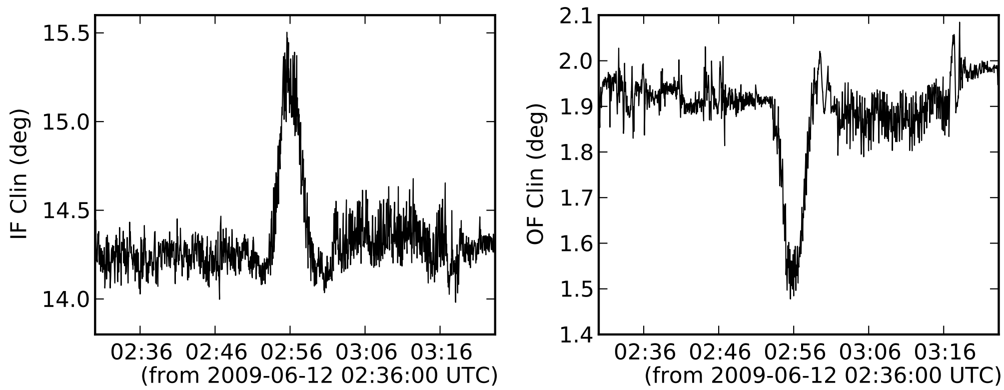

Figure 6.2: Readings from the inner frame (IF, left) and outer frame (OF, right) clinometers from 2:30 UTC to termination. The large excursion at 2:53 UTC corresponds to the period of rapid rotation at the start of dipole scan, and the remainder of the dipole scan with lower rotation speed lasts until 3:16 UTC.

6.1.2 Microwave Sky Flux Model

In order to place the estimated dipole scan pointings into an astronomical context, we construct a model of the anticipated microwave flux in the EBEX observing bands. Such a model has two components of interest: the CMB itself, and emission from galactic dust. As the dipole scan subtends the entire sky, we prepare an all-sky model using the Hierarchical Equal Area isoLatitude Pixelization (HEALPix)[62] representation, primarily via the `healpy` module[63] which provides HEALPix functionality in Python[54].

As we shall see, the aggregate sensitivity of the dipole scan falls far short of that needed to measure the primary anisotropies of the CMB, which are on the order of 35 μK[64]. Therefore we model the CMB as composed of only a 2.73 K monopole[65] and a 3.36 mK dipole in the direction $\ell = 264^\circ.3$, $b = 48^\circ.05$[66, 67]. These components are combined to give a per-pixel temperature, which is converted to flux (MJy/sr) in each band using an implementation of the Planck function written in Python.

We model emission from galactic dust after Model 8 of Schlegel, Finkbeiner, and Davis[68, 69]. The SFD map combines all-sky data from FIRAS, IRAS, and DIRBE to produce cleaned maps of 100 μm emission and a flux ratio parameter. They then provide a series of models, culminating in Model 8 which combines two dust emission components with different spectral indices ($\alpha_1 = 1.67$, $\alpha_2 = 2.70$) with a fitted dust temperature. The result is an empirical expression that can be used to compute the flux for each band at each pixel. Schlegel et al. provide a C code implementing these models, which we have reimplemented in Python and integrated with `healpy`.

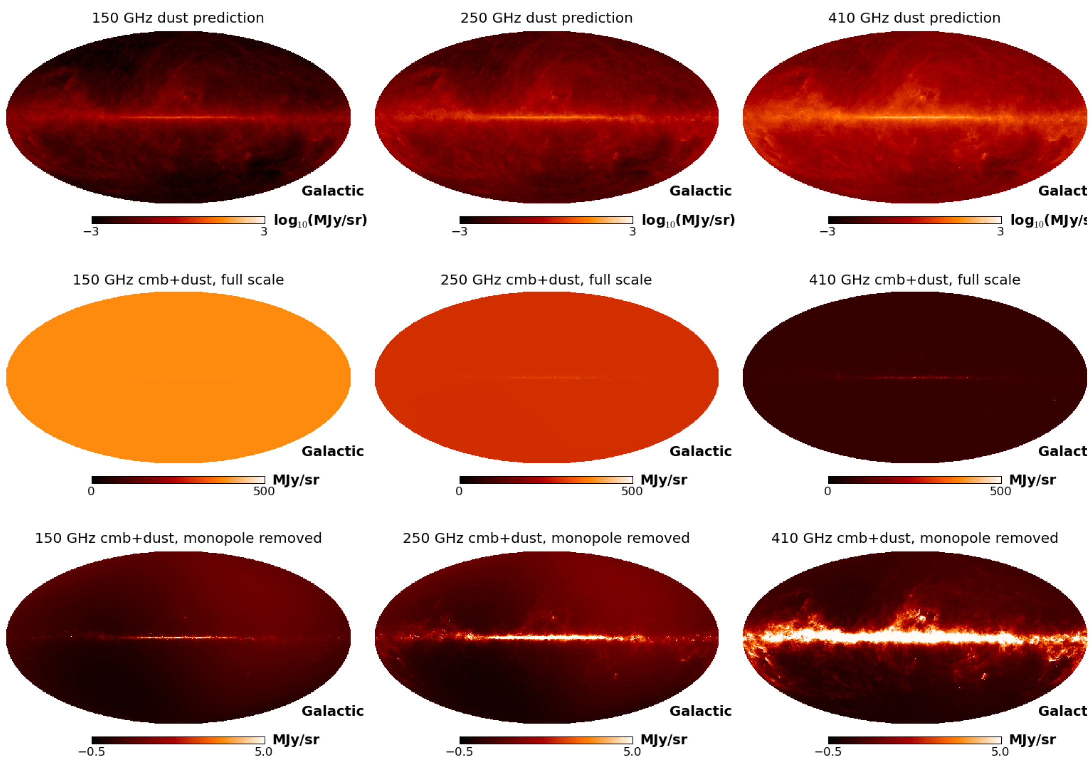

Figure 6.3: Outputs of the microwave sky flux model, at 150 (left column), 250 (center), and 410 (right) GHz. Each panel shows the Mollweide projection of a full sky map in HEALpix format[62], along with a color bar for scale. In the top row is the output of Model 8 from Finkbeiner et al.[69] alone, plotted using a logarithmic color stretch. In the middle row the predicted dust flux is added to the CMB model (2.73 K monopole[65] and 3.36 mK dipole[67, 66] terms), and the bottom row displays the same after the monopole term is removed. The lower two rows use a color scale that is linear in flux.

Finally, for each band center (150, 250, and 410 GHz), we compute flux maps for the CMB and for the SFD dust model and store the sum. The resulting maps are shown in Fig. 6.3, which illustrates that the galaxy becomes brighter relative to the CMB with increasing frequency, but that flux from the CMB monopole dominates all but the brightest portions of the galactic plane at all three bands. However, diffuse dust emission away from the galactic plane is significant when compared to the dipole alone.

6.1.3 Astronomical Context

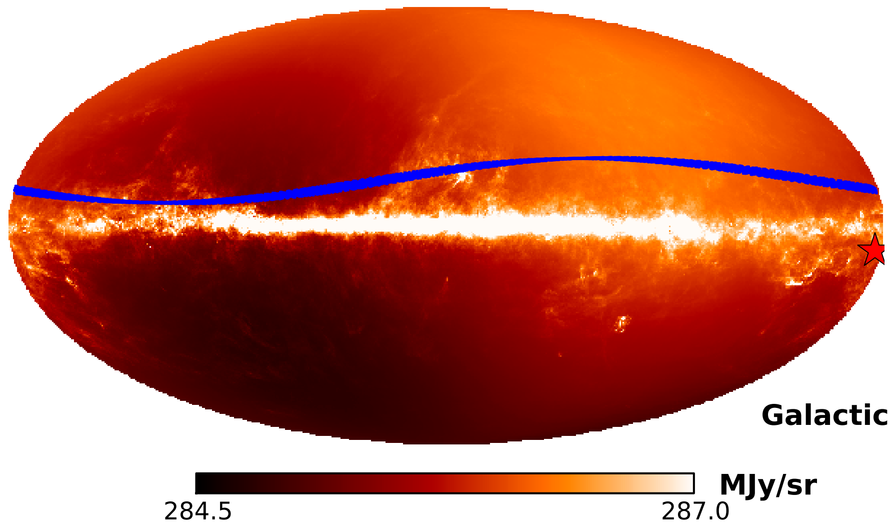

Figure 6.4: Full sky map of the 250 GHz microwave sky flux model described in Sec. 6.1.2 overlaid by the boresight track of the NA flight constant elevation dipole scan after stable gondola rotation was achieved. The map is oriented according to Galactic coordinates. The color scale leaves the brightest portion of the galactic plane saturated: the maximum flux density is 457.4 MJy/sr. The large red star marks the position of the Sun on this date.

The best estimate boresight pointing during the dipole scan rotations is overplotted on a full sky 250 GHz intensity prediction in Fig. 6.4. At the time of the scan, the North Galactic Pole was located about 6° from the local zenith. With the scan elevation low and approximately constant, the scan covers a narrow stripe that is nearly a great circle on the sky, which is broadened by the rotation of the sky over the course of 23 minutes. As a result, the area covered roughly parallels and never crosses the Galactic plane.

The position of the Sun is noted in Fig. 6.4 with a red star. During the dipole scan the Sun ranged from $-1.9°$ to $-5.7°$ elevation. While below horizontal, as noted in Chapter 3 the geometric horizon was located at $-6°$ elevation and the sun should therefore have been visible to the northwest (at $\sim 300°$ azimuth).

We have not attempted to calculate the degree of extinction or atmospheric refraction that sunlight would experience in this configuration, but well after local sunset on the ground, eyewitnesses–including this author–were able to see the balloon brightly

Figure 6.5: This photograph of the EBEX balloon was taken from near Phoenix, AZ at or close to 3:04:48 UTC according to the EXIF metadata embedded in the image, which the photographer believes to be correct. He also reported that the balloon visually entered darkness "shortly after." (Photograph courtesy John Kittelsrud.)

illuminated by sunlight at float altitude. Shown in Fig. 6.5, John Kittelsrud was able to photograph the balloon in sunlight at about 3:05 UTC, about halfway through the dipole scan. While many of the pixels are saturated, the unsaturated pixels of the gondola do not evidence obvious reddening. He reports that the balloon disappeared from view "shortly after," consistent with the fact that the sun would have passed below $-6°$ elevation at 3:15:30 UTC.

While we expect that the scoop baffle should have prevented sunlight from directly entering the inner frame black cavity, the possibility exists for radiation to indirectly enter the optical path due to scattering from the lip of the scoop. In addition, exposure to sunlight could produce scan-synchronous temperature changes in baffle structures that potentially radiate into the optical path.

In addition to using the CMB dipole as a calibration signal, we are interested in observing emission from galactic dust. Due to the low galactic latitude of the scan track, the instrument pointing passes through several regions of enhanced dust contrast. Of particular interest is the region near Ophiuchus, in the direction of 0° galactic longitude. There the pointing track crosses several regions of high stellar extinction associated with the Ophiuchus and Lupus molecular cloud complexes[70].

Of particular interest, as illustrated in Fig. 6.6, the pointing passes close to the well studied ρ Ophiuchi molecular cloud and star forming region, which at ~ 130 pc is one of

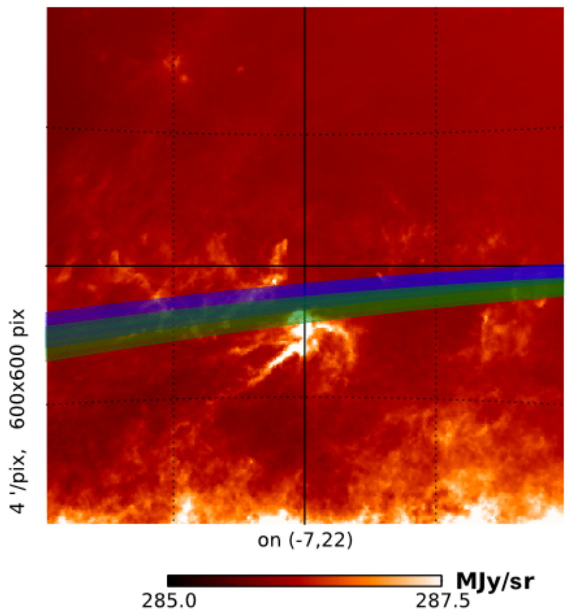

Figure 6.6: Map of the 250 GHz flux model in the vicinity of the ρ Ophiuchi cloud complex, centered at Galactic coordinates $l = -7°$, $b = 22°$. For scale, the graticule lines are spaced at 10° apart. The map is overlaid by two possible instrument pointings: blue covers the area scanned by a detector pointed at 15.5° elevation above horizontal during the dipole scan after 3:02:20 UTC, and green shows the same for a detector pointed at 14.5° elevation.

the nearest significant star forming regions to the Sun[71]. This cloud contains several compact cold dusty cores which emit strongly at millimeter wavelengths, with observed surface brightnesses up to 280 MJy/sr at 1.3 mm[72] and in excess of 1000 MJy/sr at 850 μm[73] on scales of a few arcseconds.

Unfortunately, all but the very lowest-elevation detectors, and possibly all detectors depending on the true instrument pointing elevation, miss the very brightest central region of ρ Ophiuchi. The peripheral regions of the complex are not as well studied at millimeter wavelengths, but wide-field imaging exists out to about a degree from the core[72, 74]. Moreover, due to the resolution limitations of DIRBE and FIRAS, the SFD model does not fully resolve the temperature structure of compact structures on

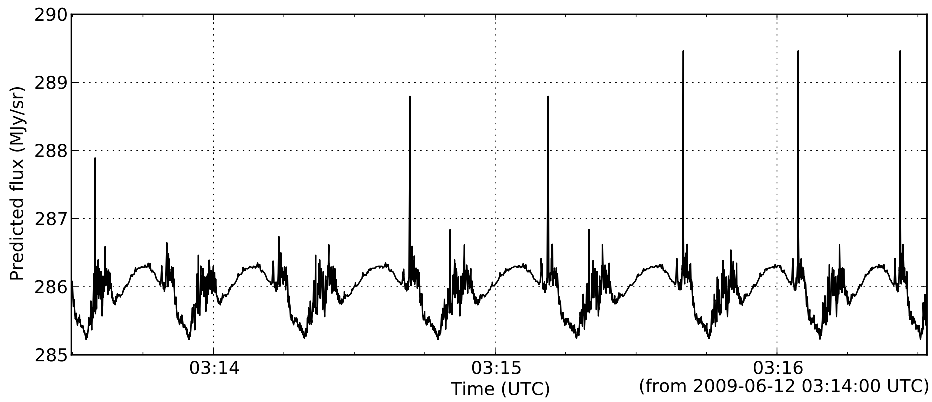

Figure 6.7: 250 GHz flux model timestream for three minutes at the end of the dipole scan, for a detector pointed at 15° elevation. This is an excerpt from the flux timestream generated by indexing HEALPix pixels in the 250 GHz model sky against pixel indices computed from the recorded instrument pointings. The DC level is set by the CMB monopole, and the periodic sinusoidal component is the CMB dipole. The peaks above 288 MJy/sr correspond to close approaches to the core of ρ Ophiuchi.

sub-degree scales. As a result, the flux model map is likely to provide a better flux estimate in the periphery than in the dense core region of ρ Ophiuchi[68].

6.1.4 Flux Timestream

`healpy` provides functions to convert pointings in equatorial or galactic coordinates into pixel indices in a HEALPix map. Because the geographic position and local sidereal time at the gondola are continuously recorded in the ACS frame, we can easily convert azimuth and elevation pointing timestreams into RA and declination pointings using the standard algorithm[75], and then compute the sequence of indices of HEALPix pixels visited as a function of time.

The typical scale of a HEALPix pixel is $\sqrt{3/\pi}3600/N_{side}$ arcminute. For this work we will use the NSIDE$=512$ map, which gives a typical pixel scale of $6.9'$, comparable to the nominal size of the EBEX beam and, at $\sim 16°$/s rotation speed, also comparable to $\sim 5'$ per 190.73 Hz bolometer sample. As we are primarily interested in much larger features than this, and because we have no authoritative beam map to use as a reference, we do not attempt at this stage to convolve the sky map with a hypothetical EBEX beam.

Sec. 5.7 described the EBEX Alignment Tools, through which an instrument pointing is obtained for each bolometer sample. For each element in this pointing timestream, a pixel index is computed, and HEALPix map is consulted to obtain the flux for that pixel. The result is a model flux timestream, an excerpt of which is plotted in Fig. 6.7. Note that the DC level and sinusoidal component correspond to the CMB monopole and dipole, respectively; deviations from this are due to flux from dust emission. The largest spikes in the flux timestream correspond to passages through the bright emission regions near ρ Ophiuchi. The amplitude of those spikes can vary considerably from one rotation to the next as sky rotation brings the scanning elevation of the instrument past various small-scale features.

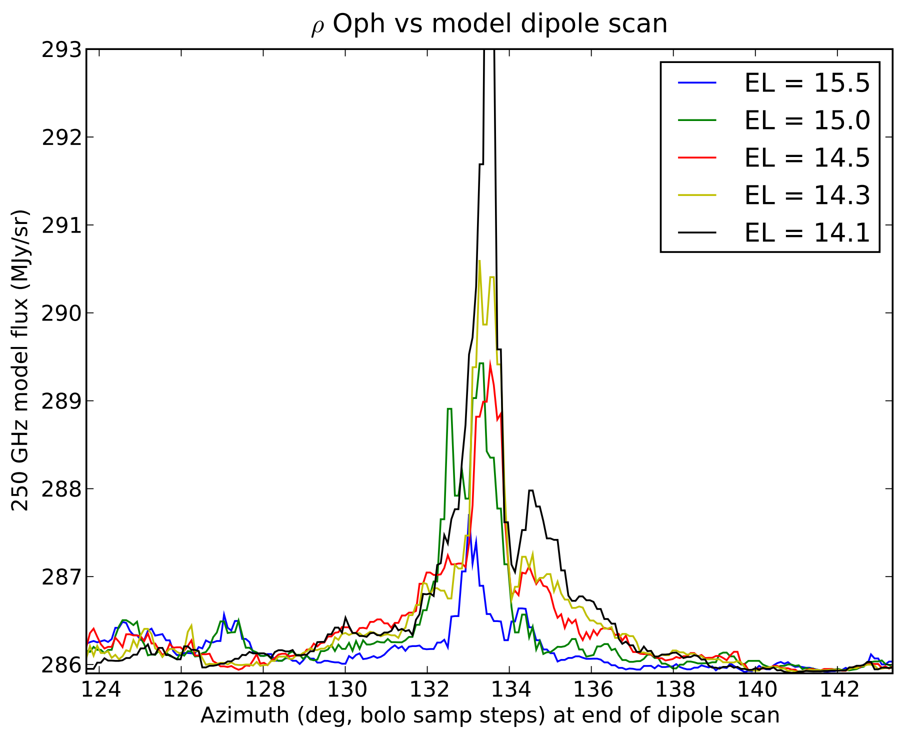

Figure 6.8: Cuts in azimuth of the 250 GHz flux model in the vicinity of ρ Ophiuchi during the dipole scan, for different values of scan elevation. While the brightest dust feature is always found near 133° azimuth, the peak flux varies from ~ 1 to more than 7 MJy/sr as the scan elevation falls from 15.5° to 14.1°. The true elevation pointing for the 250 GHz bolometers was probably around 14.5° to 15°.

This will pose a complication if we are able to detect ρ Ophiuchi in the dipole scan dataset, since the precise elevation pointing during the dipole scan remains unknown. The pointing for the instrument during the dipole scan plausibly ranges from 14° to 15.5°, and as illustrated in Fig. 6.8 the excess flux near ρ Ophiuchi varies by a factor of seven over that range.

6.1.5 Azimuth binning and simulated timestreams

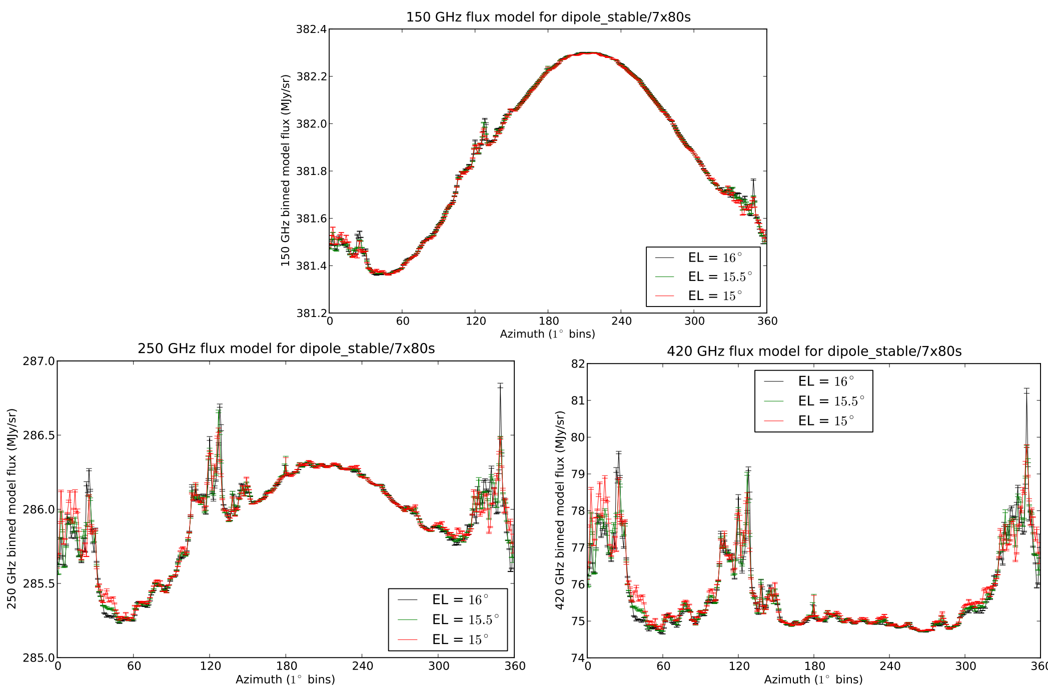

Figure 6.9: Flux timestreams for the stable rotation portion of the dipole scan, binned to 1° in azimuth, for the 150 (top), 250 (lower left), and 410 (lower right) GHz bands. Each plot includes lines for multiple plausible boresight elevation pointings. The error bars indicate the variance of the mean of the samples in each bin, i.e. $\sigma/\sqrt{N}$.

Because the instrument pointing is set at a fixed elevation, because the uncertainty in that pointing is comparable to width of the stripe swept out by the instrument during the dipole scan, and because the dipole scan contains a rather limited number of scans, we will not attempt to make two dimensional maps from dipole scan data. For any pixelization with reasonably square bins, most pixels would suffer from a very low number of samples per bin.

Instead, we will integrate by binning in azimuth, and introduce a common procedure that can be applied to both the simulated timestreams from the flux model and, later, to bolometer timestreams. In light of the characteristic feature scales involved, we divide the sky here into 360 1° azimuth bins. Then the contents of bin n are

$$B_n = \Big\{ i \mid \alpha_i \in \Big[n^\circ, (n+1)^\circ \Big) \Big\}$$

where α_i is the azimuthal pointing of the instrument at sample i, and n ranges from 0 to 359. We compute the mean and standard deviation of the mean in each bin

$$\mu_n = \frac{1}{N_n} \sum_{i \in B_n} s_i \tag{6.3}$$

$$\sigma_n = \frac{\sigma(B_n)}{\sqrt{N_n}} = \frac{1}{N_n} \sqrt{\sum_{i \in B_n} (s_i - \mu_n)^2} \tag{6.4}$$

where s_i are the samples in the timestream, and N_n the number of samples in bin n.

Each panel of Fig. 6.9 plots for one observing band the bin mean values μ_n with error bars σ_n, for the simulated flux timestream corresponding to the stable rotation period of the dipole scan. As expected, we see that the CMB dipole is the dominant component of the 150 GHz azimuth profile, while the dipole is relatively insignificant compared to dust emission at 410 GHz. In all three bands it is possible to discern a broad complex around 130° azimuth, which corresponds to the Ophiuchus dust emission features, as well as several emission complexes on either side of 0° azimuth corresponding to the low point of the scan in galactic latitude.

Note that in this case no noise term has been added to the flux timestream, and the bin errors σ_n are thus purely a function of the amount of structure in the model within a bin. The fact that the error bars are small compared to the range of the overall azimuthal profile indicates that the largest components of the sky signal incident on the bolometers will arise from large-scale structures and the CMB dipole itself. Therefore, when we desire wider integration, or for convenience of display, we will generally use 2° bins.

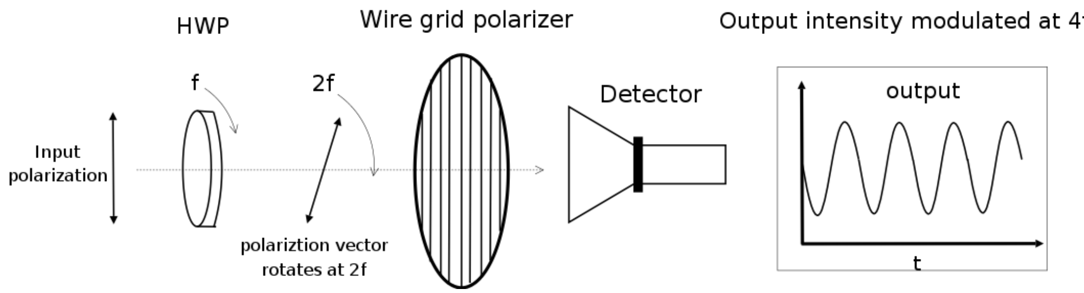

Figure 6.10: Schematic diagram illustrating the principle of rotating HWP polarimetry. Polarized light enters from the left and passes first through the HWP rotating at frequency f and then a polarizing grid before being detected. As described in the text this results in the input polarization fraction and angle being modulated at $4f$ into the amplitude of the detected signal. Figure courtesy B. Johnson[23].

6.2 HWP Template Removal

6.2.1 Review of HWP Polarimetry

As mentioned previously, the purpose of the rotating half-wave plate (HWP) is to modulate the linear polarization of light passing through it such that the Q and U Stokes vectors are encoded into the power timestream measured by the bolometers. This occurs because rotating a HWP in a beam of linearly polarized light with angular frequency f causes the polarization angle to rotate at twice the angular frequency, or $2f$. A 180° rotation of the polarization angle, corresponding to a 90° rotation of the HWP, is then an eigenfunction of the system that leaves the Q and U vectors unchanged except for reflective losses. Given a linear polarizing grid aligned with the $+Q$ state and a constant input polarization state, the power transmitted will vary as a sinusoid with angular frequency $4f$, with amplitude proportional to $Q + U$ and phase $\tan(Q/U)$. The method of polarimetry used in EBEX is to extract this $4f$ sinusoid component from the signal recorded by a bolometer and reconstruct the incident Q and U states for making maps.

Again using the notation of Johnson[23], the resulting signal takes the form

$$s_i = \frac{1}{2}\Big[I(t_i) + Q(t_i)\cos(4\rho_i) + U(t_i)\sin(4\rho_i)\Big] \tag{6.5}$$

where I, Q, and U are the Stokes parameters incident at the HWP, the result of polarization arriving at the telescope, plus instrumental polarization, as modified by any cross-polarization present. ρ is the instantaneous orientation angle of the HWP, and t represents time. All of these terms are part of a discrete timestream indexed by i. In general we are interested in the time-varying components of Q and U produced as the telescope scans across the sky, not the constant term likely arising from instrumental polarization, and thus the information of interest in this signal lies in the sidelobes of $4f$.

Unfortunately the rotation of the HWP does not simply modulate optical polarization signals into the bolometer timestream as sidelobes of $4f$. Defects in the HWP or nonuniformities in its motion can be expected to generate signals in the bolometer timestreams at arbitrary harmonics of its rotation frequency. In practice, we find that HWP rotation induces signals in the timestream at the first 8-10 harmonics of f (see the top panels of Figs. 6.11 and 6.13), and these signals are typically the largest spectral components of the timestream. They are stationary in time, and thus appear as sharp spikes in the periodogram, which can be completely described in terms of harmonic number, phase, and amplitude. The periodic signal that is the combination of these harmonic terms is called the HWP template.

Because the HWP template typically swamps other signals in the timestreams of the bolometers open to light, we remove this signal before proceeding with further analysis. Below, Sec. 6.2.2 describes the process of parametrically obtaining the HWP template from a timestream and knowledge of the HWP orientation angle, and Sec. 6.2.3 describes the algorithm developed to robustly fit and subtract the template from a timestream.

6.2.2 HWP Template Fitting

As the HWP rotates each optical angular encoder produces a stream of pulses from which the orientation of the HWP at each encoder slot can be reconstructed with an instantaneous accuracy of $0.03°$[12]. As the HWP optical encoder has 120 fixed slots, this procedure yields a sequence of angular orientation samples that are even spaced in angle, but potentially variably spaced in time. For the North American flight, this stream is sampled at $120f \approx 240$ Hz. The *interpX* programs (see Sec. 5.7) include functionality to resample the encoder-synchronous angle data to create an `angle` channel in the bolometer dirfiles that is sampled synchronously to the bolometers.

Once the bolometer-synchronous HWP orientation sequence is obtained, we model

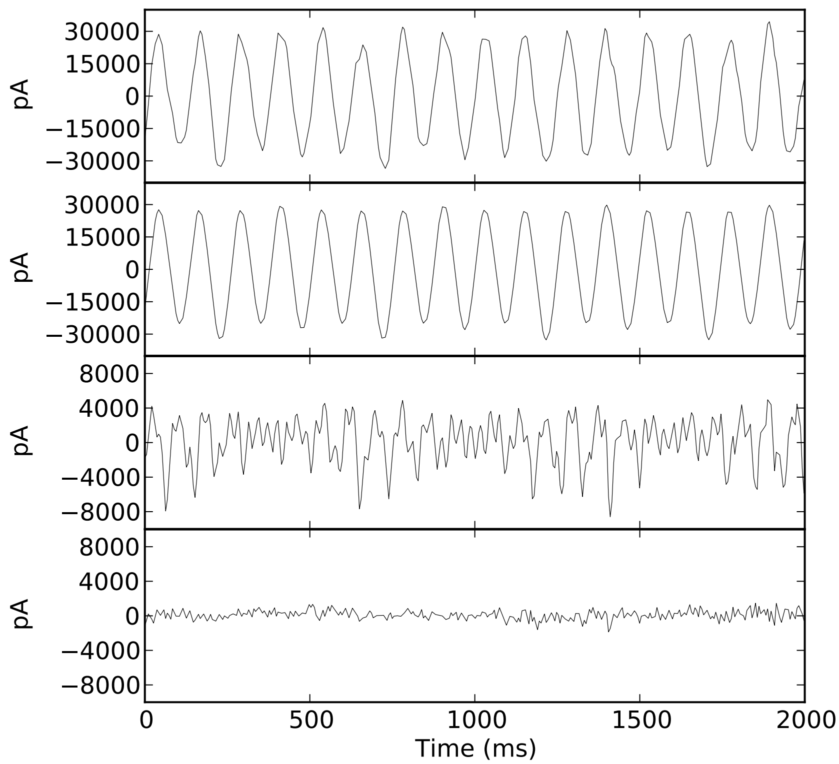

Figure 6.11: Illustration of HWP template fitting and removal. Shown here is a segment of timestream data (in pA of current) for low noise light 250 GHz bolometer b56_w2_c3 for two seconds (four rotations of the HWP) during the NA flight. The top panel plots raw datapoints from the DfMux system, which are dominated by the periodic HWP template. Below that is the best-fit template, obtained by fitting the sin/cos terms of the $n = 1, \ldots, 8$ harmonics of the HWP rotation angle according to the procedure described in Sec. 6.2. In the third panel the difference of the two signals is plotted, revealing the underlying noise structure. In the bottom panel electronic noise frequencies in the readout system have been removed as well, according to the procedure described in Sec. 6.3. The y-axis of the top pair of plots uses the same scaling, and likewise for the bottom pair.

the HWP-synchronous signal (HWPSS) as

$$
\begin{aligned}
\langle h_i \rangle = \sum_{n=1}^{N_{harm}} & A_n \cos(n \cdot \rho_i) + B_n \sin(n \cdot \rho_i) \\
& + A'_n t \cos(n \cdot \rho_i) + B'_n t \sin(n \cdot \rho_i)
\end{aligned}
\tag{6.6}
$$

We call this estimator $\langle h_i \rangle$ the HWP template. It is constructed to include terms linear in time to allow for the template amplitude to drift in time (e.g. tracking slow drifts in detector sensitivity). Note that variations in the HWP rotation frequency are captured naturally, because the sinusoidal terms are functions of the HWP orientation angle, not of time.

Assuming the HWPSS is a meaningful component of the total signal recorded for a bolometer, we can obtain the HWP template by using Eq. 6.6 as a fitting function for the bolometer datastream. By precomputing the sine and cosine harmonic sequences, we can efficiently find the maximum-likelihood coefficients that yield

$$d_i \approx \langle h_i \rangle$$

using LU decomposition to solve the resulting system of linear equations. The module `hwp_removal`, which derives from the work of Johnson[23], implements this approach in C using the GNU Scientific Library[76]. For ease of integration with other components of our toolchain, we have also developed a Python module `hwprem` that provides access to `hwp_removal`. Compare the top two panels of Fig. 6.11 for an example of a raw bolometer data stream and the HWP template fitted from that data. The residual left after subtracting this template from the raw data is shown in the third panel from top in that plot.

6.2.3 Template Removal Algorithm

Given the high detector count and large data volumes encountered in EBEX, we need a procedure to make use of this template fitting algorithm that will operate robustly in the absence of close human supervision. From experience, we have found that the following conditions can lead to a poor quality fit:

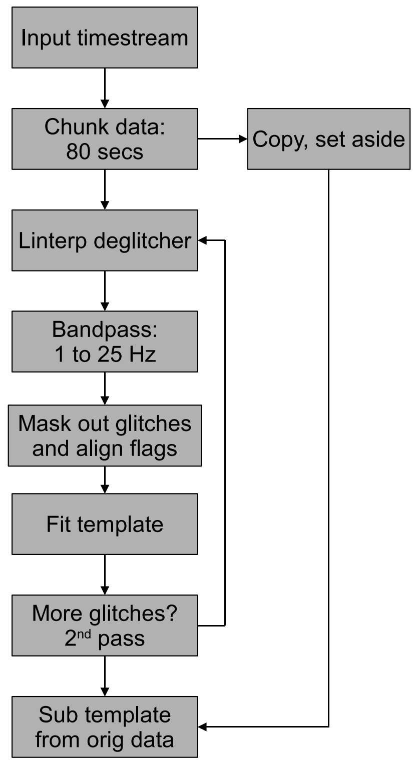

Figure 6.12: Flowchart summarizing the HWP template removal algorithm.

- **Problem:** The amplitude of harmonic terms in the signal varies.

  Solution: Use a relatively short processing interval and iterate through the time series.

- **Problem:** Large $1/f$ drifts.

  Solution: Highpass the timeseries with cutoff frequency well below f.

- **Problem:** High noise levels increase the errors in the fit.

  Solution: While Gaussian noise is not normally a problem, lowpass filtering the timeseries with cutoff frequency above the highest harmonic of interest can improve performance.

- **Problem:** Large glitches or LED calibrator flashes perturb the fit.

  Solution: Mask or remove glitches before fitting.

- **Problem:** Small glitches swamped by the HWPSS still perturb the fit.

  Solution: Subtract the first pass fitted template and run a second pass.

These considerations lead to the algorithm depicted as a flowchart in Fig. 6.12. Based on this we have developed a set of Python functions that implements a standardized workflow for bolometer datastreams. These functions begin by reading 80 second chunks[1] of raw bolometer data and setting aside a copy. The chunk is scanned for spikes with a 5.5σ threshold, and those spikes are added to a mask list. The data is then bandpassed with an 8-pole Butterworth filter that has low and high cutoff frequencies of 1 and 25 Hz, respectively. After this processing, a mask is generated as the union of the spikes found and any flags set during timestamp alignment, and the unmasked data is fit for 10 harmonics using `hwprem`.

At this point, the fit template is subtracted from the processed chunk and a second 5.5σ scan is made for spikes that were hidden by the HWPSS in the first pass. If any new spikes are found, the process is repeated for a second pass with the newly found spikes added to the mask list.

If no new spikes are found, or else at the end of the second pass, the processed chunk is discarded. The procedure returns the fitted template $< h_i >$ and the template subtracted raw data $d_i - < h_i >$, and these sequences are written to disk as new dirfile fields with `_temp` and `_tod` extensions, respectively. Future processing can then read the `_tod` data directly.

In the typical case, the residual power in harmonics of the HWP rotation frequency is reduced to the noise level of the original signal. Fig. 6.13 shows the power spectrum of an 80 second chunk of bolometer data from a low noise light 250 GHz bolometer before and after processing. Note that in that figure, for the sake of clarity the signal in both panels has also been subjected to the line removal process described in Sec. 6.3.

This code runs quickly enough that it can be run interactively in small batches (typically several seconds runtime per hour of data per bolometer) if, for example, one wishes to prepare a dataset where the chunks are aligned to a particular boundary. We have also used this code on the parallel machine `elmo` at the Minnesota Supercomputing

[1] Strictly, each chunk is 80.5306368 seconds long. For the sake of efficient FFTs we have rounded the second up to 192 bolometer samples.

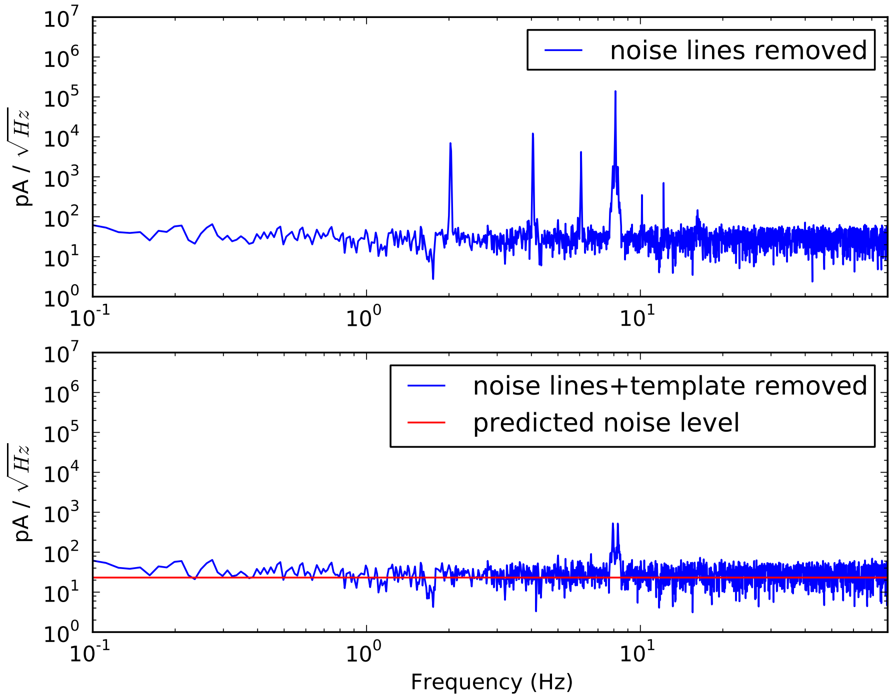

Figure 6.13: Example of HWP template removal performance. Plotted here are the frequency spectra for low noise light 250 GHz bolometer b56_w2_c3, before and after HWP template removal. In the top panel the peaks at harmonics of the $f = 2$ Hz HWP rotation frequency comprise the HWP rotation synchronous signal (HWPSS). In the lower panel this signal has been removed according to the algorithm described in Sec. 6.2. Still apparent near 8 Hz are sidelobes of $4f$, the result of HWP modulation of optical polarized signals. Also shown is the predicted noise level for this bolometer. The data segment displayed corresponds to a quiescent period during the NA flight commanded for the purpose of making bolometer noise measurements. Nevertheless, electrical interference in the readout system generated several narrow peaks, which have been removed from both panels according to the procedure in Sec. 6.3 for clarity.

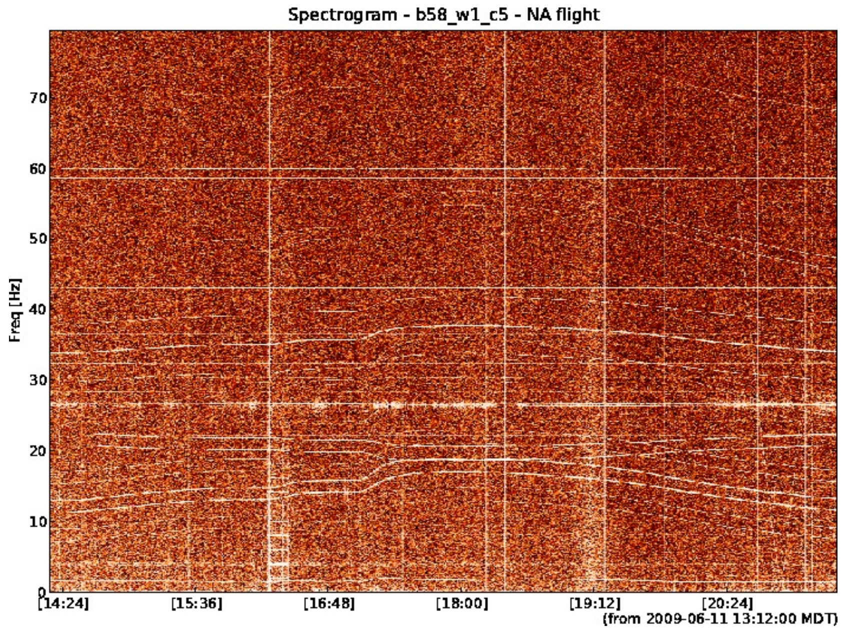

Figure 6.14: Spectrogram of light 410 GHz bolometer b58_w1_c5 during the North American test flight, from the completion of bolometer tuning to termination. The data has undergone HWP template subtraction but not yet been further processed. The color stretch is approximately logarithmic in $W/\sqrt{\mathrm{Hz}}$ units, but has been adapted to enhance the contrast.

Institute, where we were able to template subtract the entire dataset from the North American test flight in about 40 minutes using 44 cores.

6.3 Narrow Line Noise

In addition to the strong lines in frequency domain that result from the HWPSS and that can be removed via template subtraction, most bolometer timestreams exhibit many other frequency domain features that are best understood by reference to a spectrogram visualization. The spectrogram visualization used here computes a separate periodogram for each 30 second segment of the timestream, and plots the periodogram values as intensity in a vertical column of pixels. The color stretch is approximately logarithmic, but employs a pixel intensity histogram normalization to enhance the contrast of faint features.

Fig. 6.14 displays a spectrogram of the timestream of a light 410 GHz bolometer chosen because it exhibits moderate noise and a typical number of frequency lines. Sharp vertical lines are indicative of momentary noise spikes, glitches, or calibrator flashes. Sharp horizontal lines indicate constant-frequency narrow line noise, while lines that deviate from horizontal indicate narrow lines that move with time. This last category has been correlated with variations in the temperature of the DfMux boards, although not all moving lines fit that pattern. At this time all of these narrow lines are suspected to be the result of noise or interference in the readout electronics. Many specific lines were common to several bolometers, but none were found to affect all bolometers, and most bolometers also exhibited at least one line with a unique frequency.

To remove the narrow line features we take advantage of the fact that over sufficiently short timescales all such features are stationary, in which case we can remove them in the frequency domain. Moreover, we do not observe any lines below about 1.5 Hz, although during the dipole scan many bolometers show a strong moving line at 1.6 Hz, and the underlying noise spectrum above 1.5 Hz is generally very flat (see Fig. 6.13).

Therefore we developed a narrow line finder that operates on 80 second chunks, chosen to match the existing chunking used for HWP template removal. Each chunk is Fourier transformed to frequency domain, where a 2σ peak finder flags all narrow lines above 1.5 Hz and not within 0.5 Hz of the 8.01 Hz HWP 4th harmonic. The flagged regions are filled with Gaussian random complex data at the mean white noise level, and the chunk is transformed back to time domain.

Because glitches or LED flashes causing sharp spikes in the time domain can ring strongly in frequency domain, all chunks are deglitched at this stage if they have not been already. In this and subsequent processing, a standardized two-pass deglitcher is employed. An 8σ spike finder scans for spikes, clears the identified sample ranges, and linearly interpolates across them. Then a second pass is performed, with the threshold set at 5σ. Finally the filled region is added with Gaussian random noise at the signal RMS level.

Fig. 6.15 presents spectrograms that illustrate this procedure and the HWP template removal procedure working on a light 410 GHz bolometer for data corresponding to the stable rotation portion of the dipole scan. In the chunk between 21:11 and 21:13 MDT (3:11 and 3:13 UTC) there is a period of elevated noise that reduces the effectiveness of

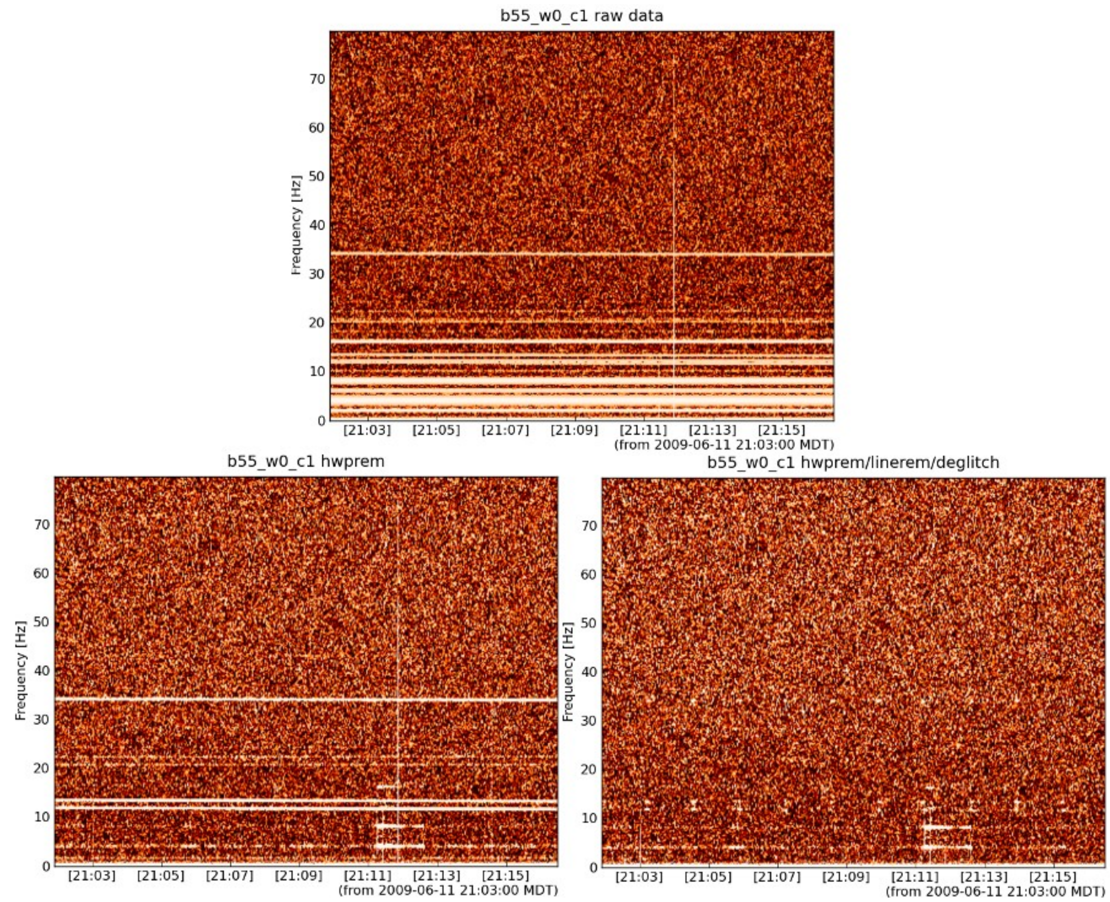

Figure 6.15: Spectrograms of the timestream for light 410 GHz bolometer b55_w0_c1 during the dipole scan illustrating the template and line removal operations of Secs. 6.2 and 6.3. Top: the unprocessed timestream. Lower left: timestream after HWP template removal. Lower right: timestream after template and line removal. In each case the data are being processed in 80 second chunks.

HWP template removal. It is unknown whether the association between this period and the LED calibrator flash at 2:12 UTC is coincidental. However, this period of elevated noise is common to many of the light 250 and 410 GHz bolometers, and if the chunk boundaries are adjusted it is possible to obtain a result in which the high noise chunk falls immediately after the LED flash, while the chunk containing the flash is nominal.

The bottom panel of Fig. 6.11 shows a segment of time-domain data after both template and line noise removal. The lower panel of Fig. 6.13 is also representative of the power spectrum of bolometer data after these two operations have been completed.

6.4 Bolometer Selection and Data Cuts

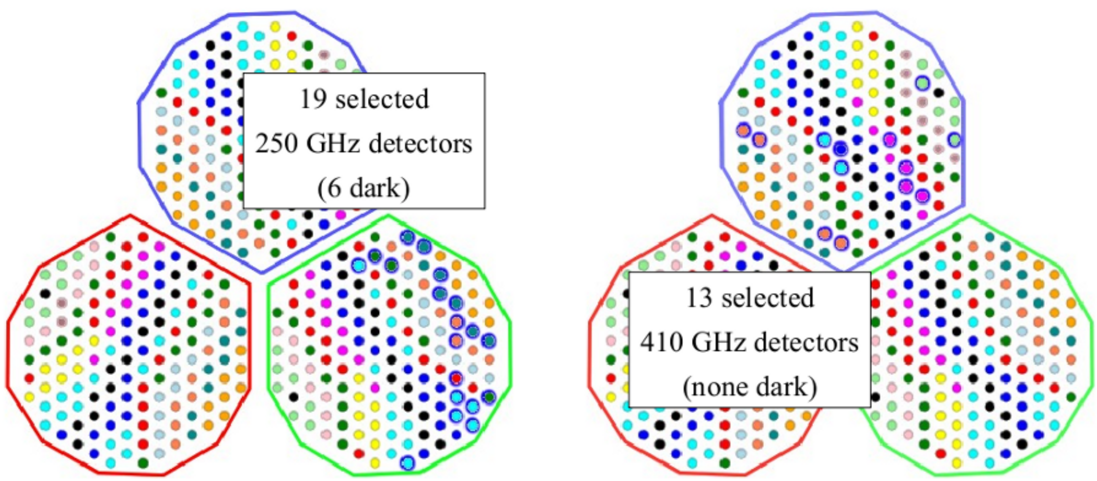

Figure 6.16: *jsviz* plot of the NA flight focal plane highlighting the 250 and 410 GHz bolometers selected for further analysis on the basis of functionality and acceptable noise performance. The detectors are color coded by multiplexing module.

6.4.1 Selecting bolometers

In the aftermath of the test flight, the EBEX bolometry team compiled a significant amount of information about each bolometer. The relevant properties here are:

- Was the bolometer read out?

- Did the bolometer evidence a superconducting transition (display a turnaround in its IV curve)?
- Was the bolometer latched superconducting, either during tuning or later in the flight?
- What type of detector was this (light, dark, eccosorb plugged, other)?
- What was the measured noise level of the bolometer?
- What was the measured calibration of counts to incident power?

The set of bolometers available for further analysis is relatively small due to the fact that the dipole scan took place after the bolometer noise testing phase of the test flight. During that phase, one experiment conducted was to drop sets of bolometers deeper into the superconducting transition and take performance measurements. A result of this course of action was that many previously functioning groups of bolometers became latched in the superconducting state and unusable.

As part of the work described previously, we also tabulated the number and frequency of spurious narrow lines in frequency domain for each bolometer during the dipole scan.

Aubin has observed[27] that bolometer noise levels fall into broad populations when compared against the noise level predicted based on fabrication properties. He defined three categories: bolometers for which the noise level is between 80% and 200% of the predicted level; those for which the ratio is between 80% and 300%; and all others. Here we refer to the first two groups as "low" and "medium" noise bolometers.

We developed a set of Python classes that parse the various spreadsheets in which the answers to these questions can be found and used them to create a database from which subsets of bolometers satisfying certain criteria could be selected. Tables 6.1 and 6.2 list the properties of the bolometers we have selected for further study. These are bolometers that, in accordance with the list above, are read out, exhibit a turnaround, are never latched, are either light or dark, and have either low or medium noise. These criteria identify 19 250 GHz bolometers and 13 410 GHz bolometers; we use the shorthand "ok250" and "ok410" to denote these collections.

Bolometer Identifiers					
Board/Wire/Channel	Wafer location	Noise bin	$-1\times$aW/count	Lines	Dark?
b52_w3_c4	250-14-01	low	11225	2	y
b56_w1_c4	250-09-10	low	9562	18	
b56_w1_c7	250-08-11	low	11225	22	
b56_w2_c0	250-06-11	low	10255	15	
b56_w2_c2	250-02-09	low	7484	25	
b56_w2_c3	250-03-10	low	7899	21	
b56_w2_c4	250-05-11	low	10394	23	
b56_w2_c5	250-07-11	low	10810	19	
b56_w2_c6	250-09-11	low	10532	18	
b56_w2_c7	250-10-11	low	9562	21	
b57_w0_c6	250-11-08	low	8592	25	
b57_w1_c1	250-03-08	medium	10671	21	
b57_w1_c3	250-02-07	low	9839	24	
b57_w1_c7	250-13-08	low	12057	6	y
b57_w3_c0	250-02-06	medium	9978	18	
b57_w3_c4	250-13-07	low	11225	7	y
b57_w3_c5	250-14-05	low	9701	6	y
b57_w3_c6	250-12-07	low	10671	13	y
b57_w3_c7	250-13-06	low	11225	5	y

Table 6.1: The ok250 bolometer subset; see the text (Sec. 6.4) for selection criteria. The first two columns identify the bolometer, first by readout ID, then by focal plane coordinate. The noise bin, aW/count, number of lines, and whether the bolometer was light or dark are among the bolometer properties described in the text.

In these tables the Board/Wire/Channel designation identifies the bolometer as part of the readout system, associated with a particular channel on the given multiplexing module of the given DfMux board. Bolometers are also identified by focal plane coordinates, which specify a wafer and a detector row and column on that wafer. For the North American flight, since we flew one wafer for each band, the three wafers are simply identified as "150," "250," and "410."

Also of potential interest are the eccosorb plugged bolometers; at these positions in the focal plane eccosorb has been inserted into the waveguide array to attenuate incoming radiation. While intended to facilitate ground calibration experiments by providing bolometers that will not saturate at high loading, at float these bolometers

Bolometer Identifiers				
Board/Wire/Channel	Wafer location	Noise bin	$-1\times$aW/count	Lines
b55_w0_c0	410-06-05	low	30026	6
b55_w0_c1	410-04-04	medium	28179	7
b55_w0_c2	410-02-03	low	48042	4
b55_w0_c4	410-03-04	low	32336	6
b55_w3_c0	410-04-01	medium	29103	10
b55_w3_c2	410-08-02	medium	29565	8
b58_w1_c0	410-02-08	low	31874	11
b58_w1_c1	410-03-09	low	30950	14
b58_w1_c5	410-10-10	medium	23559	18
b58_w1_c6	410-11-10	medium	31412	6
b59_w2_c0	410-07-07	medium	30950	8
b59_w3_c2	410-06-08	low	31874	8
b59_w3_c3	410-08-08	low	31874	7

Table 6.2: The ok410 bolometer subset; see the text (Sec. 6.4) for selection criteria. The first two columns identify the bolometer, first by readout ID, then by focal plane coordinate. The noise bin, aW/count, and number of lines are among the bolometer properties described in the text. No selected 410 GHz bolometers were dark.

can be used as "mostly-dark" detectors. These are listed in Table 6.3.

These tables also record a responsivity calibration in aW/count. This number is based on ground measurements using a chopped cold load at the window, and should thus be independent of the unknown optical efficiency of the EBEX cryostat optics. These numbers should however be regarded with some caution, since the different loading environment, lower bath temperature, and changed tuning parameters at float may have caused the responsivity of some or all detectors to change[15, 16]. Note that the sign of the responsivity is negative: the configuration of the filters in the readout chain was such that an increase of one count corresponds to an increment in the bias current, and thus a decrement in the incident power at the bolometer.

Bolometer Identifiers		
Board/Wire/Channel	Wafer location	−1×aW/count
b53_w1_c5	250-09-04	32072
b56_w1_c1	250-03-09	36824
b56_w2_c1	250-04-10	32468
b57_w0_c5	250-10-08	36032
b54_w3_c0	410-08-06	86890
b55_w2_c6	410-05-02	76991
b58_w1_c2	410-05-10	82490

Table 6.3: The eccosorb plugged bolometers that were not latched. The first two columns identify the bolometer, first by readout ID, then by focal plane coordinate. The responsivity in aW/count was measured after the eccosorb plugs were inserted at these focal plane positions.

Because these responsivity values are referenced to power outside the cryostat, we can also express them in terms of flux. The two quantities are related by

$$\frac{1\ \mathrm{aW}}{A \cdot \Omega \cdot \Delta\nu} = \frac{1\ \mathrm{aW}}{\mathrm{m}^2 \cdot \mathrm{Hz} \cdot \mathrm{sr}} \left(\frac{1\ \mathrm{m}^2}{A}\right) \left(\frac{1\ \mathrm{sr}}{\Omega}\right) \left(\frac{1\ \mathrm{Hz}}{\Delta\nu}\right) \tag{6.7}$$

$$= 10^8\ \frac{\mathrm{Jy}}{\mathrm{sr}} \left(\frac{1\ \mathrm{m}^2}{A}\right) \left(\frac{1\ \mathrm{sr}}{\Omega}\right) \left(\frac{1\ \mathrm{Hz}}{\Delta\nu}\right) \tag{6.8}$$

$$= 10^{-7}\ \frac{\mathrm{MJy}}{\mathrm{sr}} \left(\frac{1\ \mathrm{m}^2}{A}\right) \left(\frac{1\ \mathrm{sr}}{\Omega}\right) \left(\frac{1\ \mathrm{GHz}}{\Delta\nu}\right) \tag{6.9}$$

where A is the effective telescope collecting area accounting for the truncated Gaussian profile of the beam at the aperture, $\Delta\nu$ is the bandwidth of each observing passband, and Ω is the solid angle of the telescope beam on the sky. These values for the three observing bands are tabulated here in Table 6.4.

Band (GHz)	ν_{low} (GHz)	ν_{high} (GHz)	$\Delta\nu$ (GHz)	$A \cdot \Omega$ $\mathrm{m}^2{\cdot}\mathrm{sr}$
150	133	173	40	3.24×10^{-6}
250	218	288	70	1.44×10^{-6}
410	266	450	84	5.36×10^{-7}

Table 6.4: Band edges, bandwidths, and $A \cdot \Omega$ for the EBEX observing bands.

We can then obtain the conversions, using `dustsfd` to also convert flux to thermodynamic temperature units in each band:

$$\begin{aligned}\frac{1\ \mathrm{aW}}{A\cdot\Omega\cdot\Delta\nu} &= 7.72\times10^{-4}\ \mathrm{MJy/sr} = 1.94\ \mu\mathrm{K} \quad \text{at } 150\ \mathrm{GHz}\\ &= 9.91\times10^{-4}\ \mathrm{MJy/sr} = 2.12\ \mu\mathrm{K} \quad \text{at } 250\ \mathrm{GHz}\\ &= 2.23\times10^{-3}\ \mathrm{MJy/sr} = 11.2\ \mu\mathrm{K} \quad \text{at } 410\ \mathrm{GHz}\end{aligned} \tag{6.10}$$

For reference, using these conversions, the 3360 μK CMB dipole equates to a beam power of 1731, 1584, and 300 aW at 150, 250, and 410 GHz, respectively.

6.4.2 Data restriction: time and frequency domain

We also restrict the span of time under study. As previously noted in Sec. 6.1, the gondola was placed into stable rotation from approximately 3:02 to 3:16:30 UTC. However, we also noted in Sec. 6.3 that a poorly understood period of elevated noise occurs at around 3:14 UTC. In order to avoid potential complications, we will avoid data from this point in time. Thus, for this analysis, we select the first seven 80-second chunks of data following 3:01:50 UTC. As previously noted in Sec. 6.2.3, each chunk is actually 80.5306368 seconds in length, so the total selected data amount to 107520 samples spanning 563.7144575 seconds.

Since this data will be binned in azimuth according to the procedure described in Sec. 6.1.5, we can discard frequency components that would only increase the variance in our bins after other processing is complete. At an average rotation speed of 16.7°/s, scan-synchronous signals (SSS) such as the CMB dipole will appear at about 46 mHz; lower frequencies can be interpreted as $1/f$ noise. Similarly, signals corresponding to less than one-half a degree motion on the sky, which would be subsumed into a bin, will appear above 33 Hz. Therefore we will bandpass all bolometer data using 8-pole Butterworth filters with band edges at 30 mHz and 40 Hz. Applying this bandpass to the simulated flux timestream changed the mean of no bins by more than 10^{-3} MJy/sr, but reduces the standard deviation in the typical bin by a factor of 2.5. The effect of this filter in the frequency domain is illustrated in Fig. 6.17. That plot demonstrates that the low-frequency cutoff is below the scan-synchronous peak, while the high-frequency cutoff occurs where the model power falls far below the expected noise level.

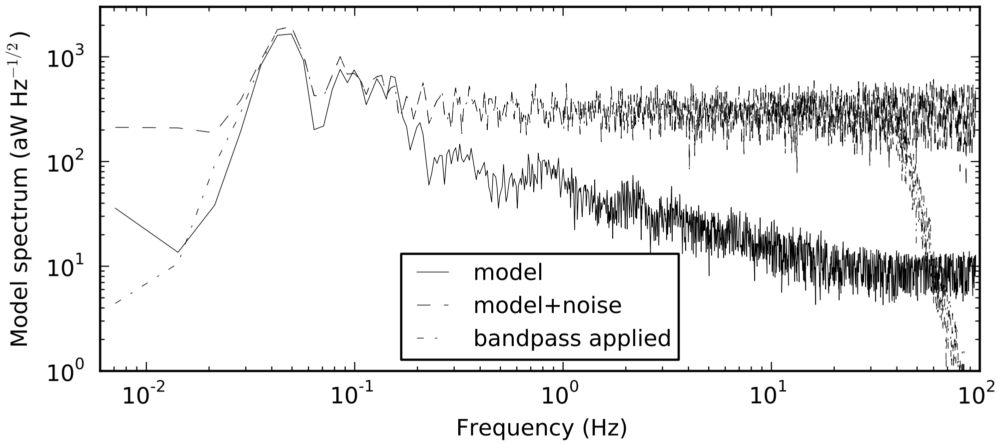

Figure 6.17: Spectrum for one detector sampling the 250 GHz flux model during the stable portion of the dipole scan. The solid line reflects the raw model. The dashed line adds the nominal noise per sample from Eq. 6.15. The dash-dot line further applies the bandpass filter discussed in Sec. 6.4.2.

6.5 Scan-Synchronous Signal

Once data merging, timestamp alignment, and resampling to the bolometer data rate are complete, the standard processing chain for data from a selected bolometer is then:

- HWP template subtraction (fetch template subtracted data from disk)
- Split into 80 second chunks
- Two-pass glitch/spike removal
- Narrow line noise removal
- Bandpass between 30 mHz and 40 Hz
- Scale values from DfMux counts to power (aW)

In Figs. 6.18, 6.19, and 6.20 are displayed the result of this processing chain for the ok250, ok410, and eccosorb plugged bolometers, binned to 2° according to the procedure in Sec. 6.1.5.

It is immediately clear that these data exhibit substantial SSS that are not obviously correlated to the expected signal from the sky, and which are many times larger than

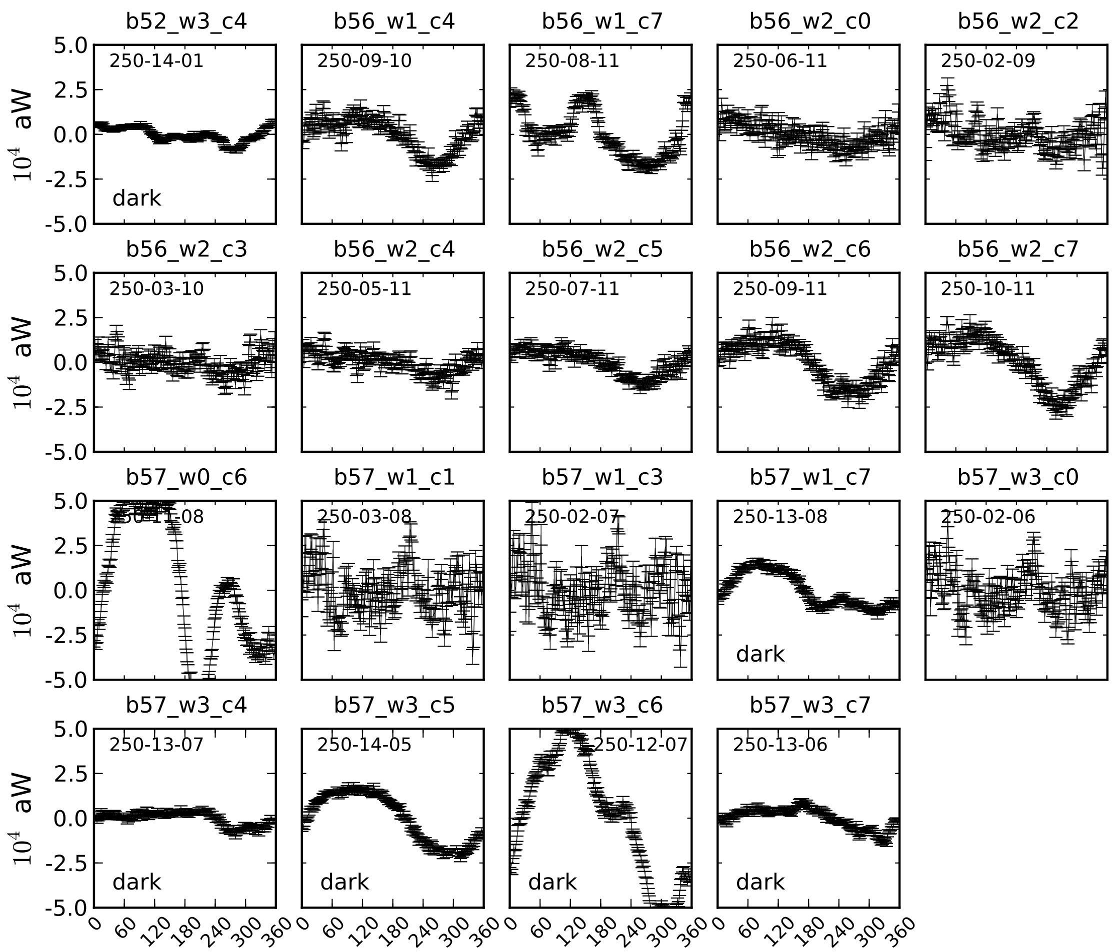

Figure 6.18: Data from the ok250 bolometer set, processed as specified in Sec. 6.5, and binned to 2°. Bolometers are identified by board/wire/channel and wafer coordinate. The six dark bolometers are noted as such.

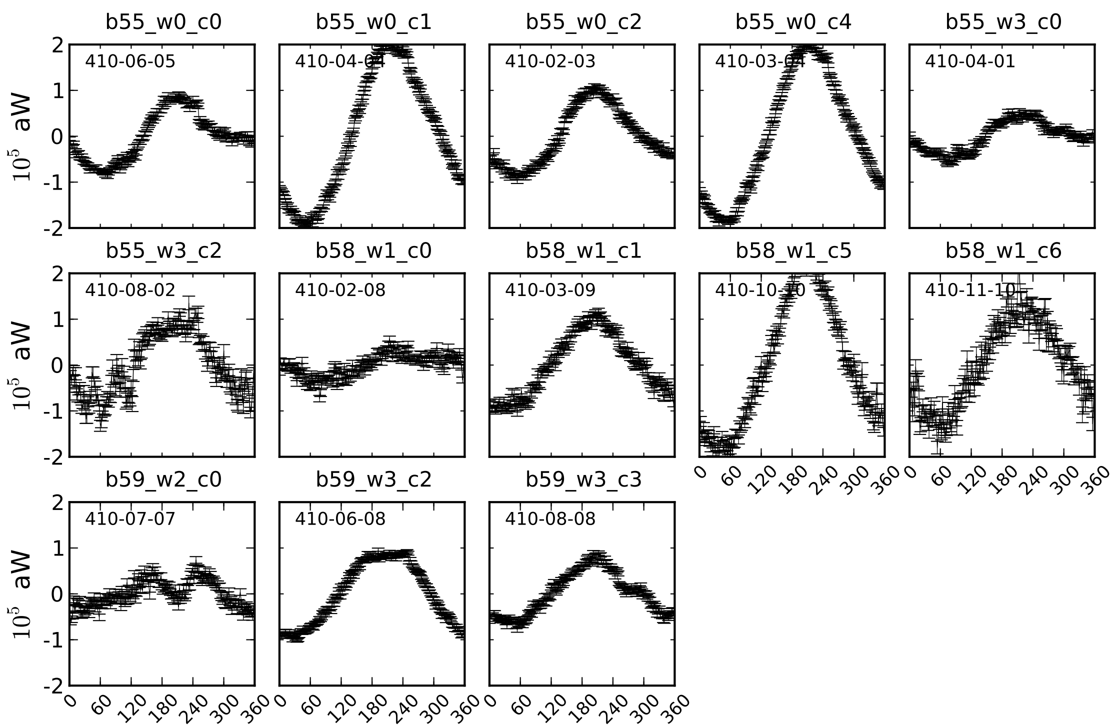

Figure 6.19: Data from the ok410 bolometer set, processed as specified in Sec. 6.5, and binned to 2°. None of these bolometers are dark.

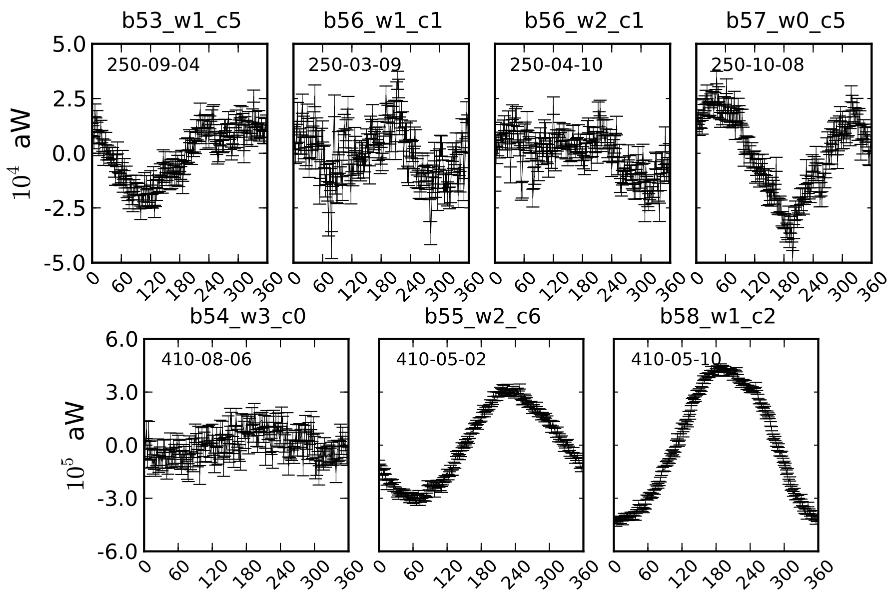

Figure 6.20: Data from the eccosorb plugged bolometers, processed as specified in Sec. 6.5, and binned to 2°. Detectors on the 250 GHz wafer are in the top row, the 410 GHz wafer below. Note that the dependent axis is scaled differently for the two bands, due to the significantly different data range.

the expected amplitude of the CMB dipole (1584 aW at 250 GHz) or the brightest dust emission bins ($\sim$ 20000 aW at 410 GHz).

Considering the ok250 set, we observe that many detectors exhibit a sinusoid SSS with maximum near 120° and minimum near 300°, but that the shape of the SSS deviates from a true sinusoid in varying ways. Meanwhile, some detectors (e.g. b56_w2_c0 and b57_w0_c6) display a very different pattern. The example of module b56_w2 is interesting, as the form of the SSS evolves from low numbered channels (corresponding to lower bias carrier frequency) to higher. Both light and dark detectors display the SSS; dark detectors appear qualitatively different only inasmuch as the error bars on the bins are uniformly smaller. This is as we would expect, given that light detectors are exposed to both higher loading and potentially varying optical signals. On the other hand, the 250 GHz eccosorb plugged bolometers both display higher bin variance and fail to conform to the SSS pattern seen in the ok250 set.

The situation with respect to the ok410 set is similar; all of the selected bolometers display a roughly sinusoid SSS with maximum near 210° and minimum near 60°, but

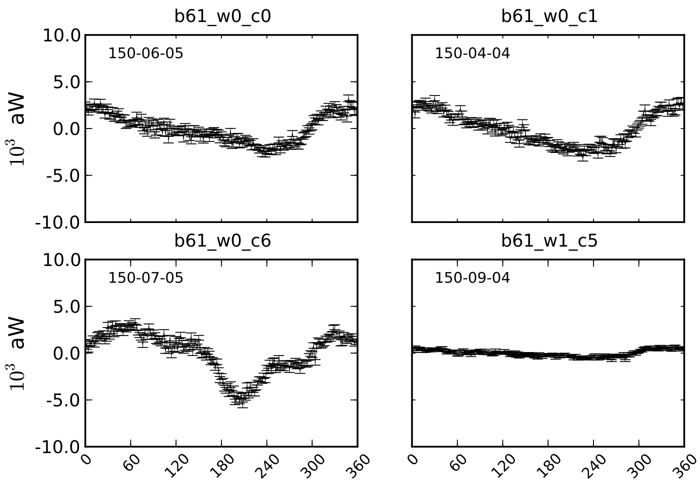

Figure 6.21: Data from the 150 GHz bolometer set, selected according to the same criteria as ok250, processed as specified in Sec. 6.5, and binned to 2°. The bolometers are all open to light.

the amplitude and smoothness of the figure varies somewhat. There are no selected dark 410 GHz bolometers, and the behavior of the eccosorb plugged bolometers is divided– two show the same SSS with even larger amplitude and low bin variance, while the third shows a weak SSS and large bin variance.

While we do not otherwise discuss the 150 GHz bolometers here, Fig. 6.21 illustrates that the situation for them is generally similar.

It is difficult to propose an explanation by which the observed SSS can be an optical signal. The SSS are much too large to be the CMB dipole, and have the wrong phase. They are also too large to be the expected dust emission, and have the wrong shape. The SSS is also approximately 90° out of phase with solar elongation. The fact that dark and eccosorb plugged bolometers also see the SSS also argues strongly against the case for an optical origin.

One possibility is that the SSS is the result of an unexpected coupling between the SQUIDs in the readout system and an external magnetic field. Such an effect would potentially affect all bolometer channels regardless of optical configuration. The differences in phase could arise from the fact that different sets of SQUIDs within the cryostat are mounted with differing orientations. If this is the mechanism, it is most likely that the external magnetic field is the Earth's, since the signal is strongly correlated to the gondola's azimuthal orientation. However, a mechanism involving magnetic fields in the pivot motor are also plausible. Others in the EBEX collaboration have set out to test this hypothesis, with no definitive results as of this writing.

6.5.1 Azimuth template removal

In order to further analyze these data, we will use the code developed for subtracting the HWP synchronous signal to subtract this azimuth synchronous signal. Unfortunately, because the sum or difference of sinusoids is another sinusoid, it is impossible to do so without also subtracting any underlying signal from the CMB dipole. Therefore at this point we abandon further consideration of the dipole signal.

Analogously to HWP template fitting, we will compute the best fit coefficients in the time domain that satisfy

$$\langle g_i \rangle = \sum_{n=0}^{N} A_N \cos(n \cdot \alpha_i) + B_N \sin(n \cdot \alpha_i) \tag{6.11}$$

$$s_i + n_i \approx d_i - \langle h_i \rangle - \langle g_i \rangle \tag{6.12}$$

Figures Figs. 6.22 and 6.23 show the result of subtracting a $N = 2$ harmonic azimuth template and binning as before. We observe that for many of the bolometers the remaining signal appears noise-like. A minority of bolometers exhibit a more complex SSS and for those large residuals remain.

6.6 Co-addition and Noise Tests

Now we wish to characterize the remaining SSS in the processed, azimuth template subtracted bolometer data. At this point we attempt to achieve additional integration by combining bolometer data streams.

We begin by excluding bolometers that (by eye) still exhibit large SSS residuals after azimuth template subtraction, making sure to reject an odd number from each set, as the next step will require an even number of timestreams. After rejecting five 250 GHz bolometers and three 410 GHz bolometers, we are left with 14 and 10 timestreams, respectively.

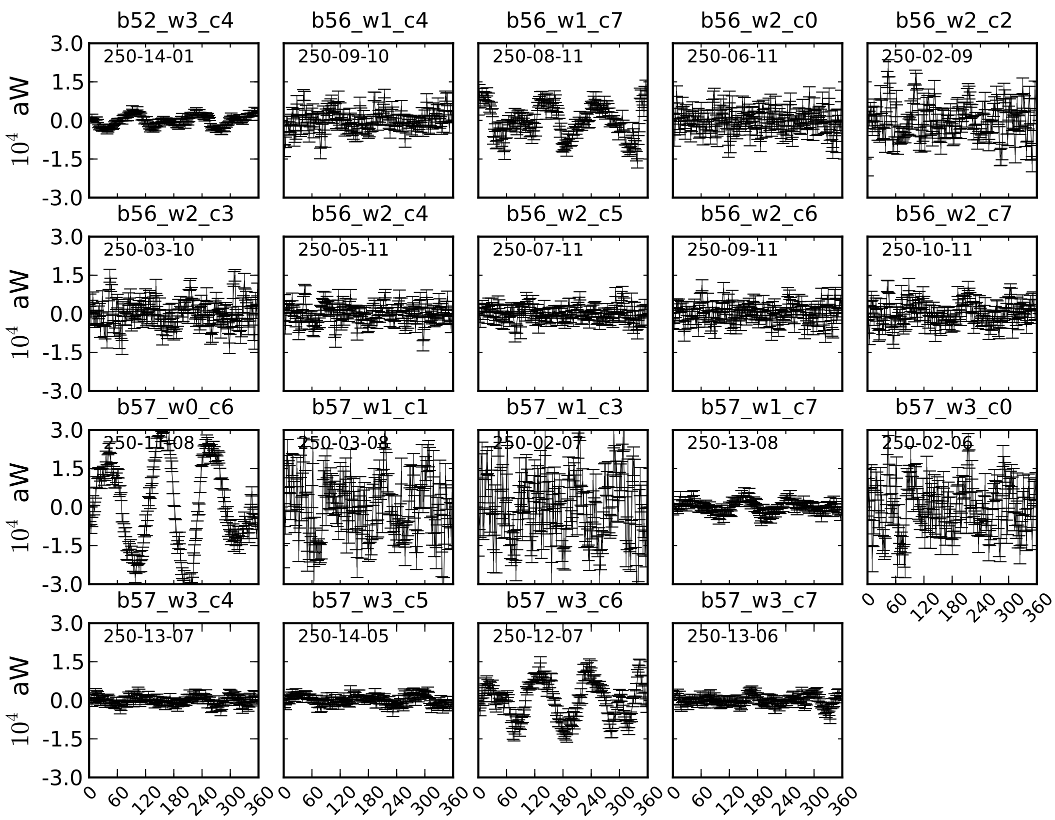

Figure 6.22: Selected data from the ok250 bolometer set, after subtraction of a 2 harmonic azimuth template.

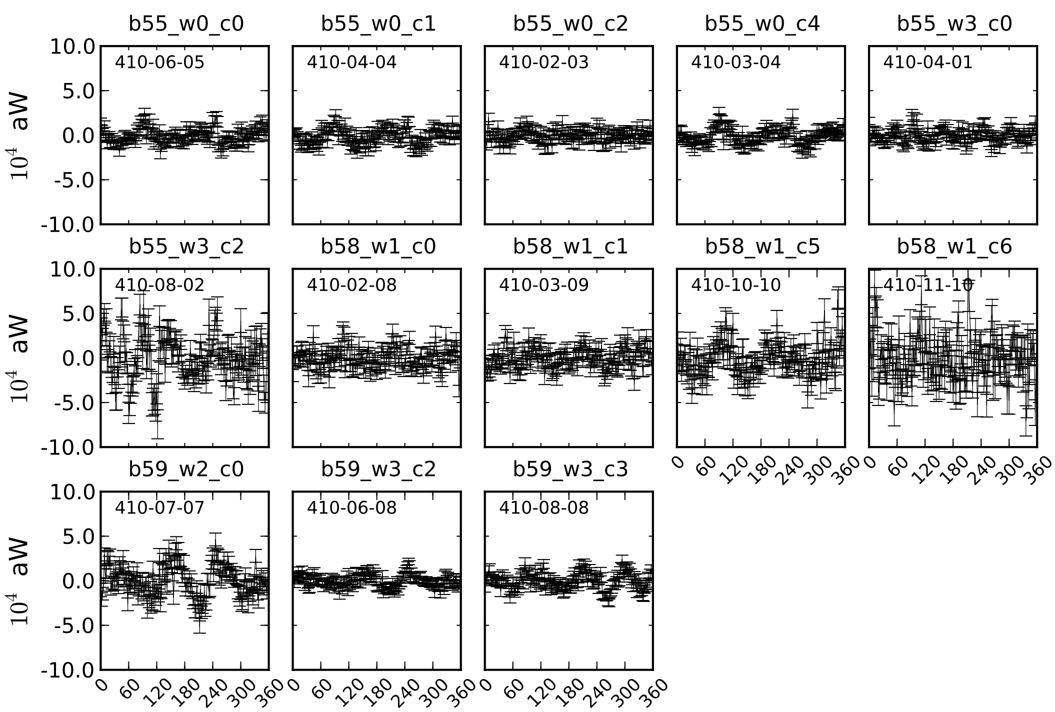

Figure 6.23: Selected data from the ok410 bolometer set, after subtraction of a 2 harmonic azimuth template.

By inspection of Fig. 6.16, we note that the selected 250 GHz bolometers are arranged fairly compactly on the 250 GHz wafer, and their pointings subtend only about 1° on the sky. By contrast, the selected detectors on the 410 GHz wafer are widely dispersed and will subtend approximately 2.2° on the sky. Since this is already similar to the 2° bin size we are using, we ignore this for now and use the boresight pointing for every detector. A more careful approach would calculate an individual pointing for each detector, but would complicate the co-addition procedure.

By assuming identical pointing for all bolometers, we can then perform all processing in the time domain as described in the preceeding sections, and as a final step we average the signals in time domain as well. In addition to this co-added mean, we compute the alternating, or "jacknifed" difference by adding the bolometer signals with alternating signs. That is, if we denote ${}_j\hat{d}_i$ to be the ith sample of the HWPSS subtracted and cleaned timestream of the jth bolometer, the signal common to all bolometers is estimated by

$$\begin{aligned} \langle s_i \rangle &= \frac{1}{N}\sum_j {}_j\hat{d}_i = \frac{1}{N}\sum_j \left[s_i +_j n_i\right] \\ &= s_i + \frac{1}{N}\sum_j {}_j n_i \end{aligned} \tag{6.13}$$

assuming that each bolometer has an independent noise ${}_j n_i$. Meanwhile the common signal is marginalized by

$$\begin{aligned} \langle 0 \rangle &= \frac{1}{N}\sum_j (-1)^j {}_j\hat{d}_i = \frac{1}{N}\sum_j (-1)^j \left[s_i +_j n_i\right] \\ &= 0 + \frac{1}{N}\sum_j (-1)^j_j n_i \end{aligned} \tag{6.14}$$

The result is presented in Figs. 6.24 and 6.25. In those plots, the top panel is the co-addition, and the next to top panel is the jacknife signal computed as above, both binned to 2° in azimuth and plotted as bin means μ_n with bin errors σ_n. The third panel down plots the ratio of bin errors between the co-add and jacknife, quantifying the intra-bin variance that is common between bolometers, and thus suppressed by the jacknife. The bottom panel plots μ_n/σ_n, the ratio between the bin mean and bin error in the co-add, as an estimate of the signal-to-noise ratio achieved.

For the ok250 bolometers, $\langle s_i \rangle$ exhibits a considerable degree of structure on $10-20°$ scales, a property that appears to hold true of the jacknife as well to a lesser extent. The ratio of bin errors takes a mean value of about 4, and the SNR ranges from < 0 to ~ 7.

The ok410 bolometers actually look significantly different, with lower SNR overall and a more noise-like jacknife, but also clear evidence of structure in the co-added signal.

Interestingly, the amplitudes in both cases are comparable to the expected power from the brightest dust emission bins ($\sim$ 2000 aW for 250 GHz, $\sim$ 20000 aW for 410 GHz), but neither co-add especially resembles the expected dust emission template.

6.7 Comparing Data to Simulation

At this point we can simulate noisy bolometer data using the sky flux models and use the pipeline established here to compare the results. With several simple additions, we construct a plausible realization of a bolometer timestream.

HEALPix makes it very easy to insert pointing offsets. Because of the nearest-neighbor packing of the pixelization algorithm, an offset in pixel number corresponds to a fairly predictable offset in angle for most pixels. Pixels on boundaries where this property does not hold make up a negligible fraction of the total. Therefore, to simulate the scatter of detectors across a wafer, for each realization we add one to the pixel number, which at $N_{side} = 512$ equates to a $\sim 6'$ step away from the boresight pointing.

According to models prepared by the EBEX collaboration, when all noise sources are taken into account we expect our detectors to perform with NET of $\sim 480\ \mu\mathrm{K}\sqrt{\mathrm{s}}$ at 250 GHz and $\sim 5900\ \mu\mathrm{K}\sqrt{\mathrm{s}}$ at 410 GHz. Using the conversions in Eq. 6.10 we obtain noise per sample (NPS)

$$\begin{aligned}
\mathrm{NPS}_{250} &= 480\sqrt{190.73}\ \mu\mathrm{K} \\
&= 3126\ \mathrm{aW} \\
\mathrm{NPS}_{410} &= 5900\sqrt{190.73}\ \mu\mathrm{K} \\
&= 7275\ \mathrm{aW}
\end{aligned} \tag{6.15}$$

and we likewise use those conversions to scale the flux model from MJy/sr to aW, before adding a Gaussian random signal with σ equal to the NPS above. We do not

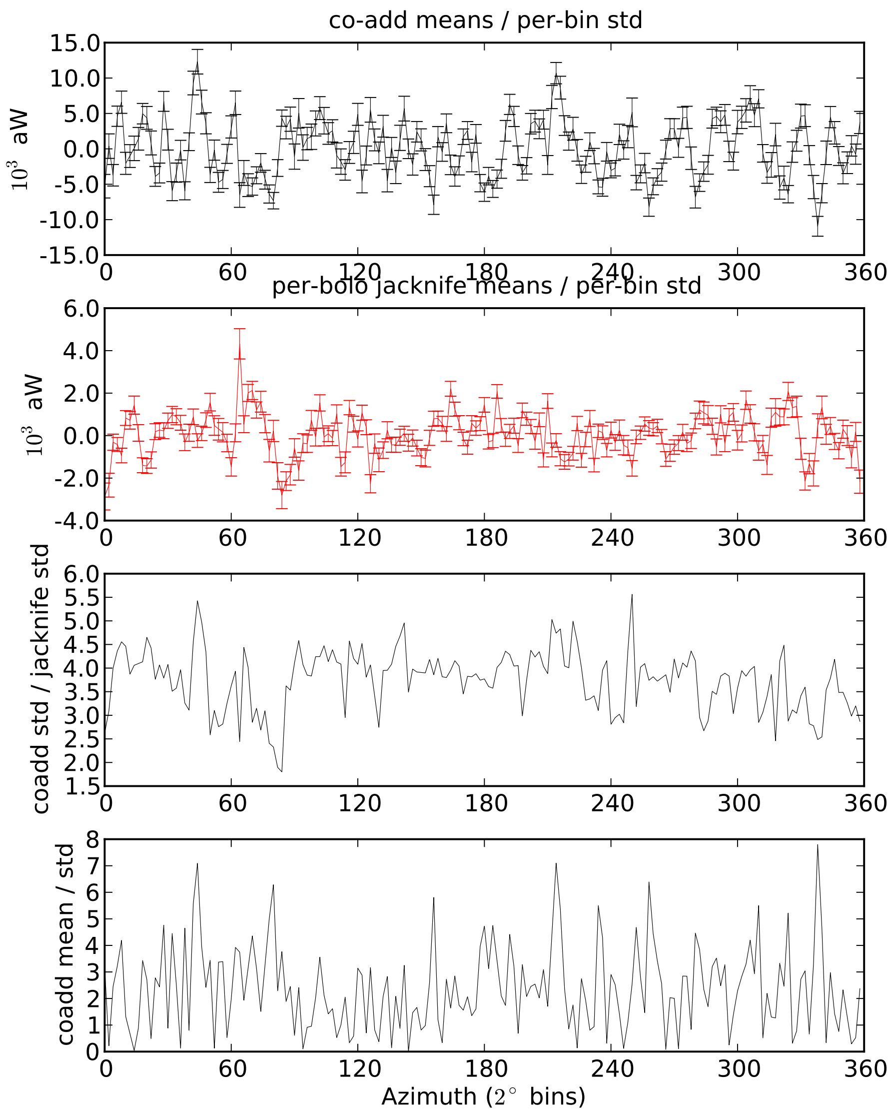

Figure 6.24: Co-add and diagnostics for ok250 azimuth template subtracted data. Bolometers b52_w3_c4, b56_w1_c7, b57_w0_c6, b57_w1_c7, and b57_w3_c6 are excluded due to large residual SSS post-subtraction, leaving 14 bolometers: 11 light and 3 dark. See Sec. 6.6 for details.

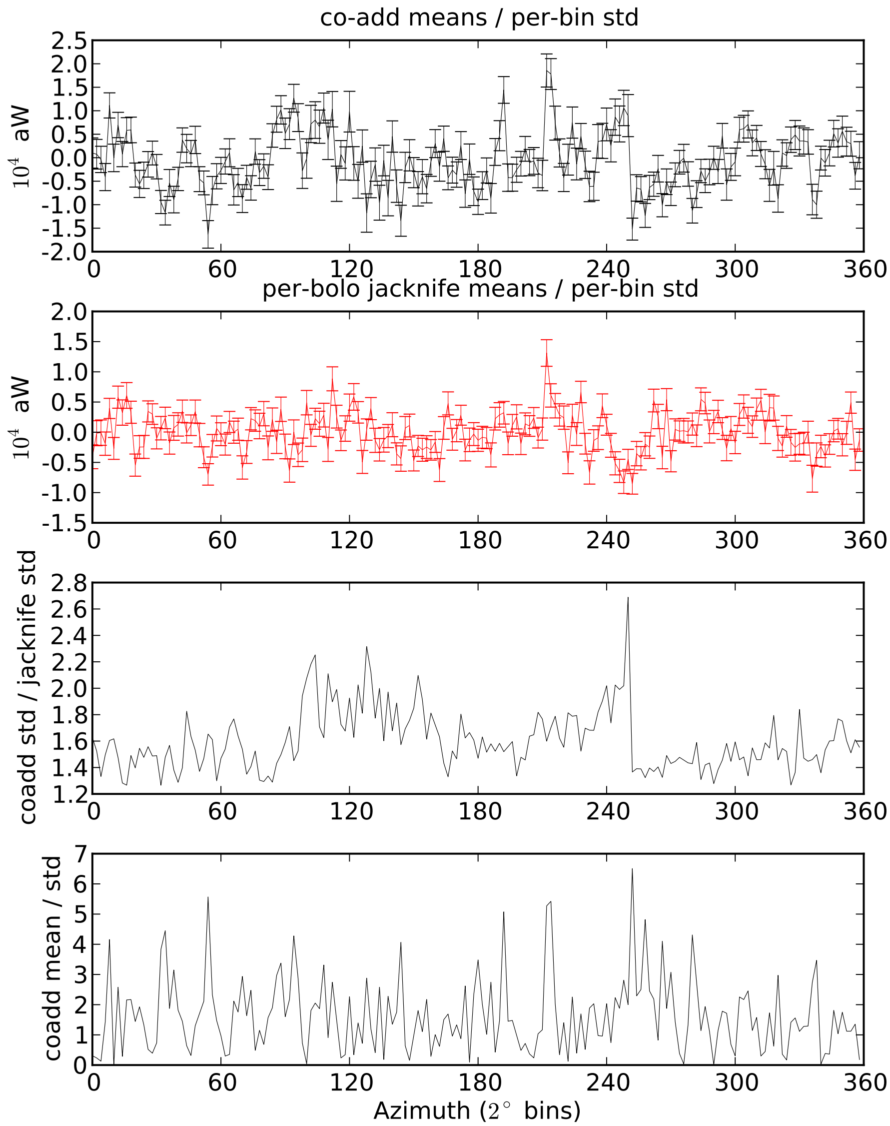

Figure 6.25: Co-add and diagnostics for ok410 azimuth template subtracted data. Bolometers b55_w3_c2, b58_w1_c5, and b59_w2_c0 are excluded due to large residual SSS post-subtraction, leaving 10 bolometers. See Sec. 6.6 for details.

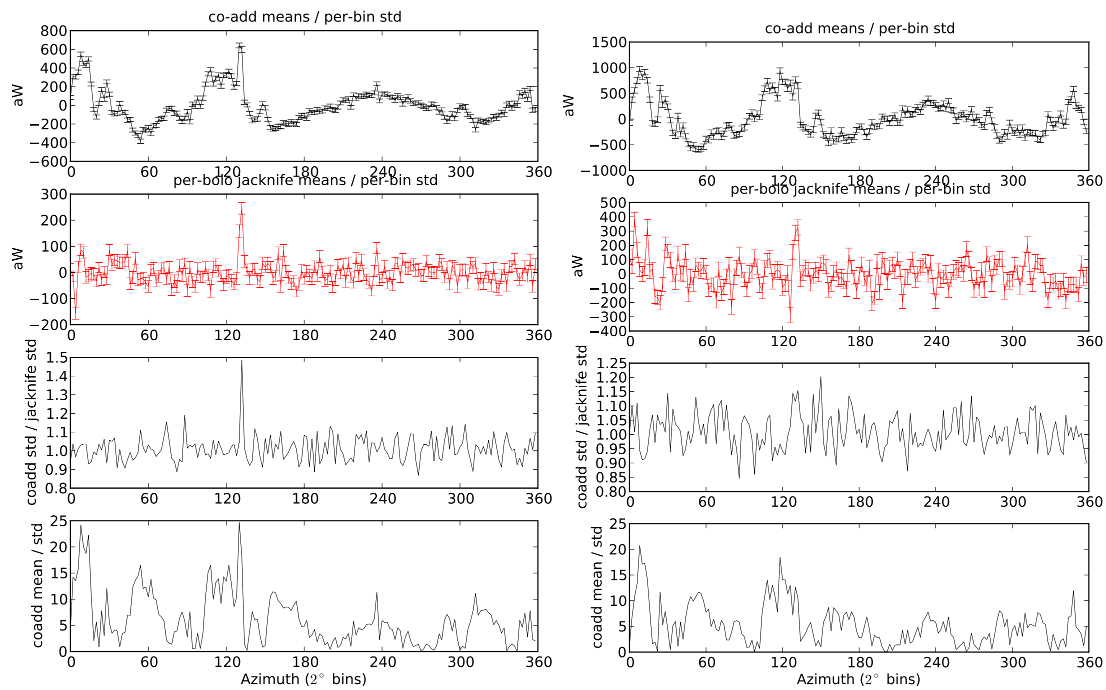

Figure 6.26: Co-add and jacknife plot for 14 simulated bolometers with independent noise and offset pointings: 250 GHz at left and 410 GHz at right. See Sec. 6.7 for details.

add transient glitches or line noise, so while the glitch and narrow line removers will run, we do not expect them to have an effect.

The outcome of doing so is plotted using the same co-add/jacknife plots in Fig. 6.26. For both 250 and 410 GHz, 14 bolometer timestream realizations, with offset pointing and independent noise, are generated, co-added, and differenced. We find that in the absence of a scan-synchronous signal the azimuth template removal has reduced the dust contrast modestly on large scales, but the dust model profile is otherwise quite recognizable. Each realization uses a different pointing chosen to approximate the distribution of selected bolometers on the 410 GHz wafer, spanning 2° in azimuth and 1.3° in elevation. The resulting difference in sky sampling is apparent in the difference plot, second panel from top, in regions of large contrast where the sky changes sharply from one bin to the next, such as near 130° azimuth.

Other than at high contrast bins, in both band simulations the jacknife panel is flat and quite noise-like, as expected since we have added no correlated noise to these

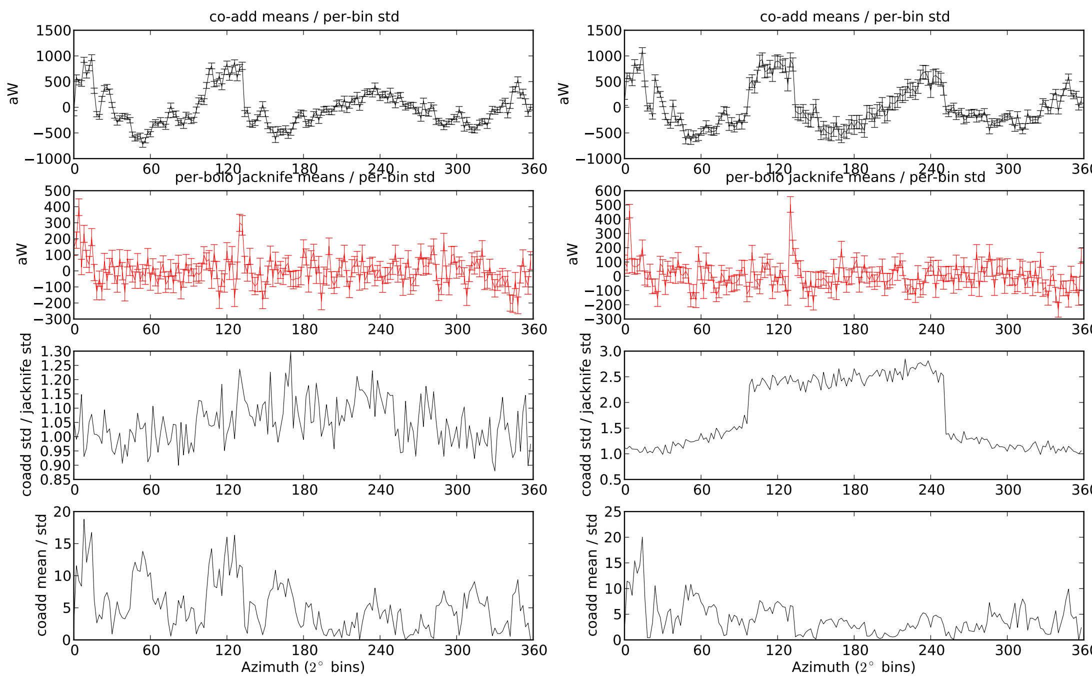

Figure 6.27: Simulations of 14 bolometers viewing the 410 GHz model sky including an artificial SSS which is then fit and removed by the pipeline. Left: a 10 MJy/sr fundamental SSS; Right: a 50 MJy/sr fundamental SSS and a 20 MJy/sr second harmonic of azimuth SSS.

realizations. Between the band-pass filter and the de facto smoothing accomplished by the pointing offsets, there is apparently very little intra-bin correlated structure, as the ratio of bin errors is close to unity. Based on the SNR panel, had the system performed as simulated here, there would have been a robust detection of dust emission.

Finally we add a simulated SSS to the model, as shown in Fig. 6.27. On the left hand side of that figure we use a single-term SSS with amplitude comparable to the large-scale dust contrast. On the right we use a more complex SSS which includes a larger fundamental mode, and also includes the second harmonic of azimuth. These modes are defined as:

$$\begin{aligned}\langle g_i \rangle_{simple} &= 10 \text{ MJy/sr} \cdot \cos(\alpha_i + 25^\circ) \\ \langle g_i \rangle_{complex} &= 50 \text{ MJy/sr} \cdot \cos(\alpha_i + 25^\circ) + \\ &\quad 20 \text{ MJy/sr} \cdot \cos(2\alpha_i + 155^\circ)\end{aligned} \tag{6.16}$$

That the co-added signals (top panels of Fig. 6.27) retain the same basic shape

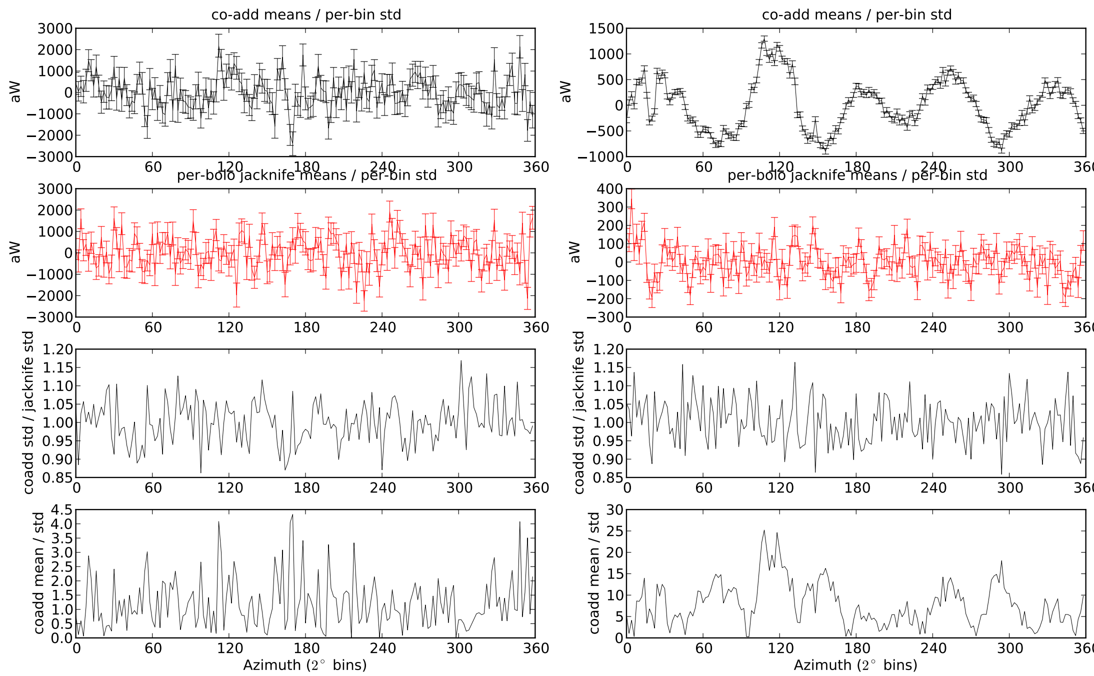

Figure 6.28: Variations on the simulations of 14 bolometers viewing the 410 GHz model sky. Left: NPS is increased by a factor of 10. Right: 1 MJy/sr SSS is the 5th harmonic of azimuth, which is not removed by the azimuth template subtractor.

indicates the effectiveness of the azimuth template removal step of the pipeline described above. However, the addition and removal of a very large SSS does produce alterations to the final data product, most apparent in the ratio of bin errors. Note that when only the second term of $\langle g_i \rangle_{complex}$ is added, the result closely resembles the left panel with the simpler SSS. By way of context, in Figs. 6.18 and 6.19 the characteristic SSS amplitudes at 250 GHz and 410 GHz are 2.5×10^4 aW and 1.0×10^5 aW, respectively. Using Eq. 6.10 we see that these correspond to estimated sky fluxes of 25 and 220 MJy/sr.

Several variations on this experiment are possible. Here are a few:

- Increasing the NPS by a factor of ten is sufficient to largely obscure the dust signal profile in the co-add, but does not produce correlated structures in the jacknife. See Fig. 6.28, left panel.

- An SSS component that is a greater than second harmonic of azimuth and is

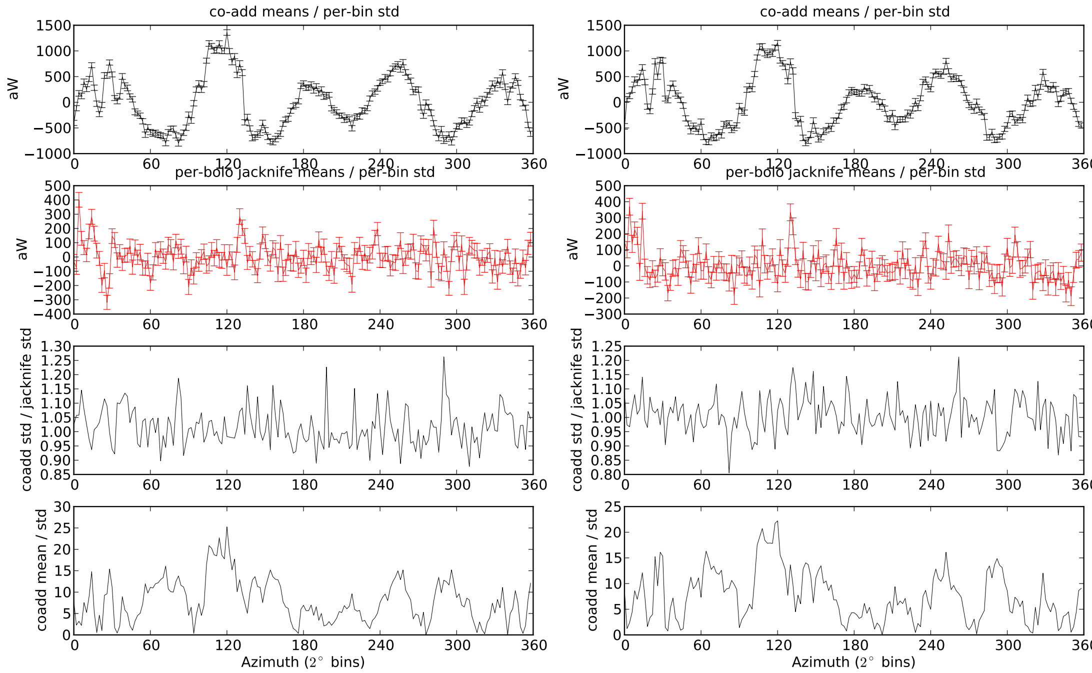

Figure 6.29: Variations on the simulations of 14 bolometers viewing the 410 GHz model sky. Left: the amplitude of the SSS varies between 0.25 and 2.25 MJy/sr. Right: the phase of the SSS varies between bolometers by up to 30°.

common to all bolometers does appear in the co-add, but does not affect the jacknife, regardless of amplitude. See Fig. 6.28, right panel.

- A SSS component which varies in phase from signal to signal or varies in amplitude with time will also appear in the co-add but will not significantly affect the jacknife. Provided the wavelength is longer than the bin size, the ratio of bin errors is unchanged. See Fig. 6.29.

- Creating a common-mode Gaussian white noise with magnitude equal to the nominal NPS is sufficient to both partly obscure the sky profile in the co-add and to increase the ratio of bin errors to about 4, but does not affect the jacknife. Increasing the NPS by a factor of 5 further obscures the sky profile, increases the jacknife variance, and reduces the ratio of bin errors and SNR. See Fig. 6.30.

For the sake of illustration, Fig. 6.31 shows the result of combining a large SSS, high

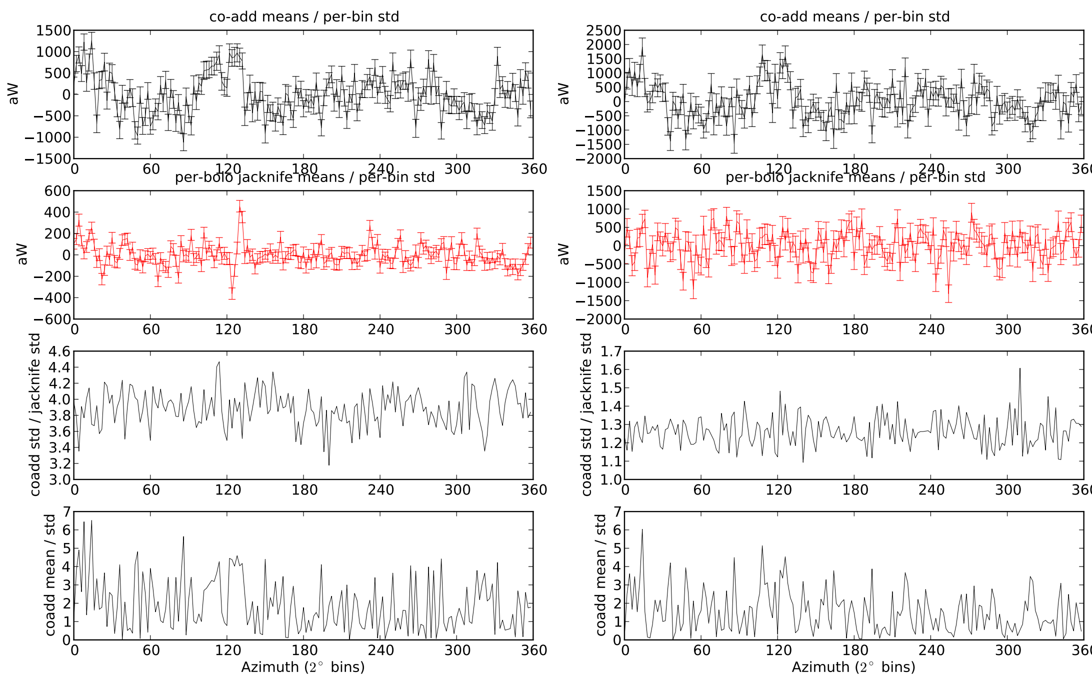

Figure 6.30: Simulations of 14 bolometers viewing the 410 GHz model sky with Gaussian random common-mode noise. Left: the common mode noise has amplitude equal to the nominal NPS. Right: same as left but the NPS is increased by a factor of 5.

noise, and a common-mode noise term. This combination comes closest to approximating the behavior of the real bolometer sets as seen in Figs. 6.24 and 6.25.

6.8 Conclusion

EBEX successfully executed a constant rotational speed scan near the end of the North American test flight intended to gather calibration data from the CMB dipole or galactic dust. After aggressive data cuts, we selected 563.7 seconds of data from 32 bolometers at two bands for analysis. By simulating the sky and observing scheme we can demonstrate that under nominal conditions EBEX should have robustly detected both signals.

In reality, the presence of large scan-synchronous signals, possibly in conjunction with common-mode noise, destroyed the possibility of detecting the CMB dipole. Even after further data processing to reduce unwanted noise and suppress some scan-synchronous

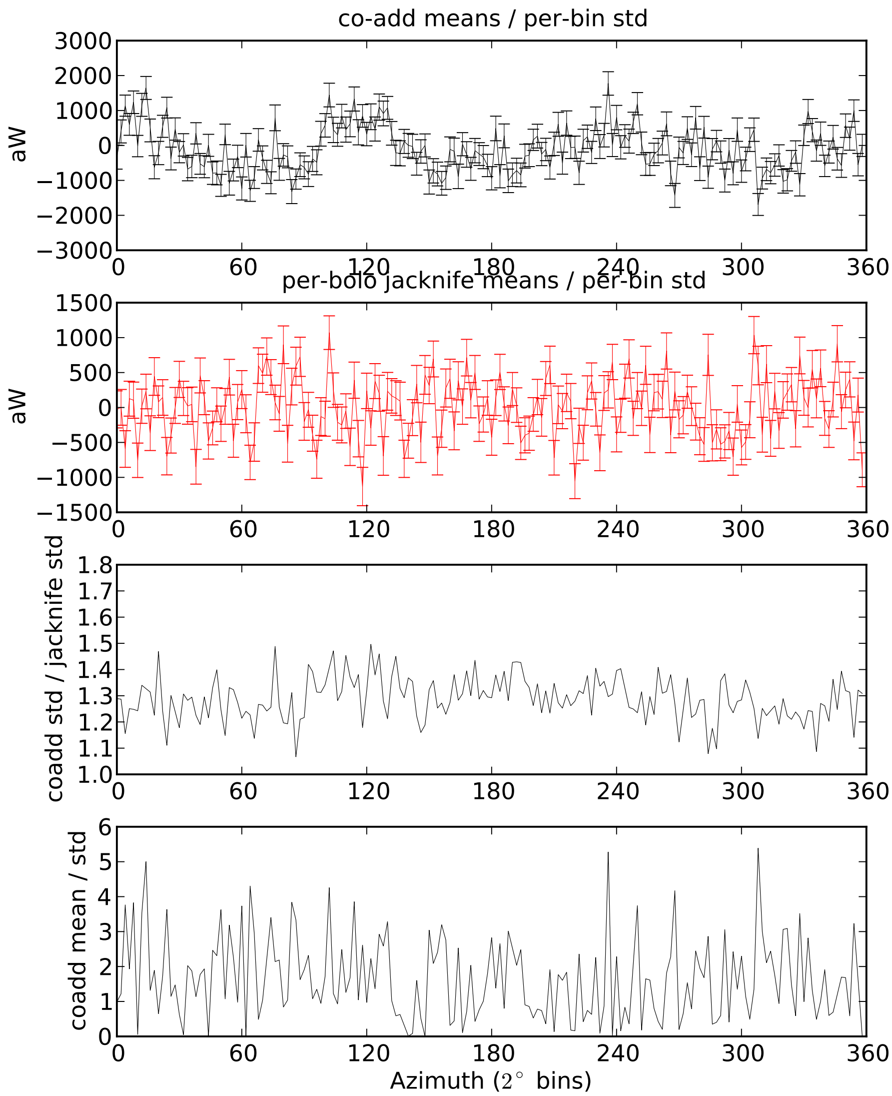

Figure 6.31: Simulation of 14 bolometers viewing the 410 GHz model sky with fundamental SSS of 50 MJy/sr, Gaussian random common-mode noise equal to the nominal NPS, and realized NPS increased by a factor of 5.

signals we are unable to claim an unambiguous detection of emission from an astronomical origin.

The sources of these spurious signals remain under investigation. Future work may include harnessing established techniques for detecting and characterizing noise that is correlated across signals. By doing so we may be able to decisively confirm the presence of a common-mode noise term, and possibly gain insight into its origin.

References

[1] H. Curtis. The scale of the universe. *Bull. Nat. Res. Coun.*, 2:194, May 1921.

[2] H. Shapley. The scale of the universe. *Bull. Nat. Res. Coun.*, 2:171, May 1921.

[3] A. A. Penzias and R. W. Wilson. A Measurement of Excess Antenna Temperature at 4080 Mc/s. ApJ, 142:419–421, July 1965.

[4] R. H. Dicke, P. J. E. Peebles, P. G. Roll, and D. T. Wilkinson. Cosmic Black-Body Radiation. ApJ, 142:414–419, July 1965.

[5] Paul Oxley, Peter A. Ade, C. Baccigalupi, Pierluigi deBernardis, Hsiao-Mei Cho, Mark J. Devlin, Shaul Hanany, B. R. Johnson, T. Jones, Adrian T. Lee, T. Matsumura, Amber D. Miller, M. Milligan, T. Renbarger, Helmuth G. Spieler, R. Stompor, Gregory S. Tucker, and Matias Zaldarriaga. The EBEX experiment. In Marija Strojnik, editor, *Infrared Spaceborne Remote Sensing XII*, volume 5543 of *Society of Photo-Optical Instrumentation Engineers (SPIE) Conference Series*, pages 320–331. SPIE, 2004.

[6] Will Grainger, Asad M. Aboobaker, Peter Ade, François Aubin, Carlo Baccigalupi, Éric Bissonnette, Julian Borrill, Matt Dobbs, Shaul Hanany, Clayton Hogen-Chin, Johannes Hubmayr, Andrew Jaffe, Bradley Johnson, Terry Jones, Jeff Klein, Andrei Korotkov, Sam Leach, Adrian Lee, Lorne Levinson, Michele Limon, John Macaluso, Kevin MacDermid, Tomotake Matsumura, Xiaofan Meng, Amber Miller, Michael Milligan, Enzo Pascale, Dan Polsgrove, Nicolas Ponthieu, Britt Reichborn-Kjennerud, Tom Renbarger, Ilan Sagiv, Federico Stivoli, Radek Stompor, Huan Tran, Greg Tucker, Jerry Vinokurov, Matias Zaldarriaga, and Kyle Zilic. EBEX:

the E and B Experiment. In William D. Duncan, Wayne S. Holland, Stafford Withington, and Jonas Zmuidzinas, editors, *Millimeter and Submillimeter Detectors and Instrumentation for Astronomy IV*, volume 7020 of *Society of Photo-Optical Instrumentation Engineers (SPIE) Conference Series*, page 70202N. SPIE, 2008.

[7] U. Seljak and M. Zaldarriaga. Signature of Gravity Waves in the Polarization of the Microwave Background. *Physical Review Letters*, 78:2054–2057, March 1997, arXiv:astro-ph/9609169.

[8] W. Hu, U. Seljak, M. White, and M. Zaldarriaga. Complete treatment of CMB anisotropies in a FRW universe. Phys. Rev. D, 57:3290–3301, March 1998, arXiv:astro-ph/9709066.

[9] W. N. Brandt, C. R. Lawrence, A. C. S. Readhead, J. N. Pakianathan, and T. M. Fiola. Separation of foreground radiation from cosmic microwave background anisotropy using multifrequency measurements. ApJ, 424:1–21, March 1994.

[10] C. Baccigalupi. Cosmic microwave background polarisation: foreground contrast and component separation. *New Astronomy Review*, 47:1127–1134, December 2003, arXiv:astro-ph/0306181.

[11] M. Zaldarriaga and U. Seljak. Gravitational lensing effect on cosmic microwave background polarization. Phys. Rev. D, 58(2):023003–+, July 1998, arXiv:astro-ph/9803150.

[12] Britt Reichborn-Kjennerud, Asad M. Aboobaker, Peter Ade, François Aubin, Carlo Baccigalupi, Chaoyun Bao, Julian Borrill, Christopher Cantalupo, Daniel Chapman, Joy Didier, Matt Dobbs, Julien Grain, William Grainger, Shaul Hanany, Seth Hillbrand, Johannes Hubmayr, Andrew Jaffe, Bradley Johnson, Terry Jones, Theodore Kisner, Jeff Klein, Andrei Korotkov, Sam Leach, Adrian Lee, Lorne Levinson, Michele Limon, Kevin MacDermid, Tomotake Matsumura, Xiaofan Meng, Amber Miller, Michael Milligan, Enzo Pascale, Daniel Polsgrove, Nicolas Ponthieu, Kate Raach, Ilan Sagiv, Graeme Smecher, Federico Stivoli, Radek Stompor, Huan Tran, Matthieu Tristram, Gregory S. Tucker, Yury Vinokurov, Amit Yadav, Matias Zaldarriaga, and Kyle Zilic. EBEX: a balloon-borne CMB polarization experiment. In Wayne S. Holland and Jonas Zmuidzinas, editors, *Millimeter,*

Submillimeter, and Far-Infrared Detectors and Instrumentation for Astronomy V, volume 7741 of *Society of Photo-Optical Instrumentation Engineers (SPIE) Conference Series*, page 77411C. SPIE, 2010, 1007.3672.

[13] Enzo Pascale et al. The Balloon-borne Large Aperture Submillimeter Telescope: BLAST. ApJ, 681:400–414, July 2008, 0711.3465.

[14] Donald Victor Wiebe. *BLAST: A Balloon-borne, Large-aperture, Submillimetre Telescope*. PhD thesis, University of Toronto, February 2009.

[15] Daniel E. Polsgrove. *Calibration of the E and B EXperiment (EBEX), A Balloon-Borne Cosmic Microwave Background Polarimeter*. PhD thesis, University of Minnesota, September 2009.

[16] Johannes Hubmayr. *Bolometric detectors for EBEX: a balloon-borne cosmic microwave background polarimeter*. PhD thesis, University of Minnesota, December 2009.

[17] Britt Reichborn-Kjennerud. *Building and Flying the E and B Experiment to Measure the Polarization of the Cosmic Microwave Background*. PhD thesis, Columbia University, 2010.

[18] Ilan S. Sagiv. *The EBEX cryostat and Supporting Electronics*. PhD thesis, University of Minnesota, March 2011.

[19] E. M. Leitch, J. M. Kovac, N. W. Halverson, J. E. Carlstrom, C. Pryke, and M. W. E. Smith. Degree Angular Scale Interferometer 3 Year Cosmic Microwave Background Polarization Results. ApJ, 624:10–20, May 2005, arXiv:astro-ph/0409357.

[20] T. E. Montroy, P. A. R. Ade, J. J. Bock, J. R. Bond, J. Borrill, A. Boscaleri, P. Cabella, C. R. Contaldi, B. P. Crill, P. de Bernardis, G. De Gasperis, A. de Oliveira-Costa, G. De Troia, G. di Stefano, E. Hivon, A. H. Jaffe, T. S. Kisner, W. C. Jones, A. E. Lange, S. Masi, P. D. Mauskopf, C. J. MacTavish, A. Melchiorri, P. Natoli, C. B. Netterfield, E. Pascale, F. Piacentini, D. Pogosyan, G. Polenta, S. Prunet, S. Ricciardi, G. Romeo, J. E. Ruhl, P. Santini, M. Tegmark, M. Veneziani, and

N. Vittorio. A Measurement of the CMB EE Spectrum from the 2003 Flight of BOOMERANG. ApJ, 647:813–822, August 2006, arXiv:astro-ph/0507514.

[21] S. Hanany, J. Hubmayr, B. R. Johnson, T. Matsumura, P. Oxley, and M. Thibodeau. Millimeter-wave achromatic half-wave plate. Appl. Opt., 44:4666–4670, August 2005, arXiv:physics/0503122.

[22] John R Hull, Shaul Hanany, Tomotake Matsumura, Bradley Johnson, and Terry Jones. Characterization of a high-temperature superconducting bearing for use in a cosmic microwave background polarimeter. *Superconductor Science and Technology*, 18(2):S1, 2005.

[23] Bradley R. Johnson. *MAXIPOL: A bolometric, balloon-borne experiment for measuring the polarization anisotropy of the cosmic microwave background radiation.* PhD thesis, University of Minnesota, 2004.

[24] M. Dobbs, E. Bissonnette, and H. Spieler. Digital Frequency Domain Multiplexer for Millimeter-Wavelength Telescopes. *IEEE Transactions on Nuclear Science*, 55:21–26, 2008, 0708.2762.

[25] I. Sagiv, A. M. Aboobaker, C. Bao, S. Hanany, T. Jones, J. Klein, M. Milligan, D. E. Polsgrove, K. Raach, K. Zilic, A. Korotkov, G. S. Tucker, Y. Vinukurov, T. Matsumura, P. Ade, W. Grainger, E. Pascale, D. Chapman, J. Didier, S. Hillbrand, B. Reichborn-Kjennerud, M. Limon, A. Miller, A. Jaffe, A. Yadav, M. Zaldarriaga, N. Ponthieu, M. Tristram, J. Borrill, C. Cantalupo, T. Kisner, F. Aubin, M. Dobbs, K. MacDermid, G. Hilton, J. Hubmayr, K. Irwin, C. Reintsema, C. Baccigalupi, S. Leach, B. Johnson, A. Lee, H. Tran, and L. Levinson. The EBEX cryostat and supporting electronics. In Thibault Damour, Robert T Jantzen, and Remo Ruffini, editors, *Proceedings of the Twelfth Marcel Grossmann Meeting on General Relativity.* World Scientific, 2010, arXiv:1005.3339v1 [astro-ph.IM].

[26] Johannes Hubmayr, François Aubin, Eric Bissonnette, Matt Dobbs, Shaul Hanany, Adrian T. Lee, Kevin MacDermid, Xiaofan Meng, Ilan Sagiv, and Graeme Smecher. Design and characterization of TES bolometers and SQUID readout electronics for a balloon-borne application. In William D. Duncan, Wayne S. Holland, Stafford

Withington, and Jonas Zmuidzinas, editors, *Millimeter and Submillimeter Detectors and Instrumentation for Astronomy IV*, volume 7020 of *Society of Photo-Optical Instrumentation Engineers (SPIE) Conference Series*, page 70200J. SPIE, 2008.

[27] François Aubin, Asad M. Aboobaker, Peter Ade, Carlo Baccigalupi, Chaoyun Bao, Julian Borrill, Christopher Cantalupo, Daniel Chapman, Joy Didier, Matt Dobbs, Will Grainger, Shaul Hanany, Johannes Hubmayr, Peter Hyland, Seth Hillbrand, Andrew Jaffe, Bradley Johnson, Terry Jones, Theodore Kisner, Jeff Klein, Andrei Korotkov, Sam Leach, Adrian Lee, Michele Limon, Kevin MacDermid, Tomotake Matsumura, Xiaofan Meng, Amber Miller, Michael Milligan, Daniel Polsgrove, Nicolas Ponthieu, Kate Raach, Britt Reichborn-Kjennerud, Ilan Sagiv, Graeme Smecher, Huan Tran, Gregory S. Tucker, Yury Vinokurov, Amit Yadav, Matias Zaldarriaga, and Kyle Zilic. First implementation of TES bolometer arrays with SQUID-based multiplexed readout on a balloon-borne platform. In Wayne S. Holland and Jonas Zmuidzinas, editors, *Millimeter, Submillimeter, and Far-Infrared Detectors and Instrumentation for Astronomy V*, volume 7741 of *Society of Photo-Optical Instrumentation Engineers (SPIE) Conference Series*, page 77411T. SPIE, 2010.

[28] Seth Hillbrand et al. unpublished internal EBEX communication.

[29] C. Barnes, R. S. Hill, G. Hinshaw, L. Page, C. L. Bennett, M. Halpern, N. Jarosik, A. Kogut, M. Limon, S. S. Meyer, G. S. Tucker, E. Wollack, and E. L. Wright. First-Year Wilkinson Microwave Anisotropy Probe (WMAP) Observations: Galactic Signal Contamination from Sidelobe Pickup. ApJS, 148:51–62, September 2003, arXiv:astro-ph/0302215.

[30] A. Benoît, P. Ade, A. Amblard, R. Ansari, E. Aubourg, J. Bartlett, J.-P. Bernard, R. S. Bhatia, A. Blanchard, J. J. Bock, A. Boscaleri, F. R. Bouchet, A. Bourrachot, P. Camus, F. Couchot, P. de Bernardis, J. Delabrouille, F.-X. Désert, O. Doré, M. Douspis, L. Dumoulin, X. Dupac, P. Filliatre, K. Ganga, F. Gannaway, B. Gautier, M. Giard, Y. Giraud-Héraud, R. Gispert, L. Guglielmi, J.-C. Hamilton, S. Hanany, S. Henrot-Versillé, V. V. Hristov, J. Kaplan, G. Lagache, J.-M. Lamarre,

A. E. Lange, K. Madet, B. Maffei, D. Marrone, S. Masi, J. A. Murphy, F. Naraghi, F. Nati, G. Perrin, M. Piat, J.-L. Puget, D. Santos, R. V. Sudiwala, J.-C. Vanel, D. Vibert, E. Wakui, and D. Yvon. Archeops: a high resolution, large sky coverage balloon experiment for mapping cosmic microwave background anisotropies. *Astroparticle Physics*, 17:101–124, May 2002, arXiv:astro-ph/0106152.

[31] C. Dragone and D. C. Hogg. The radiation pattern and impedance of offset and symmetrical near-field Cassegrainian and Gregorian antennas. *IEEE Transactions on Antennas and Propagation*, 22:472–475, 1974.

[32] H. Tran, A. Lee, S. Hanany, M. Milligan, and T. Renbarger. Comparison of the crossed and the Gregorian Mizuguchi-Dragone for wide-field millimeter-wave astronomy. Appl. Opt., 47:103–109, January 2008.

[33] W. Wong. On the equivalent parabola technique to predict the performance characteristics of a Cassegrainian system with an offset feed. *IEEE Transactions on Antennas and Propagation*, 21:335–339, May 1973.

[34] Y. Mizuguchi, M. Akagawa, and H. Yokoi. Offset Gregorian antenna. *Electronics Communications of Japan*, 61:58–66, March 1978.

[35] C. Dragone. A first-order treatment of aberrations in Cassegrainian and Gregorian antennas. *IEEE Transactions on Antennas and Propagation*, 30:331–339, May 1982.

[36] Radiant ZEMAX LLC, http://zemax.com. *ZEMAX: Software for Optical System Design.*

[37] Optical Research Associates, http://opticalres.com. *CODE V.*

[38] M. J. Griffin, J. J. Bock, and W. K. Gear. Relative performance of filled and feedhorn-coupled focal-plane architectures. Appl. Opt., 41:6543–6554, November 2002, arXiv:astro-ph/0205264.

[39] TICRA, http://ticra.dk. *GRASP8 General reflector and antenna farm analysis software.*

[40] B. Gold, C. L. Bennett, R. S. Hill, G. Hinshaw, N. Odegard, L. Page, D. N. Spergel, J. L. Weiland, J. Dunkley, M. Halpern, N. Jarosik, A. Kogut, E. Komatsu, D. Larson, S. S. Meyer, M. R. Nolta, E. Wollack, and E. L. Wright. Five-Year Wilkinson Microwave Anisotropy Probe Observations: Galactic Foreground Emission. ApJS, 180:265–282, February 2009, 0803.0715.

[41] Eugene Hecht. *Optics*. Addison-Wesley Publishing Co., Boston, MA, USA, 2nd edition, 1987.

[42] Simon Chase. *Two-stage sub-Kelvin ^{3}He cooler*. Chase Research Cryogenics Ltd., 140 Manchester Road, Sheffield S10 5DL, England.

[43] NASA Columbia Scientific Balloon Facility. *LDB Science Enclosures*, 2010.

[44] H. Boterenbrood and B. Hallgren. The development of the Embedded Local Monitor Board (ELMB). In *PROCEEDINGS of the Ninth Workshop on Electronics for LHC Experiments*, 9th Workshop on Electronics for LHC Experiments, pages 331–334, 2003.

[45] H. Boterenbrood, H. J. Burckhart, J. Cook, V. Filimonov, B. Hallgren, W. Heubers, V. Khomoutnikov, Y. Ryabov, and F. Varela. Design and Implementation of the ATLAS Detector Control System. *IEEE Transactions on Nuclear Science*, 51:495–501, June 2004.

[46] H. Boterenbrood, H.J. Burckhart, and H. Kvedalen. The Embedded Local Monitor Board (ELMB) in the LHC front-end I/O control system. In *PROCEEDINGS of the Seventh Workshop on Electronics for LHC Experiments*, 7th Workshop on Electronics for LHC Experiments, pages 325–330, 2001.

[47] Sixnet LLC, http://sixnet.com. *EtherTRAK Industrial Ethernet Real-Time Ring switch*. various models.

[48] ISO 11898-1:2003. *Road vehicles – Controller area network (CAN) – Part 1: Data link layer and physical signalling*. International Organization for Standardization, Geneva, Switzerland, 2003.

[49] Kvaser Inc., http://www.kvaserinc.com. *Leaf SemiPro HS*.

[50] Ampro ADLINK Technology, Inc., http://ampro.com. *MightyBoard 800*.

[51] Debian Project, http://debian.org. *Debian GNU/Linux Operating System*, 4.0 ("etch") edition.

[52] D. Robinson and K. Coar. The Common Gateway Interface (CGI) Version 1.1. RFC 3875 (Informational), October 2004.

[53] D. Crockford. The application/json Media Type for JavaScript Object Notation (JSON). RFC 4627 (Informational), July 2006.

[54] Guido van Rossum et al. *Python Language Reference*. http://www.python.org/.

[55] J. Postel. User Datagram Protocol. RFC 768 (Standard), August 1980.

[56] S. Hopkins and B. Coile. *ATA over Ethernet Specification*. The Brantley Coile Company, Inc., February 2009.

[57] CORAID Inc., http://www.coraid.com. *EtherDrive storage solutions*.

[58] Donald Victor Wiebe. *Dirfile Standards*. http://getdata.sourceforge.net.

[59] Barth Netterfield et al. *KST*. KDE Project, http://kst.kde.org/.

[60] The World Wide Web Consortium (W3C), http://www.w3.org/TR/html5/. *HTML5: A vocabulary and associated APIs for HTML and XHTML*.

[61] Jeffrey M. Klein et al. Cryogenic half-wave plate polarimeter using a superconducting magnetic bearing. In *Cryogenic Optical Systems and Instruments XIV*, volume 8150 of *Society of Photo-Optical Instrumentation Engineers (SPIE) Conference Series*. SPIE, 2011. In preparation.

[62] K. M. Górski, E. Hivon, A. J. Banday, B. D. Wandelt, F. K. Hansen, M. Reinecke, and M. Bartelmann. HEALPix: A Framework for High-Resolution Discretization and Fast Analysis of Data Distributed on the Sphere. ApJ, 622:759–771, April 2005, arXiv:astro-ph/0409513.

[63] Cyrille Rosset et al. *healpy*. http://code.google.com/p/healpy/.

[64] A. J. Banday, K. M. Gorski, C. L. Bennett, G. Hinshaw, A. Kogut, C. Lineweaver, G. F. Smoot, and L. Tenorio. Root Mean Square Anisotropy in the COBE DMR Four-Year Sky Maps. ApJ, 475:393–+, February 1997, arXiv:astro-ph/9601065.

[65] D. J. Fixsen, E. S. Cheng, J. M. Gales, J. C. Mather, R. A. Shafer, and E. L. Wright. The Cosmic Microwave Background Spectrum from the Full COBE FIRAS Data Set. ApJ, 473:576–+, December 1996, arXiv:astro-ph/9605054.

[66] A. Kogut, C. Lineweaver, G. F. Smoot, C. L. Bennett, A. Banday, N. W. Boggess, E. S. Cheng, G. de Amici, D. J. Fixsen, G. Hinshaw, P. D. Jackson, M. Janssen, P. Keegstra, K. Loewenstein, P. Lubin, J. C. Mather, L. Tenorio, R. Weiss, D. T. Wilkinson, and E. L. Wright. Dipole Anisotropy in the COBE Differential Microwave Radiometers First-Year Sky Maps. ApJ, 419:1–+, December 1993, arXiv:astro-ph/9312056.

[67] C. H. Lineweaver. The CMB dipole: the most recent measurement and some history. In F. R. Bouchet, R. Gispert, B. Guiderdoni, & J. Trân Thanh Vân , editor, *16th Moriond Astrophysics Meeting: Microwave Background Anisotropies*, pages 69–75, 1997, arXiv:astro-ph/9609034.

[68] D. J. Schlegel, D. P. Finkbeiner, and M. Davis. Maps of Dust Infrared Emission for Use in Estimation of Reddening and Cosmic Microwave Background Radiation Foregrounds. ApJ, 500:525–+, June 1998, arXiv:astro-ph/9710327.

[69] D. P. Finkbeiner, M. Davis, and D. J. Schlegel. Extrapolation of Galactic Dust Emission at 100 Microns to Cosmic Microwave Background Radiation Frequencies Using FIRAS. ApJ, 524:867–886, October 1999, arXiv:astro-ph/9905128.

[70] M. Lombardi, C. J. Lada, and J. Alves. 2MASS wide field extinction maps. II. The Ophiuchus and the Lupus cloud complexes. A&A, 489:143–156, October 2008, 0809.3740.

[71] B. A. Wilking, M. Gagné, and L. E. Allen. Star Formation in the ρ Ophiuchi Molecular Cloud. In Reipurth, B., editor, *Handbook of Star Forming Regions, Volume II*, pages 351–+. Astronomical Society of the Pacific Monograph Publications, December 2008, arXiv:0811.0005v1 [astro-ph].

[72] F. Motte, P. Andre, and R. Neri. The initial conditions of star formation in the rho Ophiuchi main cloud: wide-field millimeter continuum mapping. A&A, 336:150–172, August 1998.

[73] C. D. Wilson, L. W. Avery, M. Fich, D. Johnstone, G. Joncas, L. B. G. Knee, H. E. Matthews, G. F. Mitchell, G. H. Moriarty-Schieven, and R. E. Pudritz. Submillimeter Continuum Emission in the rho Ophiuchi Molecular Cloud: Filaments, Arcs, and an Unidentified Far-Infrared Object. ApJ, 513:L139–L142, March 1999, arXiv:astro-ph/9901133.

[74] D. Johnstone, C. D. Wilson, G. Moriarty-Schieven, G. Joncas, G. Smith, E. Gregersen, and M. Fich. Large-Area Mapping at 850 Microns. II. Analysis of the Clump Distribution in the ρ Ophiuchi Molecular Cloud. ApJ, 545:327–339, December 2000.

[75] Peter Duffett-Smith. *Practical Astronomy with your Calculator*. Cambridge University Press, 3rd edition, 1988.

[76] M. Galassi, J. Davies, J. Theiler, B. Gough, G. Jungman, P. Alken, M. Booth, and F. Rossi. *GNU Scientific Library Reference Manual*. Network Theory Ltd, 3rd edition, 2009, http://www.gnu.org/software/gsl/.

[77] David L. Mills. On the accuracy and stablility of clocks synchronized by the network time protocol in the internet system. *SIGCOMM Comput. Commun. Rev.*, 20:65–75, December 1989.

[78] Michael Milligan, Peter Ade, François Aubin, Carlo Baccigalupi, Chaoyun Bao, Julian Borrill, Christopher Cantalupo, Daniel Chapman, Joy Didier, Matt Dobbs, Will Grainger, Shaul Hanany, Seth Hillbrand, Johannes Hubmayr, Peter Hyland, Andrew Jaffe, Bradley Johnson, Theodore Kisner, Jeff Klein, Andrei Korotkov, Sam Leach, Adrian Lee, Lorne Levinson, Michele Limon, Kevin MacDermid, Tomotake Matsumura, Amber Miller, Enzo Pascale, Daniel Polsgrove, Nicolas Ponthieu, Kate Raach, Britt Reichborn-Kjennerud, Ilan Sagiv, Huan Tran, Gregory S. Tucker, Yury Vinokurov, Amit Yadav, Matias Zaldarriaga, and Kyle Zilic. Software systems for operation, control, and monitoring of the EBEX instrument. In Nicole M.

Radziwill and Alan Bridger, editors, *Software and Cyberinfrastructure for Astronomy*, volume 7740 of *Society of Photo-Optical Instrumentation Engineers (SPIE) Conference Series*, page 774007. SPIE, 2010, arXiv:1006.5256v2 [astro-ph.IM].

[79] William H. Press, Saul A. Teukolsky, William T. Vetterling, and Brian P. Flannery. *Numerical recipes in C (2nd ed.): the art of scientific computing*. Cambridge University Press, New York, NY, USA, 1992.

[80] Travis E. Oliphant. *Guide to NumPy*. Trelgol Publishing, 2008, http://numpy.scipy.org/numpybook.pdf.

[81] Peter D Welch. The use of fast fourier transform for the estimation of power spectra: A method based on time averaging over short, modified periodograms. *IEEE Transactions on Audio and Electroacoustics*, 15(2):70–73, 1967.

Appendix A

Correlation of EBEX and DGPS Time via E-bus Frame Timestamps

A.1 Overview

There are several timing systems and timebases within the EBEX payload.

The cannonical timestamp attached to all logged data is the EBEX timestamp, generated by the time server boards. This timestamp is a 48 bit integer which increments at 100 kHz, and is expected to be highly stable. Each time server board is driven by an oven-controlled oscillator with 0.2 ppb stability. Not all 48 bits are attached to every data stream. EBEX time refers to the real-valued continuous flow of time measured by ticks of the EBEX timestamp. Additional details about the timing system are provided by Sagiv[25] and Reichborn-Kjennerud[17].

Reference to external world time is primarily provided by the DGPS system. By locking onto signals from the GPS satellite constellation, the DGPS contains an extremely precise representation of UTC world time. This representation is communicated to the timing system by two routes. The absolute time is written to a serial port at the flight computer once per second, with integer second resolution. This is accomplished with low precision, due to the communication latency inherent in the low speed serial protocol. Once per second, the DGPS also sends a heartbeat signal, which corresponds with high precision to the tick at the start of each new second. This heartbeat should be distributed to the timing system, which should broadcast via CANbus message the EBEX timestamp corresponding to the heartbeat.

The flight computers also contain internal real time clocks (RTC) that track world time. These clocks can be quite accurate if frequency governing and drift discipline are applied, such as by the NTP program. However, when allowed to free run, computer RTCs have notoriously poor stability[77].

In normal operation the heartbeat timestamp messages combined with the low resolution absolute time messages would be sufficient to correlate EBEX timestamps to external world time to 10 μs accuracy, far better than the 1 ms accuracy needed to meet EBEX's science objectives. However, during the North American test flight (NAF) the heartbeat messages were not logged, and therefore an alternate correlation strategy is needed.

A.2 E-bus frames

The E-bus subsystem of EBEX generates frames at 100.16 Hz, within which channels may be sampled either in every frame (fast channels) or in every 20th frame (slow channels). This frame is the only logged data structure in which both the EBEX timestamp and information about world time are recorded. More information on the frame generation subsystem can be found in Milligan et al[78].

In every frame (i.e. at 100.16 Hz) the EBEX timestamp is recorded with full 48 bit precision. This timestamp is generated in the ACS crate by a clock that is synchronized to the time server boards. By the architecture of the ACS crate and the flight control program, the value of the timestamp is sampled at the same time a start-of-frame signal is sent to the flight computers, ensuring that all values in a given frame are sampled synchronously to within microseconds. In typical operation the code path that performs the actual sample collection runs in about 50 μs, while reading values from the CANbus or serial ports occurs asynchronously in different threads.

The slow channels are all sampled at the start of a superframe block of 20 frames at 5.008 Hz, and thus are synchronous with the EBEX timestamp recorded in the first frame of the corresponding superframe. Of particular interest, the DGPS absolute time is logged as a slow channel.

A.3 Problem Definition

Ultimately we wish to obtain the function

$$t_{UTC} = f\left(t_{EBEX}\right) \tag{A.1}$$

where t_{EBEX} and t_{UTC} are EBEX and world UTC time, respectively. t_{DGPS} refers to UTC time truncated to one second resolution, which is the value reported to the flight computer by the DGPS system. Because the 100 kHz EBEX timestamp counter is by far the highest resolution representation of time used by the EBEX timing system, we do not distinguish here between the discrete EBEX timestamps and the logically continuous flow of EBEX time. Although t_{EBEX} is formally a 48 bit integer, we often scale this integer by 10^{-5} so that it has units of seconds, and will continue to do so here.

Both UTC world time and the EBEX time server clocks are characterized by good rate stability over the timescale of a balloon flight. Therefore we can approximate Eq. A.1 with a linear function

$$t_{UTC} = R \cdot t_{EBEX} + \Delta_{EBEX} \tag{A.2}$$

where R should be close to unity and Δ_{EBEX} has units of seconds. Numerically, at the start of the NAF t_{EBEX} = 99126103115 ticks = 991261.03115 seconds, and t_{DGPS} = 1244728901 seconds, referenced from the UNIX epoch. Thus we can already say that $\Delta_{EBEX} \approx 1243737640$ seconds.

Because the absolute DGPS time is logged at 5.008 Hz, we know with certainty into which UTC second each slow frame falls. Consider only DGPS timestamps which differ (always by +1) from the timestamp in the preceeding frame. That is, select the timestamps $t_{DGPS}\left[i\right]$ for all frame indices in the set

$$D = \left\{i \in \mathbb{Z} \mid \exists t_{DGPS}\left[i\right] \wedge \exists t_{DGPS}\left[i-20\right] \wedge t_{DGPS}\left[i\right] - t_{DGPS}\left[i-20\right] = 1\right\}$$

where $t_{DGPS}\left[i\right]$ is the DGPS timestamp recorded in the i^{th} fast frame, recognizing the fact that such a timestamp is only recorded in every 20th fast frame. Regardless of how these values are laid out in an on-disk data structure, this frame is always considered to be synchronous with the first frame of a superframe.

A.4 Statistical Solution

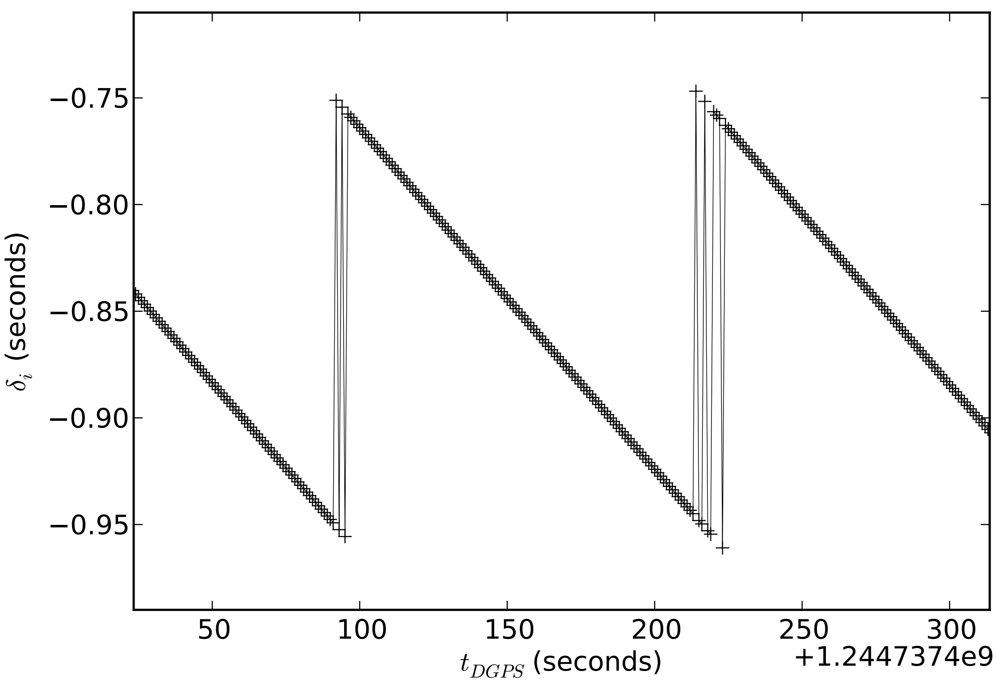

Figure A.1: $\delta_i$for estimated $\Delta_{EBEX} = 1243737640$ s. The predicted 125 s periodicity of δ_i is apparent in this ∼300 second segment from the NAF. The vertical lines at the end of each ramp correspond to the value of δ_i flip-flopping by 0.2 s as the second tick starts to fall very close to the frame generation time, and thus is updated either shortly before or shortly after the frame channels are sampled.

Call the EBEX timestamp in the i^{th} frame $t_{EBEX}[i]$. For $i \in D$, $t_{EBEX}[i]$ is an EBEX time that occurred between 0 and $\delta_f = \frac{1000}{5.008 \text{ Hz}} = 199.68$ ms after the world UTC integer second $t_{DGPS}[i]$. Call this unknown offset δ_i. Then

$$\delta_i = f\left(t_{EBEX}[i]\right) - t_{DGPS}[i] \approx R \cdot t_{EBEX}[i] + \Delta_{EBEX} - t_{DGPS}[i] \tag{A.3}$$

Since δ_f does not evenly divide 1 second, δ_i will vary with a period of (Least Common

Multiple) LCM $(\delta_f, 1000 \text{ ms}) = 125$ seconds, clearly visible in Fig. A.1. The frames logged during the NAF span 48100 seconds, almost 385 periods of the variation in δ_i, each period containing 125 values. As this distribution proceeds directly from linear modular arithmatic, we can consider $\delta_i$to be uniformly distributed over the range of possible values. Therefore, if R and Δ_{EBEX} are correctly chosen, the above calculation will yield $\langle \delta_i - \delta_f/2 \rangle = 0$ and $\delta_i$will have zero average slope.

This suggests that we can use the method of least squares linear regression to obtain the maximum likelihood values of R and Δ_{EBEX}. The sequence $[\delta_i - \delta_f/2]$ will be fit by the line $y = 0$, so we can take the expectation values of Eq. A.3 and rearrange to obtain

$$\begin{aligned} \langle \delta_i - \delta_f/2 \rangle = 0 &= \langle R \cdot t_{EBEX}[i] + \Delta_{EBEX} - t_{DGPS}[i] - \delta_f/2 \rangle \\ \langle t_{DGPS}[i] + \delta_f/2 \rangle &= \langle R \cdot t_{EBEX}[i] + \Delta_{EBEX} \rangle \end{aligned} \tag{A.4}$$

and apply regression to obtain $\Delta_{EBEX}$and R as the solution coefficients. This procedure produces values consistent with our expectations,

$$\begin{aligned} R &= 1 - 7.95 \times 10^{-9} \\ \Delta_{EBEX} &= 1243737640.9675536 \text{ s} \end{aligned} \tag{A.5}$$

A.5 Robustness

Regressions with coefficients of very different magnitudes are frequently error-prone (although less so than for nonlinear fitting, which is explicitly nondeterministic), so we make a simple modification to Eq. A.4 that makes both coefficients small:

$$\begin{aligned} &\langle t_{DGPS}[i] + \delta_f/2 - t_{EBEX}[i] - \Delta_{est} \rangle \\ &\qquad = \langle (R-1) \cdot t_{EBEX}[i] + (\Delta_{EBEX} - \Delta_{est}) \rangle \end{aligned} \tag{A.6}$$

where $\Delta_{est} = 1243737641.0$ s, which yields:

$$\begin{aligned} (R-1) &= -7.9537 \times 10^{-9} \\ (\Delta_{EBEX} - \Delta_{est}) &= -0.0324615 \text{ s} \\ \implies (\Delta_{EBEX} - \Delta_{est}) + \Delta_{est} = \Delta_{EBEX} &= 1243737640.9675384 \end{aligned}$$

which compares well with the original fit in Eq. A.5.

To estimate the variance of these results we apply a Monte Carlo approach. To investigate Δ_{EBEX}, define a Gaussian random variable r such that r_j is the j^{th} sample drawn from a distribution with $\bar{r} = 0$ and $\sigma_r = 0.1$ s. Then we modify Eq. A.6 to include r_j to form

$$\begin{aligned}&\big\langle \langle t_{DGPS}[i] + \delta_f/2 - t_{EBEX}[i] - \Delta_{est} + r_j \rangle_i \big\rangle_j \\ &\qquad\qquad = \big\langle \langle (R-1) \cdot t_{EBEX}[i] + (\Delta_{EBEX} - \Delta_{est} + r_j) \rangle_i \big\rangle_j\end{aligned}$$

We perform 1000 trial regressions and examine the statistics of $(\Delta_{EBEX} - \Delta_{est} + r_j) + \Delta_{est} - r_j = \Delta_{EBEX}$. The resulting $\overline{\Delta_{EBEX}}$ precisely matches the fit value above, and $\sigma_{\Delta_{EBEX}} = 8.9 \times 10^{-16}$, suggesting the result is stable to 14 digits, comparable to floating point numerical accuracy. Repeating the test with values of σ_r ranging from 1 to 10^{-5} gave similar results, suggesting that the precision of fit is not strongly dependent on the magnitude of the constant term. This is not extremely surprising, given that in least squares regression calculation of the constant term reduces to calculation of a mean. This test also shows no variation in $(R-1)$.

To investigate R we take r_i for $i \in D$ from a distribution with $\bar{r} = 0$ and $\sigma_r = 1$ ms, and use the equation

$$\begin{aligned}&\langle t_{DGPS}[i] + \delta_f/2 - t_{EBEX}[i] - \Delta_{est} + r_i \rangle \\ &\qquad\qquad = \langle (R-1) \cdot t_{EBEX}[i] + (\Delta_{EBEX} - \Delta_{est}) \rangle\end{aligned}$$

This is equivalent to introducing a jitter term into each reading of $t_{EBEX}[i]$. After performing 1000 regressions we examine the accumulated statistics of $(R-1)$, finding that $\overline{(R-1)} = -7.98 \times 10^{-9}$ and $\sigma_{R-1} = 3.3 \times 10^{-10}$. This test is also able to generate significant variation in $\sigma_{\Delta EBEX}$. Repeating this test with different values of σ_r reveals that σ_{R-1} and $\sigma_{\Delta EBEX}$ depend nearly linearly on σ_r, see Table A.1.

However, given that the mean values do not vary strongly with σ_r, we conclude from the values above that the magnitudes are robust results in the face of potentially large measurement jitters. The implication is that t_{EBEX} is drifting at about -8 ns/s relative to t_{DGPS}, some 40 times larger than the expected 0.2 ppb.

σ_r	σ_{R-1}	$\overline{(R-1)}$	$\sigma_{\Delta EBEX}$	$\overline{\Delta_{EBEX} - \Delta_{est}}$
1 ms	3.3×10^{-10}	-7.98×10^{-9}	3.32×10^{-4} s	-0.03246 s
10 ms	3.3×10^{-9}	-7.96×10^{-9}	3.28×10^{-3} s	-0.03233 s
100 ms	3.2×10^{-8}	-7.76×10^{-9}	3.36×10^{-2} s	-0.03232 s

Table A.1: Regression results and variances obtained by Monte Carlo iteration with Gaussian random timing jitter added.

A.6 Result

Finally, we can write down the timebase conversion function

$$\begin{aligned} t_{UTC} &= f\left(t_{EBEX}\right) \\ &\approx \left(1 - 8.0 \times 10^{-9}\right) t_{EBEX} + 1243737640.9675 \text{ s} \end{aligned} \tag{A.7}$$

with the coefficients uncertain only in the last digit, if we assume that the real world timing jitter is on the order of 1 ms or smaller. If that assumption is correct, Eq. A.7 gives a conversion of EBEX time to UTC world time that is accurate to less than 1 ms, as desired.

In practice, the true source of noise in this measurement is latency in receiving the absolute timestamp datum from the DGPS. Both the EBEX and DGPS timestamps are read digitally and processed as an integer value, and thus have effectively infinite precision. However, the time required to read the DGPS datum, comprising 30–40 bytes, over a serial link operating at 115200 bits/s, is 2–3 ms. We do not know how stable the timing of this data transmission might be.

Additionally, the Linux kernel scheduler used during the North American flight operates with a granularity of 4 ms[78], meaning that if DGPS data and a start-of-frame marker arrive within the same 4 ms window, it is indeterminate whether the frame will include the old or the new DGPS timestamp. This phenomenon is visible in Fig. A.1 as rapid oscillation in the value of δ_i near the end of each ramp. If this indeterminacy is unbiased, though, the effect should cancel out when averaged over many periods of δ_i, and in that case might be equivalent to a 2 ms jitter with respect to the analysis performed here.

Appendix B

Antenna Sensitivity Formalism

By choosing to treat a telescope as an antenna, we can address far-field sensitivity as gain relative to an isotropic receiver. Define a gain function on the sphere, $G : \mathbf{S}^2 \to \mathbb{R}_+$ normalized such that

$$\int_{4\pi} G(\phi, \theta) d\Omega = 1$$

For an isotropic radiator, the gain is constant $G_{iso} = 1/4\pi$ sr^{-1}. For all more complex receivers let the gain be nonnegative and piecewise continuous on compact regions. When dealing with antenna models gain is often expressed in units of dBi, or decibels relative to G_{iso}, and this convention is adopted here.

To describe the radiation received from the sky or other sources, we similarly define a source function $S : \mathbf{S}^2 \to \mathbb{R}_+$, where S is also nonnegative but need not be continuous anywhere. S can express quantities such as intensity (power per unit solid angle), specific intensity (intensity per unit frequency), or brightness temperature. To compute the total power or temperature of the antenna, take the inner product

$$T = \int_{4\pi} G(\phi, \theta) S(\phi, \theta) d\Omega$$

Since this operation is linear, it is possible to regard the gain function as the sum of several distinct components, $G = G_1 + G_2 + \cdots + G_n$, and likewise for the source function. In the case of the gain component functions, for the sake of simplicity we require that every $G_j(\phi, \theta) = G_j$ a constant over compact subdomain $\mathbf{A}_j \subset \mathbf{S}^2$, and

$G_j(\phi,\theta) = 0 = -\infty$ dBi everywhere else. Then we can simplify the normalization

$$\int_{4\pi} G(\phi,\theta)d\Omega = 1 = \sum_j G_j A_j$$

where $A_j$is the area of subdomain $\mathbf{A}_j$defined in the obvious way. The antenna temperature may then be evaluated as

$$T = \sum_j G_j \int_{\mathbf{A}_j} S(\phi,\theta)d\Omega$$

or more completely

$$\begin{aligned} T &= \sum_j G_j \int_{\mathbf{A}_j} S(\phi,\theta)d\Omega \\ &= \sum_j G_j \int_{\mathbf{A}_j} \sum_k S_k(\phi,\theta)d\Omega \\ &= \sum_{j,k} G_j \int_{\mathbf{A}_j} S_k(\phi,\theta)d\Omega \end{aligned}$$

We further recognize three distinct classes of such functions: beam, sidelobe, and diffuse. We assume a single beam component G_b such that the area of $\mathbf{A}_b$, $A_b \ll 4\pi$ and $G_b A_b \simeq 1$. We likewise assume a single diffuse component $G_d$for which $A_d = 4\pi$ and is thus constant everywhere. All other components $G_1, \cdots G_n$ are sidelobes, and $G_d \ll G_i \ll G_b$.

Now we can consider a single component of the above sum, the product of a sidelobe G and a source S which contributes a portion of the total antenna temperature $\Delta T = G \int_{\mathbf{A}} S(\phi,\theta)d\Omega$. In a common case, $S(\phi,\theta)$ can also be treated as constant (with value S) on a compact subdomain, which we will call the region $\mathbf{R}$, and zero elsewhere. Then we can write $\Delta T = G \cdot A \cdot d \cdot S$ where $d = area(\mathbf{A} \cap \mathbf{R})/A$ is the dilution factor describing the amount by which the portion of the source falling within the sidelobe underfills the sidelobe. Provided all the above simplifications hold, we have now reduced the antenna temperature problem to an algebraic operation:

$$T = \begin{bmatrix} G_b A_b \\ G_1 A_1 \\ \vdots \\ G_m A_m \\ G_d A_d \end{bmatrix} \begin{bmatrix} d_{b0} & d_{10} & \cdots & d_{m0} & d_{d0} \\ d_{b1} & d_{11} & & & \\ \vdots & & \ddots & & \vdots \\ d_{bn-1} & & & \ddots & \\ d_{bn} & & \cdots & & d_{dn} \end{bmatrix} \begin{bmatrix} S_0 & \cdots & S_n \end{bmatrix}$$

Appendix C

FFTs and the Periodogram in Python

C.1 Definition: Discrete Fourier Transform

The discrete Fourier transform develops from the continuous Fourier transform on functions $h : \mathbb{R} \to \mathbb{R}$ given by

$$H(f) = \int_{-\infty}^{\infty} h(t) e^{2\pi i f t} dt$$

Given instead a sequence $h_n = h(n\Delta)$ at (finite) N points $n \in \mathbb{Z}$, sampled at uniform intervals (e.g. of time) separated by $\Delta = 1/f$, the Fourier transform of the underlying function $h(t)$ can be approximated at N frequencies $f_n = \frac{n}{N\Delta}$, $n = -\frac{N}{2}, \cdots, \frac{N}{2}$. This approximation is[79]

$$H(f_n) \approx \sum_{k=0}^{N-1} h_k e^{2\pi i f_n t_k} \Delta = \Delta \sum_{k=0}^{N-1} h_k e^{2\pi i k n / N} = \Delta H_n \tag{C.1}$$

Note the implication that the terms H_n of the discrete Fourier transform approximate the continuous Fourier transform scaled by the sample period Δ.

C.2 The Periodogram

C.2.1 Power Spectral Density defined

The power spectral density of a real valued function $h(t)$ of infinite duration is defined as the Fourier transform of its autocorrelation function[79]. Since correlation in the Fourier domain is $Fourier\left\{h(t) * g(-t)\right\} = H \cdot \bar{G}$, ($\bar{G}$ denotes the compex conjugate of G) the Fourier transform of the autocorrelation function is equivalent to

$$Fourier\left\{(h(t) * h(-t)\right\} = H \cdot \bar{H} = |H|^2$$

That this is equivalent to a power density follows from Parseval's theorem: total power equals

$$\int_{-\infty}^{\infty} |h(t)|^2 \, dt = \int_{-\infty}^{\infty} |H(f)|^2 \, df$$

The discrete form of Parseval's theorem is:

$$\sum_{k=0}^{N-1} |h_k|^2 = \frac{1}{N} \sum_{k=0}^{N-1} |H_k|^2$$

C.2.2 Time integral squared amplitude

For a function sampled over a finite period of time, total power may be defined as the time integral squared amplitude[79]:

$$\int_{0}^{T} |h(t)|^2 \, dt \approx \Delta \sum_{j=0}^{N-1} |h_j|^2$$

Note that there are other conventions for defining total power, and the convention used varies by author and by field. The above definition is chosen because it yields units of $(\text{signal unit})^2 / Hz$, as typically reported in our field.

C.2.3 Discrete periodogram estimator

The periodogram is an estimator for the discrete power spectral density (with units of $(\text{signal unit})^2/Hz)$ defined at $N/2+1$ frequencies $f_k = k/N\Delta$:

$$
\begin{aligned}
P(0) = P(f_0) &= \frac{\Delta}{N}|H_0|^2 \\
P(f_k) &= \frac{\Delta}{N}\left[|H_k|^2 + |H_{N-k}|^2\right] \quad k = 1, 2, \ldots, \left(\frac{N}{2}-1\right) \\
P(f_c) = P\left(f_{N/2}\right) &= \frac{\Delta}{N}\left|H_{N/2}\right|^2
\end{aligned}
$$

which by Parseval's theorem preserves the total power (time integral squared amplitude) as

$$
\begin{aligned}
P(f_0) + P\left(f_{N/2}\right) + \sum_{k=1}^{N/2-1} P(f_k) &= \frac{\Delta}{N}\sum_{k=0}^{N-1}|H_k|^2 \\
&= \Delta\left[\frac{1}{N}\sum_{k=0}^{N-1}|H_k|^2\right] \\
&= \Delta\sum_{k=0}^{N-1}|h_k|^2
\end{aligned}
$$

Note that for purely real input, $H_k = H_{N-k}$ and therefore

$$
P(f_k) = \frac{\Delta}{N}\left[|H_k|^2 + |H_{N-k}|^2\right] = \frac{2\Delta}{N}|H_k|^2
$$

Alternatively, if a single form for all $P(f_k)$ is desired, let k range from 0 to $N-1$ such that the periodogram ranges over both positive and negative frequencies. This is not the approach used here, however.

C.3 Windowing

The expectation value of the periodogram estimate P_k is the convolution of the continuous spectrum $P(f)$ and the window function that selects the sampled data from the underlying (mathematically, infinite in duration) signal function. To control leakage of power into adjacent frequency bins, we typically multiply the sampled data by a window function that turns off less rapidly than the tophat function that describes un-windowed data of finite duration. We must then modify the periodogram estimate to preserve total power.

For an arbitrary window function $w(t)$ take samples w_k chosen in the same way as the data h_k. Let S_k be the terms of the discrete Fourier transform of signal $s_k = h_k w_k$. Then the terms of the periodogram become[79]

$$P(f_k) = \frac{\Delta}{\sum_{j=0}^{N-1} w_j^2} \left[|S_k|^2 + |S_{N-k}|^2 \right] \quad k = 1, 2, \ldots, \left(\frac{N}{2} - 1 \right) \tag{C.2}$$

and analogously for $P(0)$ and $P\left(f_c = f_{N/2}\right)$. Clearly this is just the usual periodogram, computed on windowed data, and scaled by the squared sum of the window function. In the limiting case where $w_j \equiv 1$ for all j, $\sum_{j=0}^{N-1} w_j^2 = N$ and the formula for the unwindowed periodogram is recovered.

C.4 Implementation

In python[54], the `numpy[80]` module provides an array datatype with the property that simple operations on the containing vector are efficiently applied to each contained value. Thus, for an array `data`, `data**2` yields an array containing the square of each value in `data`, `abs(data)` yields the real magnitude, and so on.

The function `rfft(data)` computes the positive-frequency terms (H_j for $j = 0$ to $N/2$) of the discrete Fourier transform. The function `hanning(N)` computes the terms of a Hanning window of length N. The function `abs(data)` returns the magnitude of the (potentially complex) values in `data`. Thus the expression `abs(rfft(data*hanning(N))` evaluates to $|S_k|$ from Eq. C.2 above.

Data vectors have a method `data.mean()`, which computes the mean of the values in the vector. Thus the expression `(hanning(N)**2).mean()` evaluates to $\frac{1}{N} \sum_{j=0}^{N-1} w_j^2$.

The following code is currently used to implement the above periodogram, windowed by a Hanning window:

```
from numpy import sqrt, hanning
from numpy.fft import rfft


def stdrps(data, Fs=1.0):
```

```
    """Standard power spectrum on real valued data."""
    N = len(data)
    Y = sqrt(1. / Fs / N) * abs(rfft(data*hanning(N)))
    Y[1:-1] *= sqrt(2.0)
    return Y / sqrt((hanning(N)**2).mean())
```

Using the above definitions, this function yields $Y = \sqrt{\frac{\Delta}{N}} |S_k| \left[\frac{1}{N}\sum_{j=0}^{N-1} w_j^2\right]^{-1/2} = \sqrt{\frac{\Delta}{\sum_{j=0}^{N-1} w_j^2} |S_k|^2}$ for $k = 0$ and $N/2$, and $Y = \sqrt{\frac{2\Delta}{\sum_{j=0}^{N-1} w_j^2} |S_k|^2}$ for all other k. Comparing to Sec. C.3, this is equal to $\sqrt{P(f_k)}$ for all k. This value is returned, instead of $P(f_k)$, so that the returned values will have units of (signal unit)/$\sqrt{Hz}$.

C.4.1 Periodogram with Reduced Variance

The periodogram estimator described in Sec. C.3 has variance $\sigma_k = \langle P_k \rangle^2$ for all frequencies f_k, independent of the data length N[79]. Welch's method yields a periodogram estimator that features, for given N, reduced variance in each frequency bin in exchange for a reduced number of total bins, i.e. reduced frequency resolution[81]. This is accomplished by partitioning the input signal data into M segments of equal length, independently computing the windowed periodogram of each segment, and averaging (in squared amplitude) the resulting M estimates.

The output of this procedure is a periodogram estimator with variance $\sigma_k = \langle P_k \rangle^2 / M$ for each bin, and $N/2M + 1$ frequency bins. The following python code implements this operation, making use of the `stdrps` function defined above:

```
def welchpsd(data, M, Fs=1.0):
    """Welch method periodogram on real-valued data"""
    NFFT = len(data) // M
    Y = zeros(NFFT//2 + 1)
    for i in range(M):
        off = i*NFFT
        Y += stdrps(data[off:off+NFFT], Fs)**2
    return numpy.sqrt(Y / M)
```

To further reduce the estimator variance, it can be shown[81] that the variance per frequency bin is nearly minimized by modifying this procedure to use $2M-1$ half-overlapping data segments.

C.4.2 Python's FFT

From Eq. C.1, the discrete Fourier transform yields the sequence

$$H_n = \sum_{k=0}^{N-1} h_k e^{2\pi ikn/N}, \quad n = -\frac{N}{2}, \cdots, \frac{N}{2}$$

Note that the sign of the exponent inside the sum is arbitrary, and is negative in the implementation used by `numpy`. Either way, the sign will be opposite in the inverse transform.

Consider a test input sequence of length 8, $a_n = \{1, 2, 3, 4, 8, 7, 6, 5\}$. The expression `(a * exp(-2j*pi*arange(8)*n/8)).sum()` computes the n^{th} term

$$A_n = \sum_{k=0}^{7} a_k e^{-2\pi ikn/8}$$

and within numerical accuracy yields an identical sequence as the `numpy` function `fft`:

$$\begin{aligned}
A_0 &= 36.00 + 0.00i \\
A_1 &= -9.83 + 7.24i \\
A_2 &= 0 \\
A_3 &= -4.17 + 1.24i \\
A_4 &= 0 \\
A_5 &= -4.17 + -1.24i \\
A_6 &= 0 \\
A_7 &= -9.83 + -7.24i
\end{aligned}$$

The `numpy` function `rfft` returns the sequence $\{A_0, A_1, A_2, A_3, A_4\}$.

Appendix D

Implementation of the SFD Dust Model

The following is the source code to the Python module `dustsfd`, which was developed by this author to implement the algorithms of Finkbeiner et al[69] in Python and interface them directly to `healpy`. It is presented here for reference in the hope that it might prove useful to others.

```
#!/usr/bin/python

"""Code pertaining to the SFD dust map and predictions

Analysis from Finkbeiner Davis & Schlegel 1999
Data from http://www.astro.princeton.edu/~schlegel/dust/

Implementation by Michael Milligan based on predict_thermal in
subs_predict.c from C code at above site.

Note that as in C code, model number ranges from 1 to 8:
        1: One-component, nu^1.5 emissivity
        2: One-component, nu^1.7 emissivity
        3: One-component, nu^2.0 emissivity
        4: One-component, nu^2.2 emissivity
        5: Two-component, alpha1=1.5, alpha2=2.6, Pollack et al. model
        6: Two-component, both nu^2 emissivities, fit f+q
        7: Two-component, alpha1=1.5, alpha2=2.6, fit f+q
```

```
        8: Two-component, alpha1=1.67, alpha2=2.70, fit alphas+f+q
"""

import healpy
import pyfits
import numpy

sfd_fname = \
    '/home/lab/analysis/mmilligan/dipole/SFD_i100_healpix_512.fits'
fink_fname = \
    '/home/lab/analysis/mmilligan/dipole/FINK_Rmap_healpix_512.fits'

path = '/home/lab/analysis/mmilligan/dipole/'
sfd_pat = 'SFD_i100_healpix_%d.fits'
fink_pat = 'FINK_Rmap_healpix_%d.fits'

# constants and tables for model parameters
nu100 = 2997.92458 #/* Frequency in GHz for 100-microns */
h_Pl = 6.6261e-27  #/* cm^2 g s^-1 */
k_B = 1.3806e-16   #/* erg K^-1 */

alpha1vec = [1.50, 1.70, 2.00, 2.20, 1.50, 2.00, 1.50, 1.67]
alpha2vec = [0.00, 0.00, 0.00, 0.00, 2.60, 2.00, 2.60, 2.70]
f1vec     = [1.00, 1.00, 1.00, 1.00, 0.25, 0.00261, 0.0309, 0.0363]
q1q2vec   = [1.00, 1.00, 1.00, 1.00, 0.61, 2480.0, 11.2, 13.0]

# /* Rfita contains fit coefficients for T2_of_R */
RfitA = numpy.array(
    [[2.9268E+00, 3.8419E-01, 5.0233E-02, 1.0852E-02,
                                          3.0738E-03, 5.0595E-04],
     [2.8483E+00, 3.8044E-01, 4.6584E-02, 9.0938E-03,
                                          2.7038E-03, 5.4664E-04],
     [2.7334E+00, 3.7537E-01, 4.1712E-02, 6.8839E-03,
                                          2.0316E-03, 6.0311E-04],
     [2.6556E+00, 3.7377E-01, 3.9898E-02, 5.7662E-03,
                                          1.4638E-03, 6.3723E-04],
     [2.9206E+00, 2.3254E-01, 2.3506E-02, 4.0781E-03,
                                          1.0048E-03, 1.2004E-04],
     [2.9900E+00, 2.5041E-01, 2.9688E-02, 6.5641E-03,
```

```
                                            1.5688E-03, 1.6542E-04],
      [2.8874E+00, 2.4172E-01, 2.9369E-02, 4.7867E-03,
                                            9.7237E-04, 1.1410E-04],
      [2.8723E+00, 2.4071E-01, 2.9625E-02, 4.7196E-03,
                                            9.3207E-04, 1.1099E-04] ]
    )
"""/* Rfita contains fit coefficients for T2_of_R */"""

Zindx = [1.50, 1.67, 1.70, 2.00, 2.20, 2.60, 2.70]
Zintegral = [5.3662E+01, 7.0562E+01, 7.4100E+01, 1.2208E+02,
    1.7194E+02, 3.4855E+02, 4.1770E+02]
Zint = dict( zip( Zindx, Zintegral ))
"""Zeta integrals for alpha=[1.50, 1.67, 1.70, 2.00, 2.20, 2.60, 2.70]
   from equn (15) of Finkbeiner et al.
"""

def tcoeff(model=8, alpha1=None, alpha2=None, q1q2=None):
    """Compute coefficient relating T1 and T2 after SFD99 eqn 14

    To supply arbitrary model parameters, pass model=None and supply
    alpha1, alpha2 (from [1.50, 1.67, 1.70, 2.00, 2.20, 2.60, 2.70])
    and q1q2
    """
    if model is not None:
        alpha1 = alpha1vec[model-1]
        alpha2 = alpha2vec[model-1]
        if alpha2 == 0.0:
            raise ValueError('tcoeff only sensible for models 5-8')
        q1q2 = q1q2vec[model-1]
    return pow( (Zint[alpha2] / (q1q2*Zint[alpha1]))
       * pow(h_Pl*nu100*1.0e+9/k_B,alpha1-alpha2), 1./(4.+alpha1) )

# We tabulate the K-factor for only the following emissivity profiles
Kfitindx = dict(zip([1.50, 1.67, 1.70, 2.00, 2.20, 2.60, 2.70],
                    range(7)))
KfitAarr = numpy.array(
    [ [   1.00000,   2.08243,  -4.72422,   2.29118 ],
      [   1.00000,   2.15146,  -4.84539,   2.35210 ],
      [   1.00000,   2.14106,  -4.83639,   2.35919 ],
```

```
        [   1.00000,   2.18053,  -4.89849,   2.38060 ],
        [   1.00000,   2.55941,  -5.41290,   2.57867 ],
        [   1.00000,   3.16383,  -6.23131,   2.86900 ],
        [   1.00000,   3.31600,  -6.43306,   2.93939 ] ] )
KfitBarr = numpy.array(
    [ [  -0.88339,   4.10104,  -4.43324,   1.76240 ],
        [  -0.87985,   4.10909,  -4.43404,   1.76591 ],
        [  -0.93625,   4.19278,  -4.46069,   1.77103 ],
        [  -0.80409,   3.95436,  -4.27972,   1.70919 ],
        [  -0.80318,   4.20361,  -4.55598,   1.80207 ],
        [  -0.50356,   4.07226,  -4.70080,   1.87416 ],
        [  -0.41568,   4.02002,  -4.72432,   1.88865 ] ] )

def kfactor(alpha, T):
    """Return DIRBE color-correction (K-factor) for 100-micron map.

    Vectorized in T (temperature Kelvin)
    alpha should be a scalar in
          [1.50, 1.67, 1.70, 2.00, 2.20, 2.60, 2.70]
    """
    ia = Kfitindx[alpha]
    T = numpy.asarray(T)
    log10T = numpy.log10(T)
    Tpow = 1.0
    sum1 = T * 0
    sum2 = T * 0
    for i in range(0,4):
        sum1 += KfitAarr[ia][i] * Tpow
        sum2 += KfitBarr[ia][i] * Tpow
        Tpow *= log10T
    return sum1 / sum2

def planck(nu, T):
    """Return planck function in MJy/sr

    Vectorized in T (temperature Kelvin)
    nu is frequency in GHz

    * This is based upon the IDL procedure PLANCK() written by Rich
```

```
* Isaacman for the COBE analysis software.
"""
cspeed = 299792.458e+0  #/* speed of light in km/s */
hck = 14387.69e+0       #/* h*c/k             */
SBconst = 2.7794795e-13 #/* Stephan-Boltzmann * 15/pi^5 */
temp = numpy.asarray(T)

#/* Variable fhz is a scale factor used to go from units of
#   nu_I_nu units to MJy/sr if the keyword is set.  In that case,
#   its value is frequency in Hz * w/cm^2/Hz ==> MJy */
fhz = nu * 1.0e-15

#/* Introduce dimensionless variable chi, used to check whether we
#   are on Wien or Rayleigh Jeans tails */
# FIXME: doesn't work for scalar T (chi ends up scalar)
chi = hck * nu / (cspeed * temp)
RayJean = (chi < 0.001)
Wein = (chi > 50.0)

val = temp * 0.0

#if (chi < 0.001) {
#/* Rayleigh-Jeans side */
ind = numpy.where(RayJean)[0]
val[ind] = SBconst * pow(temp[ind],4.0) * pow(chi[ind],3.0) / fhz;
#} else if (chi > 50.) {
#/* Wein tail */
ind = numpy.where(Wein)[0]
val[ind] = SBconst * pow(temp[ind]*chi[ind],4.0) * \
            numpy.exp(-1 * chi[ind]) / fhz;
#} else {
#/* Exact solution */
ind = numpy.where(numpy.logical_and(
        numpy.logical_not(RayJean), numpy.logical_not(Wein) ))[0]
val[ind] = SBconst * pow(temp[ind]*chi[ind],4.0) / \
            ( (numpy.exp(chi[ind]) - 1.0) * fhz);
#}

return val
```

```python
def fac_flux2temp(nu):
    """Compute factor to convert from flux/sr to brightness temp.

    Return conversion factor (MJy/sr) / (micro-K)

    (float      nu) /* frequency in GHz */
    """
    k_b = 1.3806e-16 # /* erg K^-1 */

    fac = 4.5e-9 / (k_b * nu * nu)
    return fac

def planckcorr(nu):
    """Compute factor to convert from brightness temp to thermodynamic
    temp in micro-K.

    (float      nu) /* frequency in GHz */
    """

    k_b = 1.3806e-23 #/* J/K */
    h_Pl = 6.6262e-34 #  /* J*s */
    T_cmb = 2.73 #      /* K    */

    x = h_Pl * nu * 1.e9 / (k_b * T_cmb)
    result = pow(numpy.exp(x)-1.,2.0) / (x*x * numpy.exp(x))

    return result

def try_read_map(fname):
    try:
        data = healpy.read_map(fname)
        return data
    except IndexError:
        pass
    f = pyfits.open(fname)
    for hdu in f:
        if hdu.header.has_key('NAXIS'):
            if hdu.header.get('NAXIS') == 1:
```

```
                return hdu.data
    raise IOError('did not find map data in file: %s' % fname)

def read_maps(nside=512, onlydust=False, onlyrmap=False):
    D = None
    R = None
    d_fname = '%s%s' % (path, sfd_pat % nside)
    r_fname = '%s%s' % (path, fink_pat % nside)
    if onlydust:
        return try_read_map(d_fname)
    elif onlyrmap:
        return try_read_map(r_fname)
    else:
        return try_read_map(d_fname), try_read_map(r_fname)



def read_sfd(fname=sfd_fname):
    f = pyfits.open(fname)
    return f[0].data

def RtoT(R, model=8):
    """Compute pixel T given ratio R.

    Implements equation B2 from SFD99 for given model parameters.
    Returns dust T in Kelvin (vectorized in R).
    For two-component models, this returns T2.
    """
    R = numpy.asarray(R)
    lnR = numpy.log(R)
    lnRpow = lnR * 0.0 + 1.0
    lnT = lnR * 0.0
    for i in range(0,6):
        lnT += RfitA[model-1][i] * lnRpow
        lnRpow *= lnR
    return numpy.exp(lnT)

def T2toT1(T2, model=8):
    return tcoeff(model) * \
        pow( T2, (4+alpha2vec[model-1])/(4+alpha1vec[model-1]) )
```

```python
def predict_thermal_flux(I100, R, nu, model=8):
    """Compute dust brightness at nu from 100 um I and DIRBE R.

    Implement flux calculation of predict_thermal.
    I100 is 100 um flux from SFD98 map.
    R is the DIRBE 100/240 flux ratio from SFD98.
    I100 and R must have compatible dimensions.
    nu is prediction frequency in GHz.

    For models 1-4:
    SINGLE-COMPONENT MODEL: Evaluate equn (1) from Finkbeiner et al

    For models 5-8:
    TWO-COMPONENT MODEL: Evaluate equn (6) from Finkbeiner et al
    """
    alpha1 = alpha1vec[model-1]
    alpha2 = alpha2vec[model-1]
    I100 = numpy.asarray(I100)
    R = numpy.asarray(R)
    T = RtoT(R, model)
    if alpha2 == 0:
        # One-component model
        Inu = I100 * pow(nu/nu100,alpha1) * planck(nu,T) / \
          ( planck(nu100,T) * kfactor(alpha1,T) )
    else:
        # Two-component model
        T2 = T
        T1 = T2toT1(T2, model)
        f1 = f1vec[model-1]
        q1q2 = q1q2vec[model-1]
        Inu = I100 * \
          ( f1 * q1q2 * pow(nu/nu100,alpha1) * planck(nu,T1) \
            + (1-f1) * pow(nu/nu100,alpha2) * planck(nu,T2) ) / \
          ( f1 * q1q2 * planck(nu100,T1) * kfactor(alpha1,T1) \
          + (1-f1) * planck(nu100,T2) * kfactor(alpha2,T2) )
    return Inu

def convert_units(Inu, nu, units="MJy"):
```

```
    """Convert flux to brightness or thermodynamic temperature.

    Inu is flux (MJy/sr) as returned by predict_thermal_flux.
    nu is frequency in GHz.
    units may be:
      "MJy" or "flux" - return Inu unchanged
      "microK" or "brightness" - return brightness temp in uK
      "thermo" or "uKthermo" - return thermodynamic temp in uK
    """
    if units in ("MJy", "flux"):
        return Inu
    elif units in ("microK", "brightness"):
        return Inu * fac_flux2temp(nu)
    elif units in ("thermo" or "uKthermo"):
        return Inu * fac_flux2temp(nu) * planckcorr(nu)
    else:
        raise ValueError('Invalid units value')

def predict_thermal(I100, R, nu, units="MJy", model=8):
    """Compute dust signal.

    Wraps predict_thermal_flux and convert_units.
    See those functions for meaning of arguments and return values.
    """
    return convert_units(
                predict_thermal_flux(I100, R, nu, model),
                nu, units)
```